

Progress Towards Quantum Computing with Neutral Atom Arrays

By
Xiaoyu Jiang

A dissertation submitted in partial fulfillment
of the requirements for the degree of
Doctor of Philosophy
(Physics)

at the
UNIVERSITY OF WISCONSIN-MADISON
2022

Date of Final Oral Exam: 08/05/2022

The dissertation is approved by the following members of the Final Oral Committee:

Mark Saffman, Professor, Physics
Robert Joynt, Professor, Physics
Maxim Vavilov, Professor, Physics
Swamit Tannu, Assistant Professor, Computer Science

© Copyright by Xiaoyu Jiang 2022

All Rights Reserved

Progress towards quantum computing with neutral atom arrays

Xiaoyu Jiang

Abstract

This thesis reports progress towards implementing quantum computing applications on a two-dimensional array of neutral atom qubits. While significant progress has taken place in our lab, here we focus on presenting theoretical analysis on various aspects of the experiment, to help improve the performance of the main experiment.

We finished a thorough analysis of the effect of laser noise on 1- and 2-photon Rabi oscillations, with both theoretical analysis and numerical simulations. We developed a theory to directly match a laser's frequency noise power spectral density to its self-heterodyne spectrum measured experimentally. We also predicted the error generated by white noise and spectra with servo-bumps, and our results match well with numerical simulations. A quasi-static theory is also proposed to estimate the error under certain limits, and has demonstrated a good match to numerics.

We designed a protocol for multi-qubit neutral atom gates. The protocol implements symmetric adiabatic pulses on the $k + 1$ atoms in the system to implement $C_k Z$ gates and CZ_k gates. The case that we studied was assumed equal Rydberg coupling strengths between data qubits for $C_k Z$ gates, and 0 coupling between data qubits for CZ_k gates. We show that fidelity $\mathcal{F} > 0.99$ can be achieved for both types of gates, with gate times $< 0.5 \mu\text{s}$ for $k \leq 4$. Our analysis is performed with experimentally realistic parameters.

We have also analyzed a neutral atom implementation of the surface code. In our protocols we have designed novel high-fidelity multi-qubit gates to reduce error and cycle time of the surface code. A two atomic species scheme is used to mitigate measurement crosstalk on data qubits when ancillas are being measured. We have also introduced a novel repumping scheme to convert leakage errors to depolarization errors that are correctable

by the surface code. Finally we will analyze the performance of a surface-13 code with realistic gate parameters.

Several experimental projects on improving the experimental system are also reported in this thesis, mainly on a frequency-doubling laser system with critical phase matching and Brewster-cut crystal.

To my grandma

Acknowledgements

First of all, I would like to thank my advisor, Professor Mark Saffman. Mark is a great group leader, a knowledgeable scientist, and a patient educator. I appreciate him for giving me this chance to be a member of the Saffman lab six years ago, to every insightful advice he offered me during my Ph.D study. I learned a lot from him.

I would like to thank Dr. Mark. Friesen, for his collaboration on the laser noise project, and Dr. Matthew Otten for his collaboration on the multi-qubit gate and the surface code project. They are both stellar physicists and it was my honour to work with them.

I would like to pay tribute to everyone that has worked in room 5323, the AQuA/ARL lab. Trent Graham is the leading scientist in the AQuA experiment, who came to the team a little earlier than I. He was the one who taught me the whole skill set needed to work in an optics lab. He is very knowledgeable and hard-working, and has always been a model for me to learn from. I also want to thank Matthew Ebert and Minho Kwon, for their help with various projects that I worked on. I also have the privilege to have worked with Garrett Hickman, Kais Jooya and Ravi Chinnarasu. I want to also thank Cody Poole and Jacob Isaacs, my fellow graduate student lab partners, for sharing the days in the lab and our thoughts on science. I am also pleased to have worked with many talented undergraduate students: Sebastian Malewicz, Alphonse Marra, Brandon Grinkemeyer, Samuel Cieszynski and Genevieve Kearns.

I also want to thank other friendly and knowledgeable graduate students that I worked with in the Saffman lab: Christopher Yip, Christopher Young, Juan Bohorquez, Preston Huft, Peiyu Yang, Sam Norrell, Eunji Oh and Linipun Phutittarn.

Many friends helped me in this 6-year journey. First and most importantly, I want to thank two other members of our "physics squad", Chuanhong Liu and Qinrui Liu. It's always comforting when there are friends to listen to your worries, give suggestions when you are confused, and laugh together for something good. For me they have been there for the past 6 years, and it has been a true blessing to me.

I would also like to thank all the great friends that I have in Madison: Tianyu Ma,

Yanhe Huang, Ping-yu Li, Yu Gao, Minjie Shen, Junying Liu, Zhaoning Yu, Sida Lu, Yun Li, "Newton" Niudun Wang, Ye Yuan, Yeyu Zhang, Yu Feng, Ruosen Xie and Hannah Cai.

I want to thank my life-long friend Chenhua Geng, for sharing the nonsense messages, rejuvenating jokes and encouraging words.

Finally I want to thank my parents for their unconditional love. They deserve the most credit for anything I have achieved. Their heartwarming words will always be the motivation for me to move forward.

Contents

List of Figures	x
List of Tables	xvii
1 Introduction	1
1.1 Quantum Computing Overview	1
1.2 The Atomic Qubit Array(AQuA) Experiment	2
2 Experimental Subsystem Development	6
2.1 Frequency Doubling	6
2.1.1 Critical phase-matching	7
2.1.2 Boyd-Kleimann optimization	10
2.1.3 Cavity design	12
2.1.4 Total conversion efficiency	14
2.1.5 Optical setup and test	16
3 Laser Noise Analysis	20
3.1 Laser Noise As Random Process	21
3.1.1 Random Process	21
3.1.2 Features of Laser Noise	24
3.1.3 Time-series Reconstruction	25
3.2 Laser Noise Model For Simulation	26
3.2.1 Phase noise	26

3.2.2	Frequency Noise	27
3.2.3	Intensity noise	29
3.3	Analysis of Self-Heterodyne Spectrum	29
3.3.1	Laser Lineshape	30
3.3.2	Self-Heterodyne Spectrum	33
3.4	Retrieving Noise Power Spectral Density from measurements	36
3.4.1	White Noise	37
3.4.2	Servo bump	40
3.4.3	Laser characterization	42
3.5	Density Matrix Solutions for Rabi Oscillations	43
3.5.1	Time-Series Expansion of the Laser Noise	43
3.5.2	Time-Series Master Equation	45
3.5.3	Two-Photon Gate Fidelity	51
3.6	Bandwidth-Limited Phase Noise and the Quasi-static Limit	54
3.6.1	Master Equation Approach	55
3.6.2	Static Gaussian-Distributed Noise	57
3.7	Intensity Noise	62
3.8	Numerical Simulations of the Laser Noise	66
3.8.1	Dynamical Equations	66
3.8.2	Testing Density Matrix Solutions	68
3.8.3	Testing Quasi-Static Model	72
3.8.4	Effect of Laser noise on Ramsey Measurements	76
3.9	Outlooks for Future Research	80
4	Multi-Qubit Gate	82
4.1	$C_k Z$ gate protocol	82
4.1.1	Numerical results for symmetric interactions	85
4.1.2	Numerical results for asymmetric interactions	86
4.2	CZ_k gate protocol	86

4.2.1	Numerical results with zero target-target couplings	88
4.2.2	Numerical results with finite target-target couplings	88
4.3	Qubit pumping	89
4.4	Plaquette geometries for uniform Rydberg interactions	91
5	Implementation of the Surface Code	94
5.1	Analysis of the s-13 Code	95
5.2	Single Plaquette Simulation	97
6	Conclusion and Outlook	101
A	Parameters for multi-qubit gates	103
A.1	Parameters for CZ_k gate with single Gaussian pulses	103
A.2	Parameters for C_kZ gate with ARP pulses	104
B	Sensitivity of CZ_k and C_kZ gates to phase variations	107
C	QuaC simulator	110
	Bibliography	111

List of Figures

1.1	a) Experimental layout for trapping and addressing atomic qubits. b) Atomic level diagram and wavelengths used for cooling, trapping, and qubit control. c) Averaged atomic fluorescence image of the 49 site array with spacing $3 \mu m$. Each camera pixel is $0.6 \times 0.6 \mu m$ at the atoms. d) Global microwave Rabi rotations on a block of 9 qubits at 76.5 kHz. The microwave phase, amplitude, and frequency are controlled by an arbitrary waveform generator. e) A Ramsey experiment with microwave $\pi/2$ pulses and the focused 459 beam providing an $RZ(\theta)$ rotation on a single site. f) Parity oscillation of a 2-qubit Bell state created using a CZ gate. The measured and uncorrected Bell state fidelity was 92.7(1.3)% for an optimized qubit pair ($\approx 95.5\%$ corrected for state preparation and measurement (SPAM) errors).	3
1.2	Preparation of GHZ states. a) Parity oscillations for GHZ states with 2 – 6 qubits. b) The fidelity of the created GHZ state versus qubit number. c) Decoherence time of GHZ states measured by Ramsey interference.	4
1.3	Quantum phase estimation using 3 and 4 qubits. a) Phase estimation circuit using 4 qubits. b) Quantum phase estimation results using 3 qubits. c) Quantum phase estimation with four qubits to estimate the molecular energy of a H_2 molecule.	5

1.4 QAOA algorithm for solving MaxCut. a) Circuit diagram for 4-qubit QAOA MaxCut showing a single $p = 1$ cycle. b) Decomposition of the $ZZ(\gamma) = e^{-i\frac{\gamma}{2}}Z \otimes Z$ interaction into two CNOT gates and an RZ rotation. c) Circuit results for $p = 1, 2, 3$ with optimized γ and β values.	5
2.1 Layout of the 952nm-476nm doubling system.	8
2.2 Shape of the LBO crystal. The beam enters the crystal at Brewster angle θ_b , and travels through the crystal parallel to the long edges. $\beta = \theta_b$	9
2.3 Critical phase matching of second-harmonic generation in LBO crystal. ϕ_m is the critical phase-matching angle.	10
2.4 Layout of the cavity. L1 is the input coupling lens. F1 is the input coupler. F2 is a flat mirror attached to a piezoelectric transducer for cavity length scanning and locking. C1 and C2 are curved mirrors.	12
2.5 Layout of the cavity. L1 is the input coupling lens. F1 is the input coupler. F2 is a flat mirror attached to a piezoelectric transducer for cavity length scanning and locking. C1 and C2 are curved mirrors.	14
2.6 Second harmonic power P_{out} vs fundamental beam power P_{in} , at different input coupler transmission coefficient T	15
2.7 Design of the cavity assembly. The temperature of the crystal is stabilized through the thermometric cooler(TEC) under the trapezoid-shaped crystal holder. The temperature of the base plate where the mirrors are mounted is also stabilized with TECs under the plate, in order to avoid thermal drifts of cavity length. A cavity lid(not plotted) is also designed to minimize air turbulence. A band-pass input window for fundamental light and an output window for blue light is mounted on the lid. The electrical feed-through provides access to the piezo and two TECs.	17
2.8 PDH error signal box.	18
2.9 Pink: error signal; Yellow: error transmission.	19

2.10 ULE cavity transmission taken by a Raspberry-Pi camera. The laser is locked to a stable mode of the cavity.	19
3.1 Heterodyne setup. The laser signal is split equally between two paths. One path passes through a single-mode fiber (SMF), where it is delayed by time t_d . It then passes through an acousto-optic modulator (AOM), where its frequency is shifted by ν_s . The interfering signals are combined and measured by a photodiode (PD), and finally processed through a spectrum analyzer (SA).	33
3.2 White noise power spectral densities: $S_\phi(f)$ (blue) corresponds to Eq. (3.68) with $h_0 = 100$ Hz, $2S_E(f)/E_0^2$ (gold) is obtained from Eq. (3.71)], $S_i(f)/4$ (red) is obtained from Eq. (3.74), omitting the δ -function peak. The inset shows the same quantities, plotted on a logarithmic frequency scale. Here, an approximate form for $S_i/4$ (red, dotted) is obtained from Eq. (3.65). The cutoff frequency f_x (vertical black), obtained from Eq. (3.53), indicates where we expect Eq. (3.52) to fail.	38

3.3 1040 nm solid-state Ti:Sa laser: self-heterodyne data and fits. (a) Self-heterodyne power spectral density, obtained in a 50 kHz frequency window with RBW = 100 Hz (open blue circles), or in a 600 kHz window with RBW = 300 Hz (closed red markers). The data are shifted horizontally so their peaks are centered at zero frequency, and shifted vertically so that they overlap. An optical delay fiber of 11 km is used for both data sets, corresponding to a delay time of $t_d = 5.445 \times 10^{-5}$ s. The data are then fit to Eq. (3.84) (black line), obtaining $\alpha = 5/2$ and $\sigma = 240$ Hz. Finally, all data are renormalized to ensure the correct total power. (b) Same red data set as (a), plotted over a wider frequency window. The data are then fit to Eq. (3.83), including two gaussian servo bumps, obtaining $h_0 = 13$ Hz, $h_{g1} = 2.0$ kHz, $\sigma_{g1} = 1.5$ kHz, $f_{g1} = 234$ kHz, $h_{g2} = 25$ Hz, $\sigma_{g2} = 18$ kHz, and $f_{g2} = 130$ kHz. (c) Phase and frequency power spectral densities, $S_\phi(f)$ and $S_{\delta\nu}(f)$ (inset), resulting from the fitting.	42
3.4 Coupling scheme for two-photon Rabi oscillations in a ladder configuration	52
3.5 Rabi errors for one-photon Rabi oscillations due to band-limited white frequency noise with fixed amplitude $h = 3.18$ kHz ² /kHz, while sweeping the noise bandwidth.	57
3.6 (a: π pulse; b: 2π pulse) Relation between rabi population errors and the amplitude h_0 of the white noise spectrum. Bandwidth of the spectrum in the simulation is $bw = 10\Omega_0$, $\Omega_0 = 1\pi$ MHz.	69
3.7 (a: π pulse; b: 2π pulse) Relation between rabi population errors and the fractional power of the servo bump. $h_g = 1100$ Hz ² /Hz, $\sigma_g = 1.4$ kHz, f_g is the bump center frequency where maximum error is generated.	70
3.8 (a: π pulse; b: 2π pulse) Relation between Rabi population errors and the center frequency of the servo bump f_g . Here we assume that the two lasers have the same frequency noise power spectrum. $h_g = 1100$ Hz ² /Hz, $\sigma_g = 1.4$ kHz. Ω_0 is the Rabi frequency.	71

3.9 (a: π pulse; b: 2π pulse) Relation between rabi population errors and the amplitude h_0 of the white noise spectrum. Bandwidth of the spectrum in the simulation is $bw = 10\Omega_0$, $\Omega_0 = 1\pi$ MHz.	71
3.10 (a: π pulse; b: 2π pulse) Relation between rabi population errors and the center frequency of the servo bump f_g . $h_g = 1100$ Hz ² /Hz, $\sigma_g = 1.4$ kHz. Ω_0 is the Rabi frequency.	72
3.11 (a: π pulse; b: 2π pulse) Errors predicted by Equation (3.146) in the quasi-static model and errors calculated by numerical simulations. $\Omega_0 = 1 \times 2\pi$ MHz.	73
3.12 (a: π pulse; b: 2π pulse) Relation between errors and the bandwidth of the frequency noise spectrum. $\Omega_0 = 1 \times 2\pi$ MHz.	74
3.13 (a,c: π pulse; b,d: 2π pulse; a,b: $F_c = 0.1\Omega_0$; c,d: $F_c = 10\Omega_0$) Relation between errors and the RIN level of the intensity noise. F_c is the bandwidth of the intensity noise spectrum. $\Omega_0 = 1 \times 2\pi$ MHz.	75
3.14 (a: π pulse; b: 2π pulse) Relation between errors and the linewidth of the laser. Here we assume that the two lasers have the same linewidth in their Lorentzian lineshape. $\tilde{\Omega}_0 = 1 \times 2\pi$ MHz.	76
3.15 (a,c: π pulse; b,d: 2π pulse; a,b: $F_c = 0.1\tilde{\Omega}_0$; c,d: $F_c = 10\Omega_0$) Relation between errors and the RIN level of the intensity noise. F_c is the bandwidth of the intensity noise spectrum. $\tilde{\Omega}_0 = 1 \times 2\pi$ MHz.	77
3.16 (One photon)Blue: T2 time predicted by theory; Red: T2 time simulated from dynamical equations.	79
3.17 (Two photon)Blue: T2 time predicted by theory; Red: T2 time simulated from dynamical equations.	80

4.1	Multi-qubit gate protocols. a) Each atom is described with a 4-level structure: computational basis $ 0\rangle$, $ 1\rangle$, Rydberg state $ r\rangle$, and leakage state $ d\rangle$. In the fully symmetric case each pair of atoms has equal Rydberg coupling B . b) ARP pulses applied to each atom for the C_kZ gate. c) Single Gaussian pulse at fixed detuning applied to each atom for the CZ_k gate.	84
4.2	Numerical results for C_kZ gate fidelities with different control qubit number k and coupling strength B . The gate is implemented with ARP pulses. $\Omega_0/2\pi = 17$ MHz, Rydberg lifetime $\tau = 540\mu s$. $T_{initial} = 0.54\mu s$, $\Delta_{initial}/2\pi = 23$ MHz.	85
4.3	C_kZ fidelity for different values of $B_{min} = B_0 - \Delta B$ values. Parameters are the same as in Fig. 4.2 with $B_0/2\pi = 200$ MHz.	87
4.4	Numerical results for CZ_k gate with different target qubit number k and coupling strength B . $\Omega_0/2\pi = 17$ MHz, Rydberg lifetime $\tau = 540\mu s$. $\delta t_{initial} = 0.2\mu s$, $\Delta_{initial}/2\pi = 23$ MHz.	88
4.5	Fidelities at different target-target(T-T) coupling values as a percentage of control-target(C-T) coupling for $k=2,3$ and 4 with the single Gaussian pulse. $B_0/2\pi = 10.5$ MHz.	89
4.6	Atomic structure for qubit pumping with Cs atoms. The transitions are labeled with the saturation intensity in W/m^2 . The saturation intensity of the transition $ fm\rangle \rightarrow f'm\rangle$ is $I_{fm,f'm} = \epsilon_0 c \hbar^2 \gamma^2 / 4 d_{fm,f'm}^2$ with $d_{fm,f'm}$ the dipole matrix element, and γ the natural linewidth of the $6p_{1/2}$ level.	90
4.7	Geometrical arrangements and choice of Rydberg states for $N = 2, 3, 4, 5$. Using Rydberg ns states with isotropic interactions equal couplings can be achieved for $N = 2, 3, 4$. For $N = 5$ close to equal couplings are possible as discussed in the text.	92
4.8	Choice of Rydberg states for the 4-qubit case. Using Cs $98s$ and $100s$ in a field of $B_z = 6.5$ G all coupling strengths are equalized to within about 5%.	93
4.9	Rb-Cs coupling strengths	93

5.1	(color online) Two species surface code.	95
5.2	Surface-13 layout following[1]. White circles represent data qubits; black circles, syndrome qubits. Dark patches represent X stabilizers; light patches represent Z stabilizers. The circuit of a single plaquette(for example, the plaquette that contains qubit No.0,1,3,4,9) is also shown.	97
5.3	Circuit for one round of X and Z stabilizer measurements on surface-13. Qubits 0–8 are data encoded in Cs atoms and qubits 1_a – 4_a are ancillas encoded in Rb atoms. Hadamard gates are performed with golbal microwave pulses at ω_{Cs} and ω_{Rb}	98
5.4	Decoder for s-13 code. Black circles show possible ancilla flips. Blue or yellow lines show the possible X or Z errors on the listed qubits that could cause the measured qubit flip. For example, a single ancilla flip during an X measurement on 9 could indicates X error on data qubit 1 or 4; ancilla flips on 9 and 10 during an X measurement indicates X error on data qubit 2.	99
5.5	Simulation results using QuaC for stabilizer detection on a single 5-atom plaquette. All qubits were initialized in the superposition state $(0\rangle + 1\rangle)/\sqrt{2}$, and a series of four ancilla-data CZ gates was applied sequentially. Single qubit gates were assumed to have perfect fidelity. The presented fidelity is the overlap between the calculated and ideal final state.	100
5.6	Z stabilizer	100
5.7	X stabilizer	100
B.1	Fidelity of the CZ_k gate with the single Gaussian pulse with variations of the single-qubit rotation phase on the control and the first target qubit. Variation range is $[-\pi/2, \pi/2]$	108
B.2	Fidelity of the C_kZ gate with the ARP pulse with variations of the single-qubit rotation phase on the control and the first target qubit. Variation range is $[-\pi/2, \pi/2]$	109

List of Tables

2.1	Parameters of the bow-tie cavity design.	14
2.2	Parameters of the bow-tie cavity components. Front side is the side of substrate within the cavity.	16
4.1	Fidelity of C_kZ gates with ARP pulses for $k = 2, 3, 4$ with $B/2\pi = 200$ MHz, $\Omega_0/2\pi = 17$ MHz, Rydberg lifetime $\tau = 540\mu s$. $T_{initial} = 0.54\mu s$, $\Delta_{initial}/2\pi = 23$ MHz.	86
4.2	Fidelity of CZ_k gate with single Gaussian pulse for $k = 2, 3, 4$ with $B/2\pi = 10.75$ MHz, $\Omega_0/2\pi = 17$ MHz, Rydberg lifetime $\tau = 540\mu s$. $\delta t_{initial} = 0.2\mu s$, $\Delta_{initial}/2\pi = 23$ MHz	88
A.1	Parameters for CZ_k gate with single Gaussian pulse for $k = 2$, $\Omega_0/2\pi = 17$ MHz, $\delta t_{initial} = 0.2\mu s$, $\Delta_{initial}/\Omega = 0.5$	103
A.2	Parameters for CZ_k gate with single Gaussian pulse for $k = 3$, $\Omega_0/2\pi = 17$ MHz, $\delta t_{initial} = 0.2\mu s$, $\Delta_{initial}/\Omega = 0.5$	104
A.3	Parameters for CZ_k gate with single Gaussian pulse for $k = 4$, $\Omega_0/2\pi = 17$ MHz, $\delta t_{initial} = 0.2\mu s$, $\Delta_{initial}/\Omega = 0.5$	104
A.4	Fidelities for CZ_k gate with single Gaussian pulse for $k = 3, 4, 5$ with different data-data coupling strengths at $B = 10$. B is the coupling strength between control and target qubits. d-d ratio = $B_{data-data}/B$. Gate parameters are the corresponding Δ , δt and local phase numbers for $B = 10$ for $k = 2, 3, 4$	105

A.5 Parameters for C_kZ gate with ARP pulse for $k = 2$, $\Omega_0/2\pi = 17$ MHz, $T_{initial} = 0.54\mu s$, $\Delta_{initial} = 23$ MHz	105
A.6 Parameters for C_kZ gate with ARP pulse for $k = 3$, $\Omega_0/2\pi = 17$ MHz, $T_{initial} = 0.54\mu s$, $\Delta_{initial} = 23$ MHz	105
A.7 Parameters for C_kZ gate with ARP pulse for $k = 4$, $\Omega_0/2\pi = 17$ MHz, $T_{initial} = 0.54\mu s$, $\Delta_{initial} = 23$ MHz	105
A.8 Fidelities for C_kZ gate with single Gaussian pulse for $k = 3, 4, 5$ with dif- ferent inter-atomic coupling strengths at $B_0 = 0$. For $k = 2$, there are 3 different coupling strengths, for $k = 3$, there are 6 different coupling strengths, and for $k = 4$, there are 10 different coupling strengths. For each k number, the coupling strengths are equally spaced between $B_0 - \Delta B$ and $B_0 + \Delta B$. The Ω , Δ , T and single qubit rotation phase paramters are from the $B = 200$ cases for $k = 2, 3, 4$	106

Chapter 1

Introduction

1.1 Quantum Computing Overview

Computers play a very important part in our modern life. Built based on transistors integrated on semiconductor chips, the trend of classical computers is predicted by Moore's law, which states that the number of transistors on an integrated circuit(IC) doubles every two years. As the increase of performance for classical computers has been slowing down in the recent decade due to the physical limitation of the size of a single device, quantum computing has become an alternative computing architecture that provides significant speed up in certain applications.

The basic unit of information in quantum computing is qubit, a two-level system with computational basis states $|0\rangle$ and $|1\rangle$. The ways that a single qubit evolves itself and interacts with other qubits are governed by Quantum Mechanics. By harnessing the quantum-mechanic nature of the qubits, such quantum superposition and quantum entanglement, many quantum algorithms have been proposed to solve computing problems that are hard for classical computers, such as finding prime factors of an integer[2].

Since the 1980s when Richard Feynman first proposed his idea of simulating quantum systems with quantum computers, there has been numerous experiments with different hardware platforms aiming to demonstrate quantum computing and implementing quantum algorithms, including the use of photons[3], ions[4][5], superconductors[6][7], quan-

tum dots[8], and diamond vacancy centers[9]. While all the approaches has advantages and disadvantages, our group has been focusing on quantum computing with neutral atoms[10][11][12][13]. We believe that neutral atoms provide unique benefits for scalable quantum computing, and our experiment is introduced in the next subsection.

1.2 The Atomic Qubit Array(AQuA) Experiment

The Atomic Qubit Array(AQuA) project is our experiment for building a quantum computer prototype with neutral Cesium atom arrays. So far the experiment has demonstrated high-fidelity readout and single-qubit gates[12]. Recent experiments show that a fidelity of 98.3% could be reached for two-qubit gates. The Cesium atoms are initially cooled in a magneto-optic trap(MOT), and then loaded in to an $n \times n$ array of optical traps, formed by crossed laser beams. The trap light is split into n beams with acoustic-optic deflectors(AODs). Adjacent beams are designed to have slightly different frequencies, in order to eliminate the Talbot Effect. The trapping beams are imaged onto the atom trapping region with a NA= 0.7 lens. Atom occupation is determined by collecting atomic fluorescence using NA= 0.7 lenses at opposite faces of the cell and imaging the light onto two separate regions of an EMCCD camera. A 1064 nm tweezer beam is used to rearrange atoms into desired sites for circuit operation. Circuits are decomposed into a universal gate set consisting of global driven by microwaves, local RZ(θ) rotations driven by the 459 nm beam, and CZ entangling gates using simultaneous Rydberg excitation of atom pairs by the 459 and 1040 nm beams. Fig.1.1 shows the experimental layout.

In our recent paper[13], we demonstrated several quantum algorithms on our atomic array, which includes preparation of entangled Greenberger–Horne–Zeilinger (GHZ)[14] states with up to six qubits(showing in Fig.1.2), quantum phase estimation for a chemistry problem[15](showing in Fig.1.3), and the quantum approximate optimization algorithm (QAOA) for the maximum cut (MaxCut) graph problem[16](showing in Fig.1.4).

The goal of this thesis is to report several analytic works that aim to improve the performance of quantum computing with neutral atoms, which includes studies on laser

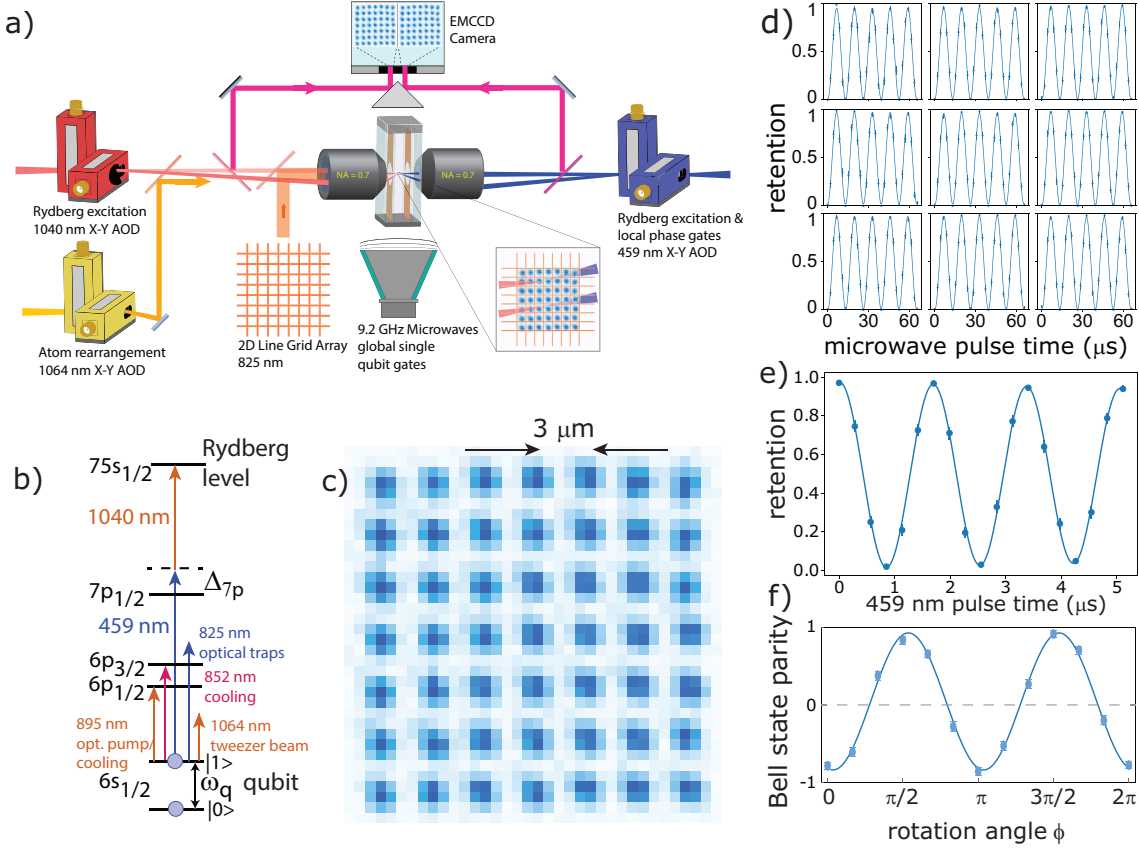


Figure 1.1: a) Experimental layout for trapping and addressing atomic qubits. b) Atomic level diagram and wavelengths used for cooling, trapping, and qubit control. c) Averaged atomic fluorescence image of the 49 site array with spacing $3 \mu\text{m}$. Each camera pixel is $0.6 \times 0.6 \mu\text{m}$ at the atoms. d) Global microwave Rabi rotations on a block of 9 qubits at 76.5 kHz. The microwave phase, amplitude, and frequency are controlled by an arbitrary waveform generator. e) A Ramsey experiment with microwave $\pi/2$ pulses and the focused 459 beam providing an $\text{RZ}(\theta)$ rotation on a single site. f) Parity oscillation of a 2-qubit Bell state created using a CZ gate. The measured and uncorrected Bell state fidelity was 92.7(1.3)% for an optimized qubit pair ($\approx 95.5\%$ corrected for state preparation and measurement (SPAM) errors).

noise, analysis of high-fidelity multi-qubit gate, and the implementation of surface code on neutral atoms.

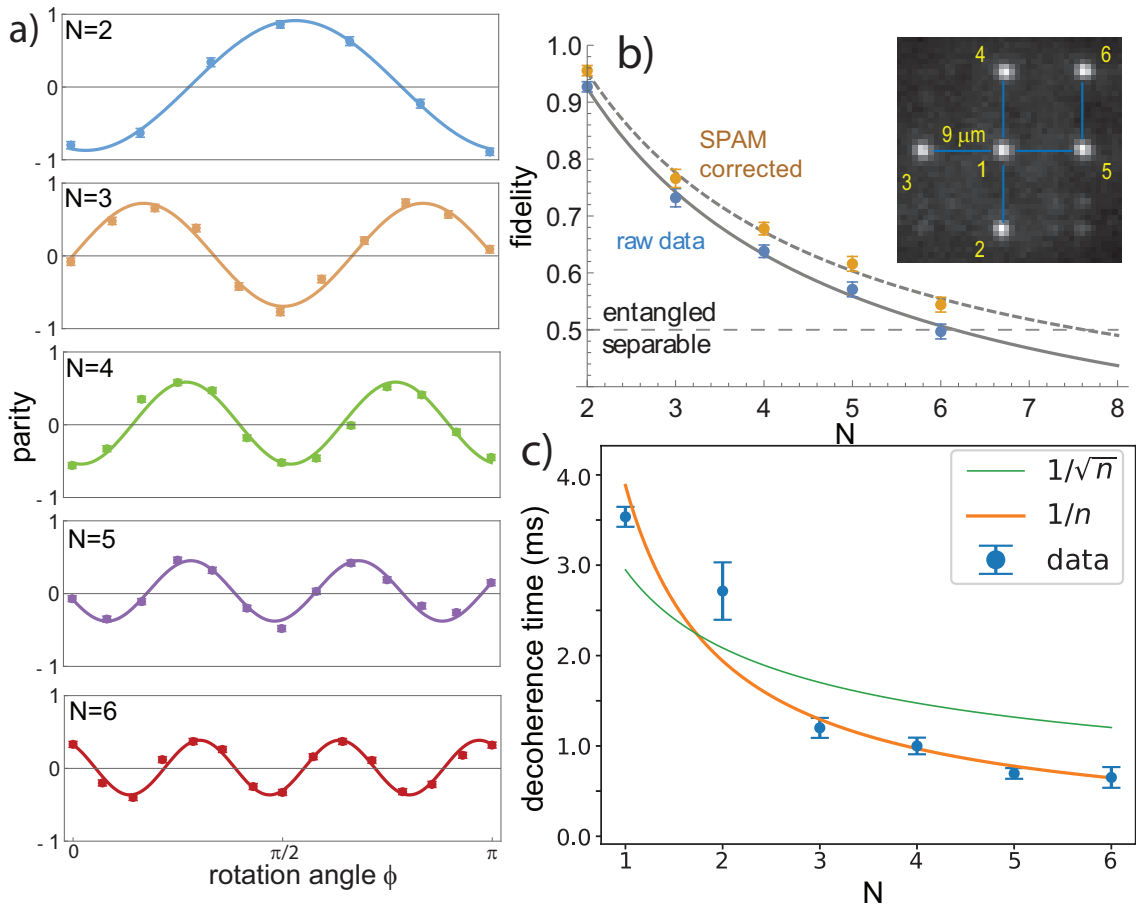


Figure 1.2: Preparation of GHZ states. a) Parity oscillations for GHZ states with 2 – 6 qubits. b) The fidelity of the created GHZ state versus qubit number. c) Decoherence time of GHZ states measured by Ramsey interference.

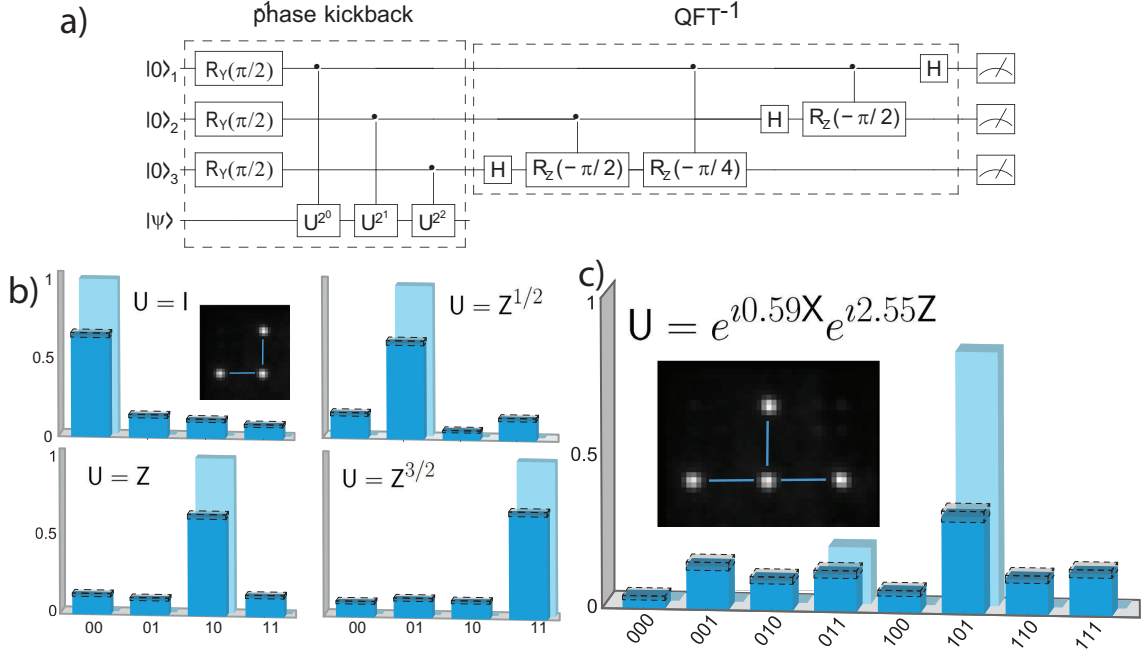


Figure 1.3: Quantum phase estimation using 3 and 4 qubits. a) Phase estimation circuit using 4 qubits. b) Quantum phase estimation results using 3 qubits. c) Quantum phase estimation with four qubits to estimate the molecular energy of a H_2 molecule.

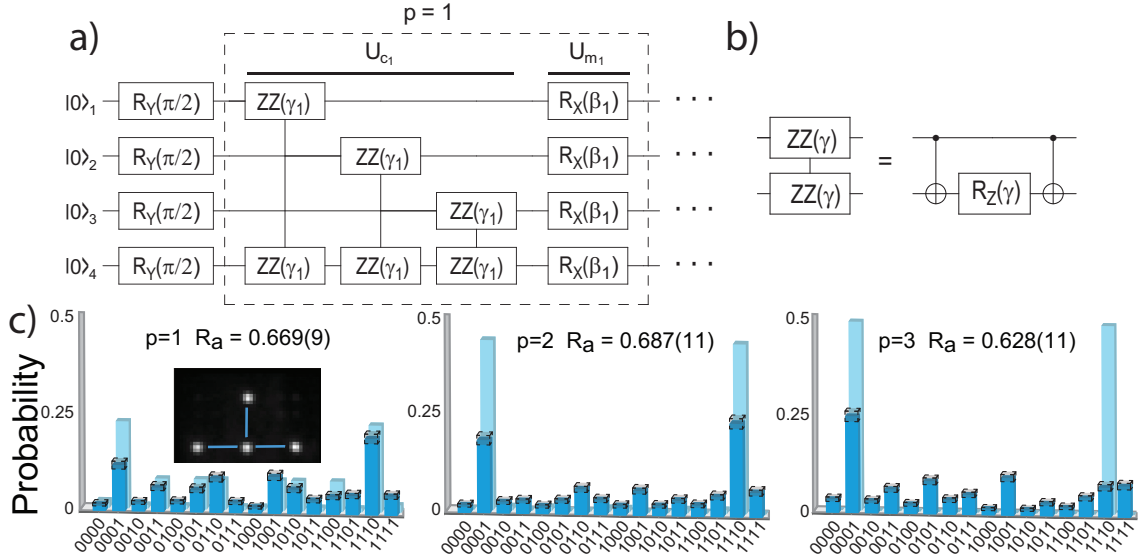


Figure 1.4: QAOA algorithm for solving MaxCut. a) Circuit diagram for 4-qubit QAOA MaxCut showing a single $p = 1$ cycle. b) Decomposition of the $ZZ(\gamma) = e^{-i\gamma/2} Z \otimes Z$ interaction into two CNOT gates and an RZ rotation. c) Circuit results for $p = 1, 2, 3$ with optimized γ and β values.

Chapter 2

Experimental Subsystem Development

As a member of the AQuA team I worked on building various experimental subsystems, including setting up the tapered amplifier(TA) system for the trap lasers, designing a digital-mirror device(DMD) as a Fourier-plane hologram for shaping the Rydberg beam, a filtering cavity for removing the servo bumps of the Rydberg laser, and slow noise-eater for stabilizing the intensity of lasers used in experiments. Here I will focus on introducing the frequency doubling system I built for Rydberg excitation on Rb atoms.

2.1 Frequency Doubling

We use a two-photon ladder scheme to achieve Rydberg excitation for Rb atoms in our Rb-Cs dual species experiment. For Rb atom, the wavelengths are 476nm and 796nm, respectively. Due to the lack of commercially available high power solid-state lasers at visible wavelengths, we perform second-harmonic generation from the 952nm fundamental beam to generate enough 476nm blue light for the experiment.

A high power 952nm fundamental beam is generated by a 2W tapered amplifier purchased from Eagleyard(model:EYP-TPA-0980-02000-4006-CMT04-0000), seeded by a cat-eye external cavity diode laser purchased from Moglabs(dioide model:RWE-0980). The

high power fundamental is then coupled to a bow-tie shaped optical cavity. A piece of nonlinear Lithium Tri-Borate(LBO) crystal purchased from United Crystals is placed between two curved mirrors in the cavity. The configuration of the resonator maximizes the efficiency of second harmonic generation as fundamental light travels through the crystal. To stabilize the frequency of the blue light, the fundamental beam is locked to a high-finesse ultra-low expansion glass(ULE) cavity with Pound-Drever-Hall(PDH) locking technique[17]. The length of the second-harmonic cavity is tuned by a cavity mirror mounted on a piezoelectric transducer, and is locked to the frequency of the 952nm pump beam with Hansch-Coulaud(HC) locking technique[18]. The 476nm blue light is collected from the cavity and coupled into an optics fiber for Rb Rydberg experiments. The layout of the system is shown in Fig. 2.1.

2.1.1 Critical phase-matching

We use an LBO crystal for the 952nm-476nm Second-Harmonic Generation. Compared to the other type of commonly used periodically poled potassium titanyl phosphate(PPKTP) crystals, LBO crystals have less blue light absorption, making them insensitive to the thermal effect in SHG cavities[19][20]. The index of refraction of LBO crystal at 952nm is 1.608. The front and back surfaces of the crystal are Brewster-cut to minimize reflection loss[20][21]. Coating is not necessary for the crystal surfaces, since refection loss is already zero.

Assume the refraction index of the crystal is n , then the Brewster angle θ_b can be calculated by:

$$\theta_b = \arctan(n) \quad (2.1)$$

The crystal will be cut in an isosceles trapezoid shape[22], as Fig. 2.2 shows.

For SHG in an LBO crystal, critical phase matching is needed. First of all we can use Sellmeier's equation to calculate the index of refractions of 952nm and 476nm lights in LBO[23][24]:

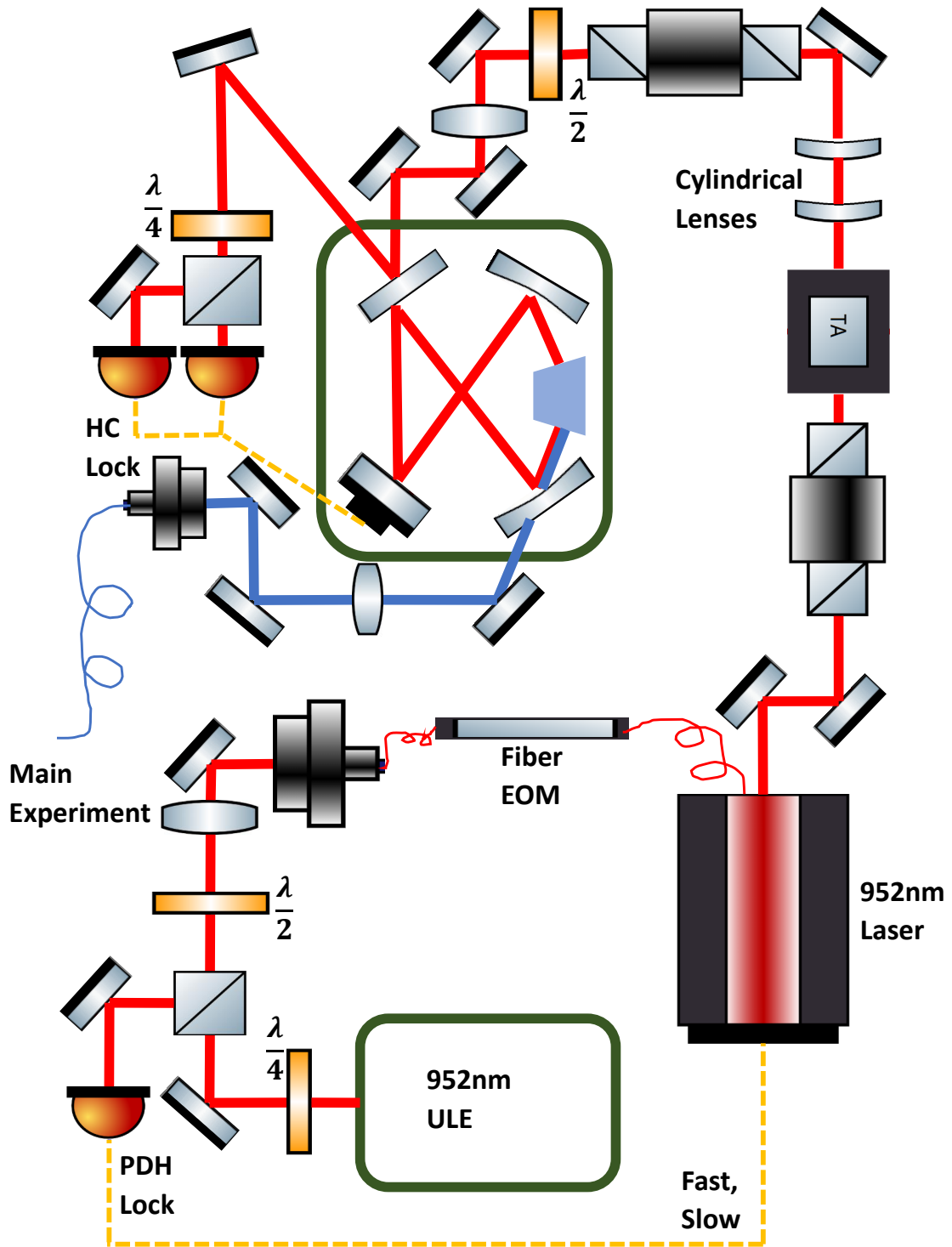


Figure 2.1: Layout of the 952nm-476nm doubling system.

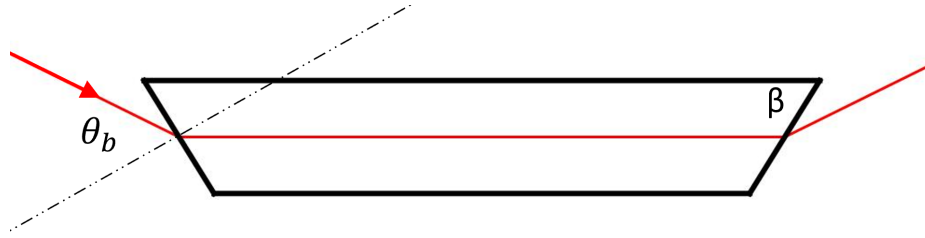


Figure 2.2: Shape of the LBO crystal. The beam enters the crystal at Brewster angle θ_b , and travels through the crystal parallel to the long edges. $\beta = \theta_b$.

$$\begin{aligned} n_x^2 &= 2.4542 + \frac{0.1125}{\lambda^2 - 0.01135} - 0.01388\lambda^2 \\ n_y^2 &= 2.5390 + \frac{0.1277}{\lambda^2 - 0.01189} - 0.01848\lambda^2 \\ n_x^2 &= 2.4542 + \frac{0.1125}{\lambda^2 - 0.01135} - 0.01388\lambda^2 \end{aligned} \quad (2.2)$$

Here λ equals 952nm or 476nm for the fundamental and second-harmonic light, respectively.

However, the factor of temperature has not been taken into consideration. For Brewster-cut crystals coating on crystal surfaces is not needed, and in experiments the performance of Brewster surfaces will be slowly degraded by air humidity. To prevent this, we decide to heat the crystal to about 50 degrees. The temperature-related Sellmeier's equations are[24]:

$$\begin{aligned} n_x^2 &= 2.4542 + \frac{0.1125}{\lambda^2 - 0.01135} - 0.01388\lambda^2 + \\ &(-3.76\lambda + 2.30) \times 10^{-6} \times (\Delta T + 29.13 \times 10^{-3}(\Delta T)^2)) \\ n_y^2 &= 2.5390 + \frac{0.1277}{\lambda^2 - 0.01189} - 0.01848\lambda^2 + \\ &(6.01\lambda - 19.40) \times 10^{-6} \times (\Delta T - 32.89 \times 10^{-4}(\Delta T)^2)) \\ n_x^2 &= 2.4542 + \frac{0.1125}{\lambda^2 - 0.01135} - 0.01388\lambda^2 + \\ &(1.50\lambda - 9.70) \times 10^{-6} \times (\Delta T - 74.49 \times 10^{-4}(\Delta T)^2)) \end{aligned} \quad (2.3)$$

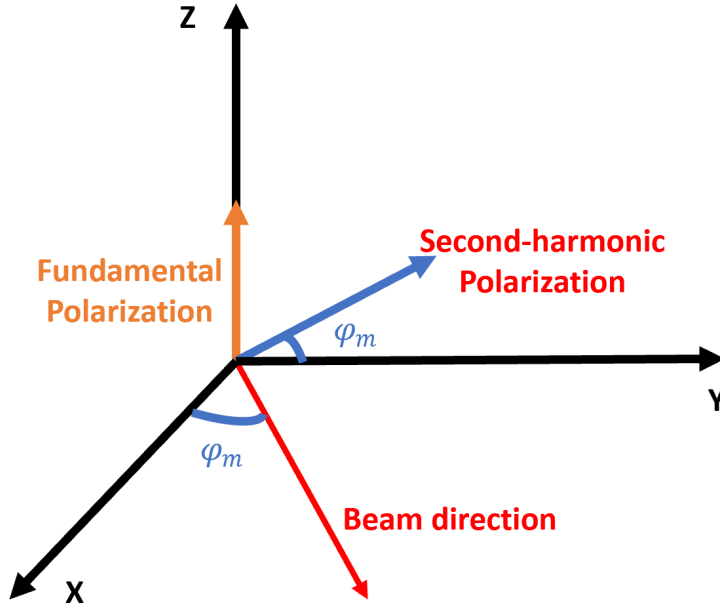


Figure 2.3: Critical phase matching of second-harmonic generation in LBO crystal. ϕ_m is the critical phase-matching angle.

For second-harmonic generation we use type I(ooe) phase matching. The cutting angle is $\theta = 90^\circ$, with the phase-matching angle ϕ_m . By using

$$\phi_m = \arcsin \left(\sqrt{\frac{n_{1z}^{-2} - n_{2y}^{-2}}{n_{2x}^{-2} - n_{2y}^{-2}}} \right) \quad (2.4)$$

we can get the critical phase-matching angle to be $\phi_m = 18.4^\circ$. As Fig. 2.3 shows, in this configuration the fundamental beam has horizontal polarization, and the second-harmonic beam has vertical polarization.

2.1.2 Boyd-Kleimann optimization

We define the power conversion efficiency of the second harmonic generation to be $\epsilon = P_2/P_{in}$, where P_2 is the power of the second harmonic beam, and P_{in} is the power of the fundamental beam. Our goal is to maximize ϵ by choosing appropriate beam parameters and cavity parameters.

Single-pass efficiency with circular beam

To maximize the second-harmonic power, we need to find the optimum configuration for a maximum single-pass conversion efficiency E_{NL} . According to Boyd-Kleimann theory[25], the conversion efficiency E_{NL} through a nonlinear crystal satisfies:

$$E_{NL} = \frac{2\omega_1^2 d^2}{\pi\epsilon_0 c^3 n_1^2 n_2} \frac{L_c}{w_{10}^2} h \quad (2.5)$$

where ω_1 is the angular frequency of the fundamental beam, d is the effective susceptibility, n_1 and n_2 are the corresponding refractive indexes of the fundamental and harmonic beam, L_c is the crystal length, and w_{10} is the waist of the fundamental beam inside the crystal.

h is the Boyd-Kleiman integral, which equals to:

$$h = \int_{-\frac{1}{2}}^{\frac{1}{2}} d\xi' \int_{-\frac{1}{2}}^{\frac{1}{2}} d\xi \frac{e^{i\Delta k L_c (\xi - \xi')}}{1 + i \frac{L_c}{L_{R1}} \xi} \frac{e^{-\frac{2L_c}{L_{R1}} B^2 (\xi - \xi')^2}}{1 - i \frac{L_c}{L_{R1}} \xi'} \quad (2.6)$$

Here L_{R1} is the Rayleigh range of the fundamental Gaussian beam. $L_{R1} = \pi w_{01}^2 / \lambda$

By numerical searching through the expression of E_{NL} , we find the optimum w_{10} and Δk . With $w_{10} = 34.4 \mu m$ and $\Delta k = 119.4 m^{-1}$, the maximum $E_{NL} = 1.25 \times 10^{-4}$.

Single-pass efficiency with elliptical beam

When optimizing conversion efficiency E_{NL} in the previous section, we are assuming that the waist of the fundamental beam at the center of the crystal should be circular. However this condition does not need to be satisfied. The more general expression for E_{NL} is:

$$E_{NL} = \frac{2\omega_1^2 d^2}{\pi\epsilon_0 c^3 n_1^2 n_2} \frac{L_c}{w_{10t} w_{10s}} h \quad (2.7)$$

with B-K integral:

$$h = \int_{-\frac{1}{2}}^{\frac{1}{2}} d\xi' \int_{-\frac{1}{2}}^{\frac{1}{2}} d\xi \frac{e^{i\Delta k L_c (\xi - \xi')}}{\sqrt{1 + i \frac{L_c}{L_{R1t}} \xi} \sqrt{1 + i \frac{L_c}{L_{R1s}} \xi}} \frac{e^{-\frac{2L_c}{L_{R1t}} B^2 (\xi - \xi')^2}}{\sqrt{1 - i \frac{L_c}{L_{R1t}} \xi'} \sqrt{1 - i \frac{L_c}{L_{R1s}} \xi'}} \quad (2.8)$$

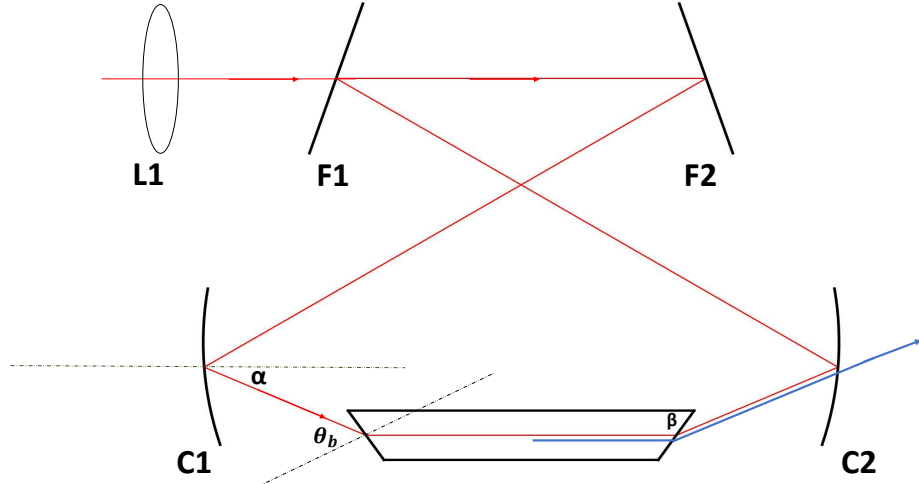


Figure 2.4: Layout of the cavity. L1 is the input coupling lens. F1 is the input coupler. F2 is a flat mirror attached to a piezoelectric transducer for cavity length scanning and locking. C1 and C2 are curved mirrors.

Here d is the effective effective susceptibility, $d = d_{32} \cos \phi_m$, with $d_{32} = -0.9810^{-12}$. L_{R1t} and L_{R1s} are the Rayleigh ranges of the fundamental Gaussian beam in the tangential and sagittal plane. $L_{R1t} = \pi w_{01t}^2 / \lambda$, $L_{R1s} = \pi w_{01s}^2 / \lambda$. w_{01t} and w_{01s} are the tangential and sagittal waist at the center of the crystal, respectively.

By numerical searching the B-K optimal waists are $w_{01t} = 52.2 \mu m$, $w_{01s} = 24.0 \mu m$, with $\Delta k = 117 m^{-1}$. $E_{NL} = 1.48 \times 10^{-4}$.

Although the optimal waists might not be achievable, we can make the beam waist slightly elliptical based on the circular-waist design, which would increase the conversion efficiency. By assuming that $w_{01t}/w_{01s} = 5/4$, we can find the B-K optimal waists: $w_{01t} = 39.846 \mu m$, $w_{01s} = 31.8768 \mu m$, with $\Delta k = 112.899 m^{-1}$. $E_{NL} = 1.42 \times 10^{-4}$.

2.1.3 Cavity design

We are using a bow-tie cavity with two flat mirrors and two curved mirrors to enhance the efficiency of the harmonic generation. An isosceles trapezoid-shaped crystal is placed between the two curved mirrors. The sketch of the cavity is shown in Fig. 2.4.

Assuming that the two curved mirrors have the same radius of curvature, then in the

cavity design we have 4 free parameters: round trip length L , separation between curved mirrors L_2 , mirror incidence angle α , and radius of curvature of the mirrors R . These parameters need to meet the following requirements: the waists of the fundamental beam must be positioned at the center of the crystal; the size of the tangential and sagittal waist should equal to the B-K optimum waist calculated in the previous section.

For a bow-tie cavity with Brewster cut crystals, we can see that the beam reflecting on the curved mirrors are off-axes beams. The incidence angle α cannot be zero. Then as a result, the off-axes beams will bring aberrations, thus degrading the focus and increasing the linear loss in the cavity. It can be noticed that when light is refracting on Brewster surfaces, such distortion will also occur. To compensate for aberrations like coma and astigmatism, we can carefully choose α and R to make the mirror-induced aberrations and crystal-induced aberrations cancel with each other. According to[26] the optimum α and R are:

$$\alpha = \arctan\left(\frac{n^3}{2(n^2 + 1)}\right) \quad (2.9)$$

$$R = \frac{2L_c(n^4 - 1)(n^2 + 1)^{1/2}}{\sin(\alpha)n^7} \quad (2.10)$$

which in our case, $\alpha = 30.1^\circ$, $R = 3.1\text{cm}$.

Then we search two parameters: the total cavity length L_T and the length of light path between the two curved mirrors L_2 , so that the light trapped inside the cavity has tangential and sagittal waists that match the B-K optimum waist at the crystal center. In this condition We get $L_T = 15.6\text{cm}$, $L_2 = 4.65\text{cm}$.

Fig. 2.5 shows the tahttps://www.diffchecker.com/diffngential waist and sagittal waist at the center of the crystal, with respect to the value of L_2 :

The layout of the cavity parameters is shown in Table 2.1

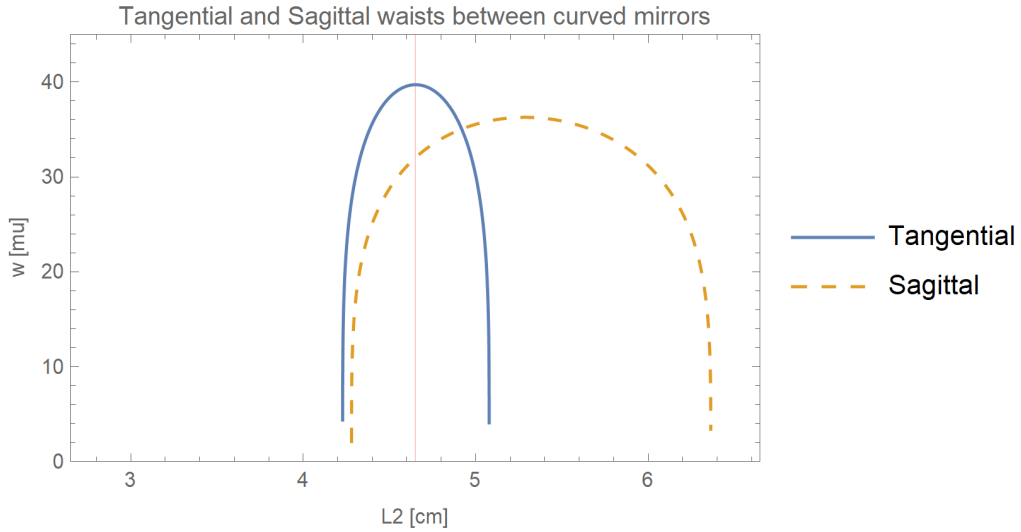


Figure 2.5: Layout of the cavity. L1 is the input coupling lens. F1 is the input coupler. F2 is a flat mirror attached to a piezoelectric transducer for cavity length scanning and locking. C1 and C2 are curved mirrors.

Table 2.1: Parameters of the bow-tie cavity design.

Parameter	Value
L_c	2.15 cm
L_T	15.6 cm
Horizontal distance between F1 and F2	2.56 cm
Horizontal distance between C1 and C2	4.39 cm
Vertical distance between F1 and C1	2.34 cm
Vertical distance between C1 and crystal center	0.55 cm
Flat mirror tilt angle	17.0°
Curved mirror tilt angle	3.9°
Curved mirror radii of curvature R	3 cm
Ideal tangential waist at crystal center	$39.85 \mu\text{m}$
Ideal sagittal waist at crystal center	$31.88 \mu\text{m}$
Tangential waist between flat mirrors	$144 \mu\text{m}$
Sagittal waist between flat mirrors	$110 \mu\text{m}$
Angle α	30.1°

2.1.4 Total conversion efficiency

As the previous section shows, a single pass of the fundamental beam only has conversion efficiency to the order of 10^{-4} . A much higher efficiency can be achieved, by using an enhancement cavity to build up the power of the fundamental light inside the cavity.

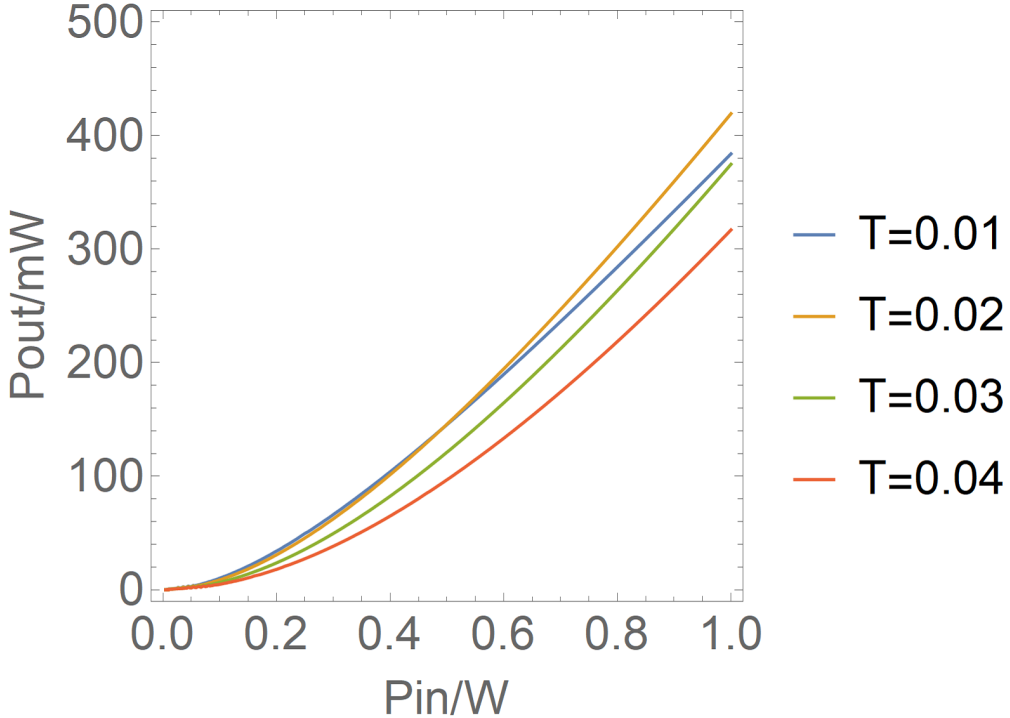


Figure 2.6: Second harmonic power P_{out} vs fundamental beam power P_{in} , at different input coupler transmission coefficient T .

The total conversion efficiency can be written as:

$$\sqrt{\epsilon} = \frac{4T\sqrt{E_{NL}P_{in}}}{[2 - \sqrt{1 - T}(2 - L_0 - \sqrt{\epsilon E_{NL}P_{in}})]^2} \quad (2.11)$$

where T is the transmission coefficient of the cavity's input coupler, L_0 is the additional internal linear loss in cavity, and E_{NL} is the crystal conversion efficiency calculated in the previous section with chosen waist parameters. The conversion efficiency ϵ can then be solved.

Assuming that the linear loss L_0 inside the cavity is 1%, we can make a plot of P_{out} vs P_{in} , as Fig. 2.6 shows. From the figure we can see that maximum conversion efficiency can be obtained at $T = 2\%$ when input fundamental power is 1W.

Table 2.2: Parameters of the bow-tie cavity components. Front side is the side of substrate within the cavity.

Component	Parameter
F_1 front side	$R = 98.0\%$ for 950 nm, p polarization
F_1 back side	AR coating $R < 1\%$ for 950nm, p polarization
F_2, C_1, C_2 front side	$R > 99.9\%$ for 950nm, p polarization $R < 1\%$ for 475nm, s polarization
F_2, C_1, C_2 back side	$R < 1\%$ for 475nm, s polarization
Piezo on F_2	Type P-010.00p, 1000 V

2.1.5 Optical setup and test

The system is designed and built as Fig. 2.1 shows. Two Faraday isolators are used to block the back-propagating beams from entering the TA and the seed laser. A pair of cylindrical lens is used to correct the beam astigmatism caused by the TA. A mode-matching lens is used to couple light into the cavity. The specs of the bow-tie cavity components are listed in Table 2.2. The fundamental beam should have p polarization, and the second-harmonic beam should have s polarization. A $\lambda/2$ wave plate is used to adjust the polarization. A home-made assembly is designed and machined to hold the doubling cavity, as Fig. 2.7 shows.

In experiments with the system, a maximum power of 2.0 W can be achieved when the TA current is 3.2 A. The beam profile coming out from the TA is very irregular. For the waist of the beam before entering the mode-matching lens is measured with a knife-edge method, and by fitting the beam irregular profile to Gaussian the waist is $\approx 700\mu m$. With the target average waist size between F_1 and F_2 being $129\mu m$, the best focal length of the lens is 300mm, calculated by $f = \pi w_{10} w_{20} / \lambda$, where w_{10} and w_{20} are the waist sizes of the beam entering and exiting the lens.

To initially align the cavity and find the second-harmonic generation, I did the following steps:

First, before the mode-matching lens, I coupled the fundamental beam into an optics fiber with 55% coupling efficiency, and shaped the beam coming out of the fiber to have a

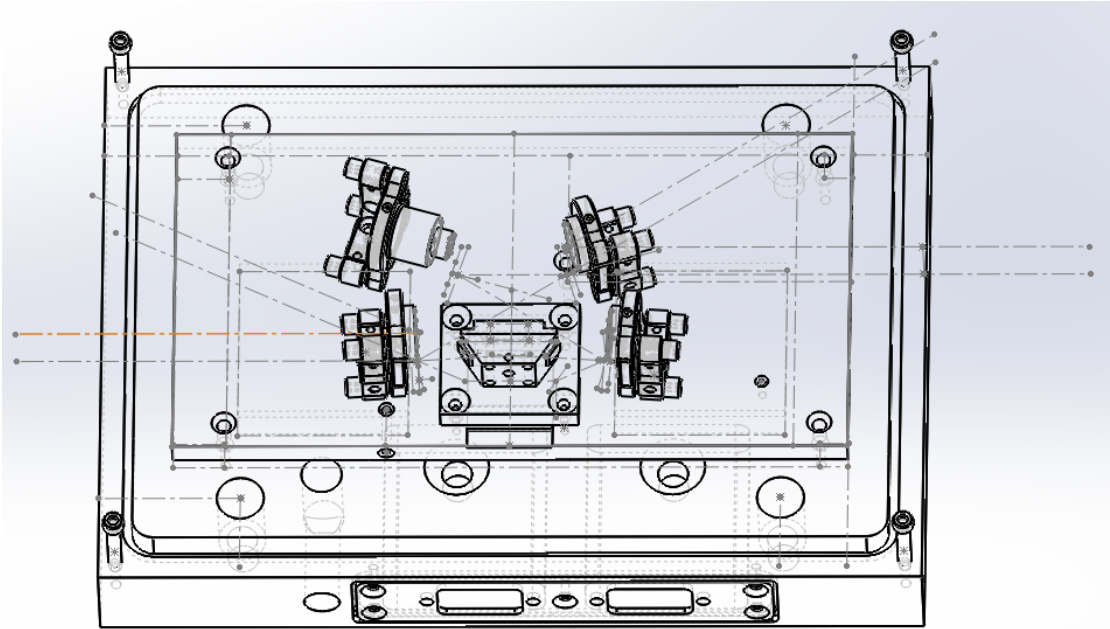


Figure 2.7: Design of the cavity assembly. The temperature of the crystal is stabilized through the thermometric cooler(TEC) under the trapezoid-shaped crystal holder. The temperature of the base plate where the mirrors are mounted is also stabilized with TECs under the plate, in order to avoid thermal drifts of cavity length. A cavity lid(not plotted) is also designed to minimize air turbulence. A band-pass input window for fundamental light and an output window for blue light is mounted on the lid. The electrical feed-through provides access to the piezo and two TECs.

waist of $700\mu m$. Then input coupler F_1 and cavity mirror C_2 is removed. The light passes through the crystal, and a dim blue light spot could be observed. This verifies that there are no problems with the crystal and that the cavity design could work.

Second, still with the fiber in the system, F_1 and C_2 are installed back into the system. The fundamental beam is from the fiber is coupled into the cavity by maximizing the reflection dips from input coupler while scanning the cavity length through the piezo. Then the 476nm blue light is collected from the cavity, and the blue light power is further maximized by tuning the cavity mirrors. A maximum of 67.5mW blue light is observed. This step is to initially align the cavity mirrors.

Finally, I removed the fiber and coupled the irregular-profiled fundamental beam into the cavity, by tuning the two flat mirrors in front of the cavity and keeping the cavity lid closed. A maximum of 70mW 476nm blue light could be observed. The cavity length is

locked to the fundamental frequency with Hansch-Couillaud(HC) lock, by feeding back to the piezo glued on the back of cavity mirror F_2 .

The fundamental frequency is locked to an ultra-low expansion glass(ULE) cavity with Pound-Drever-Hall(PDH) technique. The cavity consists of a piece of 100 mm ULE glass with a cavity mirror on either end. One mirror is planar and the other has a radius of curvature of 500 mm. A fiber samples a portion of the seed beam through the fiber coupler built in the Moglabs laser, passes through the iXblue(NIR-MPX800-LN-10-P-P-FA-FA) fiber EOM to add a sideband of 80MHz. The light is coupled to the cavity, and the reflection from the cavity front mirror is measured by a photodiode. The signal was fed into a home-built PDH error signal box, as Fig. 2.8 shows.

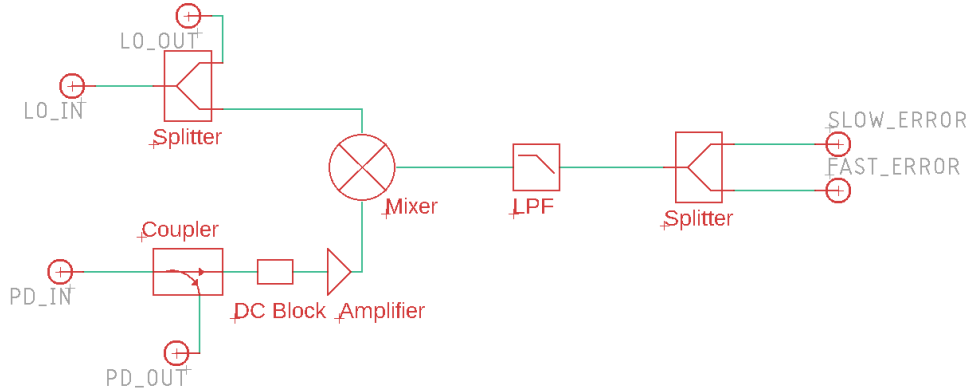


Figure 2.8: PDH error signal box.

The fast error signal is processed by a Moglabs servo generator, and fed into the built-in servo controller in the Moglabs laser with the slow error signal from the box. The feedback polarity, gain and vertical and horizontal offset can be tuned on both the servo generator and the built-in controller. Fig. 2.9 and Fig. 2.10 shows the error signal and one of the ULE cavity mode that the laser is locked to.

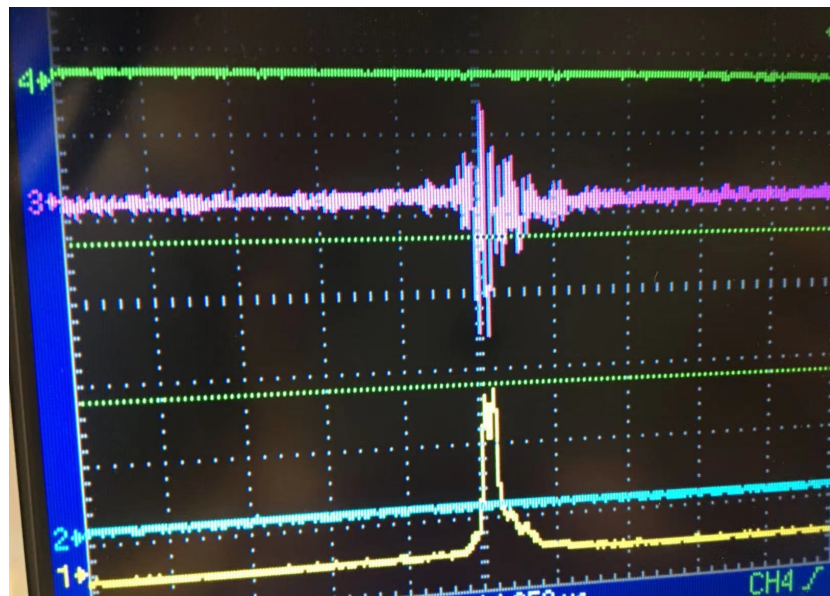


Figure 2.9: Pink: error signal; Yellow: error transmission.



Figure 2.10: ULE cavity transmission taken by a Raspberry-Pi camera. The laser is locked to a stable mode of the cavity.

Chapter 3

Laser Noise Analysis

Logical gate operations on matter qubits rely on coherent driving with electromagnetic fields. For solid state qubits these are generally at microwave frequencies of 1-10 GHz. For atomic qubits microwave as well as optical fields with carrier frequencies of several hundred THz are used for gates. High fidelity gate operations require well controlled fields with very low amplitude and phase noise. In this section we quantify the influence of control field noise on the fidelity of qubit gate operations. While we mainly focus on the case of optical control with visible or infrared lasers, our results are also applicable to high fidelity control of solid-state qubits with microwave frequency fields.

We develop a detailed theory of the dependence of gate fidelity on the noise spectrum of the driving field. We present a summary of the theory of the laser lineshape and its' relation to self-heterodyne spectral measurements. We will also show that the spectral distribution of noise relative to the Rabi frequency of the qubit drive is an important parameter that determines the extent to which noise impacts gate fidelity. When the noise spectrum is peaked near the Rabi frequency, the deleterious effects are most prominent.

3.1 Laser Noise As Random Process

3.1.1 Random Process

A continuous-time random process is a family of random variables $\{X_t\}$ where t ranges over a specific range of time. For every specific t , X_t is a random variable.

The **mean function** of a random process is defined as:

$$m_X(t) = \mathbb{E}[X_t] \quad (3.1)$$

If X_{t_1} and X_{t_2} are two random variables from a random process X_t , then their **correlation function** is defined as:

$$R_X(\tau) = \langle X(t)X(t + \tau) \rangle \equiv \lim_{T \rightarrow \infty} \frac{1}{2T} \int_{-T}^T X(t)X(t + \tau) dt. \quad (3.2)$$

The correlation function reflects how smooth or wiggly a process is.

We say that a process $\{X_t\}$ is **wide-sense stationary (WSS)** if the following two properties both hold:

- (i) The mean function $\mathbb{E}[X_t]$ does not depend on t .
- (ii) The correlation function $E[X_{t_1}X_{t_2}]$ depends on t_1 and t_2 only through the time difference $\tau = t_1 - t_2$:

$$R_X(\tau) = \mathbb{E}[X_{t+\tau}X_t] \quad (3.3)$$

For a WSS process $\{X_t\}$ it is very convenient to work with the **Fourier Transform** of the correlation functions (Wiener-Khinchin theorem):

$$S_X(f) = \int_{-\infty}^{\infty} R_X(\tau) \exp(-i2\pi f\tau) d\tau \quad (3.4)$$

The inverse transform is then:

$$R_X(\tau) = \int_{-\infty}^{\infty} S_X(f) \exp(i2\pi f\tau) df \quad (3.5)$$

We say that a process $\{X_t\}$ is **ergodic** if its statistical properties can be deduced from a sufficiently long random sample of the process. Detailed definition of ergodicity can be found in [27]. With $\{X_t\}$ being ergodic we can compute $R_X(\tau)$, which by definition is the ensemble average of $X_{t+\tau}X_t$ over the sample space, by averaging it in a sufficiently long time period:

$$R_X(\tau) = \lim_{T \rightarrow \infty} \frac{1}{2T} \int_{-T}^T X_{t+\tau}X_t dt \quad (3.6)$$

The **expected average power** of a random process $\{X_t\}$ is defined as:

$$P_X = \mathbb{E}[\lim_{T \rightarrow \infty} \frac{1}{2T} \int_{-T}^T X_t^2 dt] \quad (3.7)$$

If $\{X_t\}$ is WSS, then this becomes:

$$P_x = \lim_{T \rightarrow \infty} \frac{1}{2T} \int_{-T}^T \mathbb{E}[X_t^2] dt = \lim_{T \rightarrow \infty} \frac{1}{2T} \int_{-T}^T R_X(0) dt = R_X(0) \quad (3.8)$$

Since R_X and S_X are Fourier transform pairs:

$$R_X(0) = \int_{-\infty}^{\infty} S_X(f) df \quad (3.9)$$

So we have:

$$P_X = \mathbb{E}[X_t^2] = R_X(0) = \int_{-\infty}^{\infty} S_X(f) df \quad (3.10)$$

Suppose we want to calculate the power of $\{X_t\}$ in the frequency band $f_1 \leq |f| \leq f_2$. We

can calculate the average power of $\{Y_t\}$, where $\{Y_t\}$ is $\{X_t\}$ band-pass-filtered between f_1 and f_2 in the frequency domain:

$$\begin{aligned}
 P_Y &= \int_{-\infty}^{\infty} S_Y(f) df \\
 &= \int_{-f_2}^{-f_1} S_X(f) df + \int_{f_1}^{f_2} S_X(f) df \\
 &= 2 \int_{f_1}^{f_2} S_X(f) df \\
 &= \int_{f_1}^{f_2} S_X^{1-sided}(f) df
 \end{aligned} \tag{3.11}$$

1-sided spectrum will be explained later in following sections.

Here we see that when integrated over a frequency band, $S_X(f)$ gives the process's power in that band. $S_X(f)$ is called the **power spectral density** of the process.

It can be proved that the power spectral density function $S_X(f)$ is a real, even and nonnegative function. We can infer these properties from $R_x(\tau)$ being real and even, and equation 3.10 where $\int_{-\infty}^{\infty} S_X(f) df = \mathbb{E}[X_t^2]$. Detailed analysis can be found in [27].

In mathematics, the Wiener process(also called Brownian motion), is the integral of a white noise signal:

$$W(t) = \int_0^t W_0(t) dt \tag{3.12}$$

Here $W(t)$ is the Wiener process, and $W_0 = \frac{dW(t)}{dt}$ is a process with flat power spectral density:

$$S_0 = h_0 \tag{3.13}$$

One can then inform from the property of fourier transform that:

$$S_W = \frac{h_0}{(2\pi f)^2} \tag{3.14}$$

For $0 \leq s \leq t, t - s = \tau$, as introduced in [28], for $W_0(t)$ with a flat power spectral

density $S_0 = h_0$, it has an Allan variance of:

$$\sigma_0^2(\tau) = \frac{h_0}{2\tau} \quad (3.15)$$

Then as the time-integral of $W_0(t)$, $W(t)$ has an Allan variance of:

$$\sigma_W^2(\tau) = \tau^2 \sigma_0^2(\tau) = \frac{h_0 \tau}{2} \quad (3.16)$$

For a random process $y(t)$ measured at t and $t + \tau$, its Allan variace is defined as:

$$\sigma_y^2(\tau) = \frac{1}{2} \mathbb{E}[(y_{t+\tau} - y_t)^2] \quad (3.17)$$

For Wiener process $W(t)$ defined as above,

$$\mathbb{E}[(W_{t+\tau} - W_t)^2] = h_0 \tau \quad (3.18)$$

3.1.2 Features of Laser Noise

To use our knowledge in the previous chapter we need to do the following assumptions and clarifications before we start modeling:

1. Laser noises, including frequency/phase/intensity noise, are all random processes at time range $t \geq 0$.
2. Laser noises are wide-sense-stationary(WSS) processes.
3. Laser noises are ergodic.
4. Laser noises as well as other real-world signals only have positive components in their spectrum. The spectrum that we see on a spectrum analyzer is a one-sided spectrum. For power spectral density $S_X(f)$, considering it being real and even, it has the property:

$$S_X^{1-sided}(f) = 2S_X^{2-sided}(f) \quad (3.19)$$

Here $S_x^{1-sided}(f)$ are defined on $0 \leq f \leq \infty$.

The Wiener-Khinchin theorem for $S_x^{1-sided}(f)$ is then:

$$S_X^{1-sided}(f) = 4 \int_{-\infty}^{\infty} R_X(\tau) \cos(2\pi f\tau) d\tau \quad (3.20)$$

The inverse transform is then:

$$R_X(\tau) = \int_{-\infty}^{\infty} S_X^{1-sided}(f) \cos(2\pi f\tau) df \quad (3.21)$$

In our future study we will limit ourselves to 1-sided spectrums.

3.1.3 Time-series Reconstruction

Suppose we already know the power spectral density $S_X(f)$ for a random process, and from here we want to reconstruct a sample of $\{X(t)\}$. This technique will be important for us, since sometimes we can model or measure the spectrum of laser noises, and we need to generate time-series noise and put it into our simulation program. One way of doing this is to use the deterministic amplitude scheme(DAS) mentioned in [29]. The recipe is as follow:

1. For a continuous $S_X^C(f)$, we can make it discrete by sampling it at frequency $f_k = k\Delta f$. Then for each f_k , the value of the discretized $S_X^D(f_k)$ should be the power contained in the band $[f_k, f_k + \Delta f]$, as we learned in Eq. (3.11). We can get:

$$S_X^D(f_k) = S_X^C(f_k)\Delta f \quad (3.22)$$

Also please note we are using $S_X^C(f)$ as a one-sided power spectral density. This is also true for the rest part of the recipe.

2. Noticing that for a time series $X(t)$, it forms a Fourier pair with the amplitude spectrum $A_X(f_k)$. For a discretized signal, there is a simple relation between the

power spectrum and the amplitude spectrum:

$$|A_X(f_k)| = \sqrt{|S_X^D|} = \sqrt{S_X^C(f_k)\Delta f} \quad (3.23)$$

3. Do a inverse discrete Fourier transform(IDFT) on the amplitude spectrum $A_X(f_k)$ to get a time series. Since S_X^C is real and even we can use a real Fourier transform pair:

$$X(t_j) = \sum_k \sqrt{S_X^C(f_k)\Delta f} \cos(2\pi f_k t_j + \psi_k) \quad (3.24)$$

Here ψ_k is randomly chosen from a uniform distribution of $[0, 2\pi]$, j range from 1 to N, k range from 1 to $N/2$, where N is the sampling number, $t_k = k\Delta t$, and by Nyquist sampling theorem, $\Delta t = 1/(N\Delta k)$.

Eq. (3.24). has a factor of 2 difference compared with the expression in [29]. This is because we are using a 1-sided power spectral density here.

One concern here is how we should assign the sampling interval Δk for $S_X^C(k)$. I think in principle a larger k will give a more precise result, since we are approximating the integral in Eq. (3.11) to the area of the column in Eq. (3.19). However for white noise, which is has a uniform spectral density, Δk should not matter since in this situation there is nothing lost with the approximation in Eq. (3.19).

3.2 Laser Noise Model For Simulation

3.2.1 Phase noise

For a perfect single frequency laser, the electric field of its radiation can be written as:

$$\mathbf{E}(t) = \frac{\hat{\mathbf{e}} E_0}{2} e^{i[2\pi\nu t]} + \text{c.c.}, \quad (3.25)$$

For an intensity-noise-free laser with reasonably stable frequency, the phase of the

radiation from the laser can be a random variable $\phi(t)$ instead of being constantly 0:

$$\mathbf{E}(t) = \frac{\hat{\mathbf{e}} E_0}{2} e^{i[2\pi\nu t + \phi(t)]} + \text{c.c.}, \quad (3.26)$$

We call $\phi(t)$ the phase noise of this laser. $\phi(t)$ is a random process, which means that at any given time t , the phase of the oscillator $\phi(t)$ is a random variable, sampled from a certain distribution.

It will be reasonable to assume that $\phi(t)$ is a WSS process, because suppose we can measure the phase noise of the laser, then the property of the phase noise shouldn't depend on when the measurement was taken. Then we can calculate its auto-correlation function:

$$R_\phi(\tau) = \lim_{T \rightarrow \infty} \frac{1}{2T} \int_{-T}^T \phi(t + \tau) \phi(t) dt \quad (3.27)$$

The power spectral density of $\phi(t)$ is the Fourier transform of $R_\phi(\tau)$:

$$S_\phi(f) = \int_{-\infty}^{\infty} R_\phi(\tau) e^{-i2\pi f \tau} d\tau \quad (3.28)$$

Knowing $S_\phi(f)$ will be an important step for us to simulate and study laser noise.

To simulate phase noise with knowledge of its power spectral density, we can follow the time-series reconstruction technique in section 3.1.3, to get a sample of phase noise $\pi(t)$.

3.2.2 Frequency Noise

For a laser with phase noise, its instantaneous frequency can be defined in the following way:

$$\nu(t) = \frac{1}{2\pi} \frac{d}{dt} (2\pi\nu t + \phi(t)) \quad (3.29)$$

Then for a laser with phase noise, we can instead use the language of frequency noise to describe it, which is: for an oscillator with frequency noise, its frequency ν is no longer

constant, and the frequency drift becomes a time-varying random process:

$$\Delta\nu(t) = \nu(t) - \nu_0 \quad (3.30)$$

Here we assume that the mean function of $\Delta\nu(t)$ is zero.

The relation of phase noise $\phi(t)$ and frequency noise $\Delta\nu(t)$ is:

$$\Delta\nu(t) = \frac{1}{2\pi} \frac{d}{dt} \phi(t) \quad (3.31)$$

One might attempt to write the laser field with frequency noise like the following:

$$\mathbf{E}(t) = \frac{\hat{\mathbf{e}} E_0}{2} e^{i[2\pi(\bar{\nu} + \Delta\nu)t]} + \text{c.c.} \quad (3.32)$$

But actually this expression is only valid when the frequency noise $\Delta\nu$ is a constant, so that $\phi(t) = 2\pi\Delta\nu t$. Otherwise, the accumulated phase drift $\phi(t)$ is not proportionally related to the instantaneous frequency drift $\Delta\nu(t)$.

Assuming the property of the frequency noise $\Delta\nu(t)$ is time-independent, we can calculate its auto-correlation function:

$$R_{\delta\nu}(\tau) = \lim_{T \rightarrow \infty} \frac{1}{2T} \int_{-T}^T \Delta\nu(t + \tau) \Delta\nu(t) dt \quad (3.33)$$

The power spectral density of $\Delta\nu(t)$ is the Fourier transform of $R_{\delta\nu}(\tau)$:

$$S_{\delta\nu}(f) = \int_{-\infty}^{\infty} R_{\delta\nu}(\tau) e^{-i2\pi f \tau} d\tau \quad (3.34)$$

Fourier transform has the following properties, if the transform of $X(t)$ is the following:

$$\mathbb{F}[X(t)] = A_x(f) \quad (3.35)$$

Then the Fourier transform of $X(t)$ becomes:

$$\mathbb{F}[X'(t)] = 2\pi f A_x(f) \quad (3.36)$$

From here we can first get the relation between the amplitude spectrum of frequency noise and phase noise, by using the property of Fourier transform:

$$A_\nu(f) = \mathbb{F}[\nu(t)] = \frac{1}{2\pi} \mathbb{F}[\phi'(t)] = f A_\phi(f) \quad (3.37)$$

Then we can get the power spectral density of phase noise $\Delta\phi(t)$:

$$S_\phi(f) = \frac{S_{\delta\nu}(f)}{f^2} \quad (3.38)$$

3.2.3 Intensity noise

Assume the intensity of the laser is also noisy:

$$I(t) = I_0 + \delta I(t) == I_0(1 + \alpha_I(t)) \quad (3.39)$$

Here $\alpha_I(t) = \delta I(t)/I_0$ is the **relative intensity noise**.

In some context the term **RIN or RIN level** is used to represent the root-mean-square(RMS) value of relative intensity fluctuation:

$$RIN = \sqrt{\mathbb{E}[\alpha_I(t)^2]} = \frac{\sqrt{\mathbb{E}[\delta I(t)^2]}}{I_0} \quad (3.40)$$

Note here it's natural to assume that $\alpha_I(t)$ is WSS, so that the value of RIN is independent of time, and is always specified in the unit of percent or dB.

3.3 Analysis of Self-Heterodyne Spectrum

When the bandwidth of the laser noise spectrum is comparable to the Rabi frequency of the system, it is then no longer valid to assume the noise to simply be a time-invariant

variable.

The self-heterodyne is a powerful method for characterizing the laser noise spectrum, and is widely used in AMO labs. In a self-heterodyne measurement, the power spectral density $S_i(f)$ of the photoelectric current $I(t)$ as a random process, is shown on a spectrum analyzer. $S_i(f)$, is known to provide an estimate for the spectral density of the laser field and frequency fluctuations, $S_E(f)$ and $S_{\delta\nu}(f)$. In this section, we derive these relationships. It's worth to notice that the relation is not necessarily one-to-one, and we will discuss this issue later.

3.3.1 Laser Lineshape

With frequency noise, the amplitude of the laser's field could also be identified as a random process:

$$E(t) = \frac{E_0}{2} e^{i[2\pi\nu t + \phi(t)]} + \text{c.c.}, \quad (3.41)$$

with the autocorrelation function:

$$R_E(\tau) = \langle E(t)E(t + \tau) \rangle. \quad (3.42)$$

The time average in Eq. (3.42) has been evaluated by a number of authors. For completeness, we summarize these derivations here, following the approach of Ref. [30]. Let us begin by assuming the noise process is strongly stationary, so that Eq. (3.42) does not depend on t ; for simplicity, we set $t = 0$. Using Eqs. (3.41) and (3.42) and trigonometric identities, we then have

$$R_E(\tau) = \left\{ \frac{E_0^2}{4} e^{i[2\pi\nu_0\tau + \phi(\tau) + \phi(0)]} + \text{h.c.} \right\} + \frac{|E_0|^2}{2} \left\{ \cos(2\pi\nu_0\tau) \langle \cos[\phi(\tau) - \phi(0)] \rangle - \sin(2\pi\nu_0\tau) \langle \sin[\phi(\tau) - \phi(0)] \rangle \right\}. \quad (3.43)$$

We then assume the phase difference $\Phi(\tau) \equiv \phi(\tau) - \phi(0)$ to be a gaussian random variable centered at $\Phi(\tau) = 0$, with probability distribution

$$p(\Phi) = \frac{1}{\sigma_\Phi \sqrt{2\pi}} e^{-\Phi^2/2\sigma_\Phi^2},$$

and variance $\overline{\Phi^2} = \sigma_\Phi^2$. Here, the bar denotes an ensemble average. According to the ergodic theorem, ensemble and time averages should give the same result, so that

$$\sigma_\Phi^2(\tau) = \langle [\phi(\tau) - \phi(0)]^2 \rangle = 2R_\phi(0) - 2R_\phi(\tau), \quad (3.44)$$

where we note that

$$\langle \phi^2(0) \rangle = \langle \phi^2(\tau) \rangle = R_\phi(0).$$

Again, making use of the ergodic theorem, we have

$$\langle \cos(\Phi) \rangle = e^{-\sigma_\Phi^2/2} \quad \text{and} \quad \langle \sin(\Phi) \rangle = 0, \quad (3.45)$$

which is also known as the moment theorem for gaussian random variables. Finally we note that only biased variables like $\phi(\tau) - \phi(0)$ are gaussian. An unbiased variable like $\phi(\tau) + \phi(0)$ is simply a random phase, for which $\langle \cos[\phi(\tau) + \phi(0)] \rangle = \langle \sin[\phi(\tau) + \phi(0)] \rangle = 0$. Combining these facts, we obtain the important relation [31]

$$R_E(\tau) = \frac{|E_0|^2}{2} \cos(2\pi\nu_0\tau) \exp[R_\phi(\tau) - R_\phi(0)]. \quad (3.46)$$

Note that since ϕ can take any value, $R_\phi(0)$ does not have physical significance on its own; only the difference $R_\phi(\tau) - R_\phi(0)$ is meaningful.

Another useful form for Eq. (3.46) can be obtained from the relation $2\pi\delta\nu(t) = \partial\phi/\partial t$, together with Eq. (3.4) and the stationarity of $R_\phi(t)$, yielding

$$S_{\delta\nu}(f) = f^2 S_\phi(f). \quad (3.47)$$

Applying trigonometric identities, we then obtain the following, well-known results for the laser lineshape [32]:

$$R_E(\tau) = \frac{|E_0|^2}{2} \cos(2\pi\nu_0\tau) \exp \left[-2 \int_{-\infty}^{\infty} S_{\delta\nu}(f) \frac{\sin^2(\pi f\tau)}{f^2} df \right], \quad (3.48)$$

and

$$S_E(f) = \frac{|E_0|^2}{2} \int_{-\infty}^{\infty} \cos(2\pi f\tau) \cos(2\pi\nu_0\tau) \exp \left[-2 \int_{-\infty}^{\infty} S_{\delta\nu}(f') \frac{\sin^2(\pi f'\tau)}{(f')^2} df' \right] d\tau. \quad (3.49)$$

It's common to re-center the lineshape, therefore set $\nu_0 = 0$. We note that $S_E(f)$ is properly normalized here, with $\int_{-\infty}^{\infty} S_E(f) df = |E_0|^2/2$. Thus, fluctuations that broaden the lineshape also reduce the peak height. It's also interesting to see that when there is no noise present [$S_{\delta\nu} = 0$], we see that the laser lineshape immediately reduces to an unbroadened carrier signal: $S_E(f) = (|E_0|^2/2)\delta(f)$.

Another note is that for some analytical calculations (such as the servo-bump analysis, described below, where the noise is the sum of white noise and Gaussian bumps), it may be convenient to separate the noise spectrum into distinct components: $S_{\delta\nu}(f) = S_{\delta\nu,1}(f) + S_{\delta\nu,2}(f)$, corresponding to different physical noise mechanisms. From Eq. (3.48), the resulting lineshapes can then be written as

$$R_E(\tau) = 2|E_0|^{-2} R_{E,1}(\tau) R_{E,2}(\tau), \quad (3.50)$$

where $R_{E,1}(\tau)$ and $R_{E,2}(\tau)$ are the autocorrelation functions corresponding to $S_{\delta\nu,1}(f)$ and $S_{\delta\nu,2}(f)$. Applying the Fourier convolution theorem, we obtain

$$S_E(f) = 2|E_0|^{-2} \int_{-\infty}^{\infty} S_{E,1}(f-f') S_{E,2}(f') df'. \quad (3.51)$$

When $S_{\delta\nu}$ is nonzero but small, as typical for a locked and filtered laser, the exponential

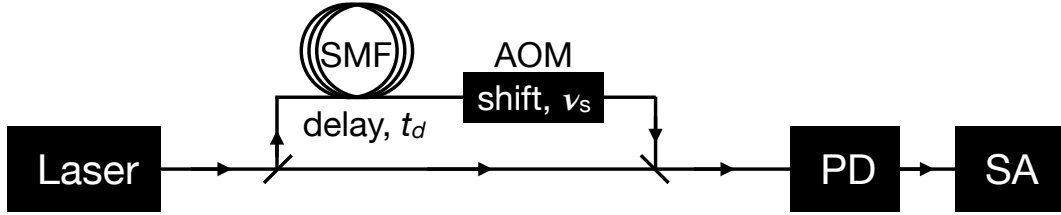


Figure 3.1: Heterodyne setup. The laser signal is split equally between two paths. One path passes through a single-mode fiber (SMF), where it is delayed by time t_d . It then passes through an acousto-optic modulator (AOM), where its frequency is shifted by ν_s . The interfering signals are combined and measured by a photodiode (PD), and finally processed through a spectrum analyzer (SA).

term in Eq. (3.49) may be expanded to first order, yielding [33]

$$2S_E(f)/|E_0|^2 \approx [1 - R_\phi(0)]\delta(f) + S_\phi(f) \quad (3.52)$$

This approximation is generally very good, but breaks down in the asymptotic limit $\tau \rightarrow \infty$ of the τ integral, and therefore the limit $f \rightarrow 0$. To see this, we note that $\sin^2(\pi f \tau)$ may be replaced by its average value of $1/2$ in the integral; for nonvanishing values of $S_{\delta\nu}(0)$, the argument of the exponential then diverges. To estimate the frequency f_x , below which Eq. (3.52) breaks down, we set the argument of the exponential in Eq. (3.52) to $1/2$:

$$2 \int_{f_x}^{\infty} \frac{S_{\delta\nu}(f)}{f^2} df \approx \frac{1}{2}. \quad (3.53)$$

This criterion clearly depends on the noise spectrum.

3.3.2 Self-Heterodyne Spectrum

We consider the self-heterodyne optical circuit shown in Fig. 3.1. As depicted in the diagram, one of the paths is delayed by time t_d , through a long optical fiber, and then shifted in frequency by ν_s , by means of an acousto-optic modulator. Here, the delay loop allows us to interfere phases at different times, while the frequency shift provides a beat tone that is readily accessible to electronic measurements, since it occurs at submicrowave

frequencies, $\nu_s \approx 100$ MHz. The two beams are then recombined and the total intensity is measured by a photodiode, using conventional measurement techniques.

For simplicity, we assume the laser signal is split equally between the two paths, although unequal splittings may also be of interest [34]. The recombined field amplitude is defined as

$$E(t) = \frac{E_0}{2} \left\{ \exp[i2\pi\nu_0 t + i\phi(t)] + \exp[i2\pi(\nu_0 + \nu_s)(t - t_d) + i\phi(t - t_d)] \right\} + \text{c.c.} \quad (3.54)$$

The output current of the photodiode is then proportional to $E^2(t)$. For convenience, we consider instead a dimensionless photocurrent $i(t)$ given by

$$i(t) = \frac{1}{2} \left\{ \cos[2\pi\nu_0 t + \phi(t) + \alpha] + \cos[2\pi(\nu_0 + \nu_s)(t - t_d) + \phi(t - t_d) + \alpha] \right\}^2, \quad (3.55)$$

where $E_0 = |E_0|e^{i\alpha}$. The corresponding autocorrelation function is defined as

$$R_i(\tau) = \langle i(t)i(t + \tau) \rangle. \quad (3.56)$$

The evaluation of $R_i(\tau)$ is greatly simplified by noting that cosine terms with ν_0 in their argument average to zero in a physically realistic measurement. Again making use of the fact that unbiased variables like $\phi(\tau) + \phi(0)$ are random phases and nongaussian, we find that

$$R_i(\tau) = 4 + 2\langle \cos[2\pi\nu_s\tau + \phi(t) - \phi(t - t_d) - \phi(t + \tau) + \phi(t + \tau - t_d)] \rangle. \quad (3.57)$$

Taking the same approach as in the derivation of $R_E(\tau)$, we take $\Phi' = \phi(t) - \phi(t - t_d) - \phi(t + \tau) + \phi(t + \tau - t_d)$ to be a gaussian random variable centered at zero, and apply

the gaussian moment relations,

$$\langle \cos(\Phi') \rangle = e^{-\sigma_{\Phi'}^2/2} \quad \text{and} \quad \langle \sin(\Phi') \rangle = 0, \quad (3.58)$$

where

$$\sigma_{\Phi'}^2 = \langle [\phi(t) - \phi(t - t_d) - \phi(t + \tau) + \phi(t + \tau - t_d)]^2 \rangle. \quad (3.59)$$

In this way we obtain

$$R_i(\tau) = 4 + 2 \cos(2\pi\nu_s\tau) \times \exp[2R_\phi(\tau) + 2R_\phi(t_d) - 2R_\phi(0) - R_\phi(\tau - t_d) - R_\phi(\tau + t_d)]. \quad (3.60)$$

Here, the cosine function represents the beat tone, and the noise information is reflected in its amplitude. It can be seen that the corresponding power spectrum, $S_i(f)$, includes a central peak, $\delta(f)$, which contains no information about the laser noise, and two broadened but identical satellite peaks, centered at $f = \pm\nu_s$. We now recenter $R_i(\tau)$ at one of the satellite peaks, as consistent with typical self-heterodyne measurements, such that

$$R_i(\tau) \rightarrow R_i(\tau) = \exp[2R_\phi(\tau) + 2R_\phi(t_d) - 2R_\phi(0) - R_\phi(\tau - t_d) - R_\phi(\tau + t_d)]. \quad (3.61)$$

Applying trigonometric identities, we then obtain

$$R_i(\tau) = \exp \left[-8 \int_{-\infty}^{\infty} S_{\delta\nu}(f) \frac{\sin^2(\pi f \tau) \sin^2(\pi f t_d)}{f^2} df \right], \quad (3.62)$$

and

$$S_i(f) = \int_{-\infty}^{\infty} \cos(2\pi f \tau) R_i(\tau). \quad (3.63)$$

We note that the self-heterodyne peak defined in this way is normalized such that $\int_{-\infty}^{\infty} S_i(f) df = R_i(0) = 1$.

In the absence of noise [$S_{\delta\nu} = 0$], we see from Eqs. (3.62) and (3.63) that the self-heterodyne power spectrum reduces to the bare carrier: $S_i(f) = \delta(f)$. For nonzero but small $S_{\delta\nu}$, we can expand the exponential in Eq. (3.62), as was done in Eq. (3.52), to

obtain

$$S_i(f) \approx [1 + 2R_\phi(t_d) - 2R_\phi(0)]\delta(f) + 4\sin^2(\pi f t_d)S_\phi(f). \quad (3.64)$$

The second term in this expression is closely related to the envelope-ratio power spectral density described in Ref. [35], following on the earlier work of Ref. [36], and provides a theoretical basis for the former.

As in the derivation of Eq. (3.52), the expansion leading to Eq. (3.64) breaks down at low frequencies. However, the well-known “scallop” features in the power spectrum are seen to arise from the factor $\sin^2(\pi f t_d)$. This result clarifies the relation between the self-heterodyne signal, the underlying laser noise, and the laser lineshape. The latter relation is given by

$$E_0^2 S_i(f) \approx 2\sin^2(\pi f t_d)S_E(f), \quad (3.65)$$

where we have omitted the central carrier peak.

To conclude, we again consider the possibility that the noise spectrum may be separated into distinct components, $S_{\delta\nu}(f) = S_{\delta\nu,1}(f) + S_{\delta\nu,2}(f)$. As for the laser lineshape, the self-heterodyne autocorrelation function may then be written as

$$R_i(\tau) = R_{i,1}(\tau)R_{i,2}(\tau), \quad (3.66)$$

yielding the combined power spectrum

$$S_i(f) = \int_{-\infty}^{\infty} S_{i,1}(f-f')S_{i,2}(f')df'. \quad (3.67)$$

3.4 Retrieving Noise Power Spectral Density from measurements

In the previous chapters we mainly focused on three power spectral densities: $S_i(f)$, $S_E(f)$ and $S_{phi}(f)$. Our aim is, for a given $S_i(f)$ that one observe on the spectrum analyzer in

a self-heterodyne system, we find the corresponding $S_\phi(f)$ which indicates the properties of the laser noise. We can already express $S_i(f)$ (Eq. (3.62)) and $S_E(f)$ (Eq. (3.49)) as integrals of $S_\phi(f)$, however, it's very difficult to do it vice versa, which is to find a distinct expression that gives $S_\phi(f)$ in terms of $S_i(f)$.

To circumvent this issue, what we could do is to first propose a phase noise power spectral density $S_\phi(f)$ with modifiable parameters, then use Eq. (3.62) to calculate the corresponding $S_i(f)$, and compare it to the data measured in self-heterodyne. We keep scanning the parameters until $S_i(f)$ calculated from the proposed noise model fits with the measurements. This is one of the key ideas of our laser noise study.

In the following sections, we will mainly focus on two types of noise, white noise and noise with servo bumps. One could argue that the $S_\phi(f)$ we find in this way might not be the only solution that leads to the given data, or say our noise model is only the necessary condition for the given data. While this is indeed true, we still think this necessary solution is worth studying, and could give important information about the laser phase noise.

3.4.1 White Noise

The self-heterodyne laser noise measurements, reported below, are well described by a combination of white noise and a Gaussian servo bump. We now obtain analytical results for the $S_E(f)$ and $S_i(f)$ power spectra, for these two noise models. The results for white noise are well-known [37]. However we reproduce them here for completeness.

The underlying noise spectrum for white noise is given by

$$S_{\delta\nu} = h_0 \quad \text{or} \quad S_\phi(f) = \frac{h_0}{f^2}. \quad (3.68)$$

Note that it is common to use a one-sided noise spectrum for such calculations; however we use a two-sided spectrum here. Our results may therefore differ by a factor of 2 from others reported in the literature. The most straightforward calculation of $R_\phi(\tau)$, from Eq. (3.5), immediately encounters a singularity. We therefore proceed by calculating $R_E(\tau)$ from

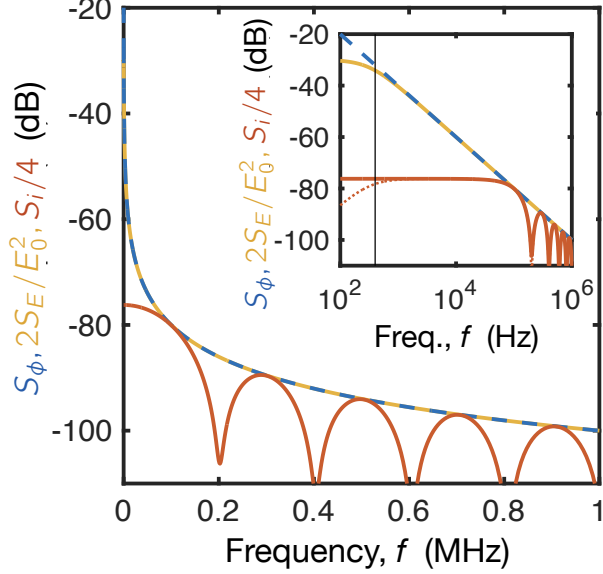


Figure 3.2: White noise power spectral densities: $S_\phi(f)$ (blue) corresponds to Eq. (3.68) with $h_0 = 100$ Hz, $2S_E(f)/E_0^2$ (gold) is obtained from Eq. (3.71)], $S_i(f)/4$ (red) is obtained from Eq. (3.74), omitting the δ -function peak. The inset shows the same quantities, plotted on a logarithmic frequency scale. Here, an approximate form for $S_i/4$ (red, dotted) is obtained from Eq. (3.65). The cutoff frequency f_x (vertical black), obtained from Eq. (3.53), indicates where we expect Eq. (3.52) to fail.

Eq. (3.48). Setting $\nu_0 = 0$, to center the power spectrum, then gives

$$R_E(\tau) = \frac{E_0^2}{2} e^{-2\pi^2 h_0 |\tau|}. \quad (3.69)$$

From Eq. (3.46), we can identify

$$R_\phi(\tau) - R_\phi(0) = -2\pi^2 h_0 |\tau|, \quad (3.70)$$

where the singularity has now been absorbed into $R_\phi(0)$. Solving for the laser lineshape yields

$$S_E(f) = \frac{E_0^2 h_0 / 2}{f^2 + (\pi h_0)^2}, \quad (3.71)$$

for which the FWHM linewidth is $2\pi h_0$. Away from the carrier peak, which is very narrow

for a locked and well-filtered laser, we find

$$2S_E(f)/E_0^2 \approx \frac{h_0}{f^2} = S_\phi(f), \quad (3.72)$$

as consistent with Eq. (3.52).

We can also evaluate the self-heterodyne autocorrelation function, Eq. (3.61), obtaining

$$R_i(\tau) = \exp [-2\pi^2 h_0 (2t_d + 2|\tau| - |\tau - t_d| - |\tau + t_d|)], \quad (3.73)$$

and the corresponding power spectrum,

$$\begin{aligned} S_i(f) &= \frac{2h_0}{f^2 + (2\pi h_0)^2} + e^{-4\pi^2 h_0 t_d} \left\{ \delta(f) \right. \\ &\quad \left. - \frac{2h_0}{f^2 + (2\pi h_0)^2} \left[\cos(2\pi f t_d) + \frac{2\pi h_0}{f} \sin(2\pi f t_d) \right] \right\}. \end{aligned} \quad (3.74)$$

It is interesting to visualize the results and approximations employed above. In Fig. 3.2 we plot the white-noise power spectral densities $S_\phi(f)$, $S_E(f)$, and $S_i(f)$ corresponding to Eqs. (3.68), (3.71)], and (3.74), on both linear and logarithmic scales, for the noise amplitude $h_0 = 100$ Hz. In the inset, we also plot the approximate relation between $S_i(f)$ and $S_E(f)$ given by Eq. (3.65), which clarifies how self-heterodyne measurements may be used to characterize the laser noise. Here, we also plot the crossover frequency f_x from Eq. (3.53), below which the approximations in Eq. (3.65) begin to fail. For the case of white noise, this expression can be evaluated analytically, giving $f_x = 4h_0$.

The scallop features in Fig. 3.2 are caused by beating between the interfering fields in the self-heterodyne circuit. We note that, in principle, all fine-scale noise features present in $S_\phi(f)$ or $S_E(f)$ are transmitted to $S_i(f)$. However the fine features may be obscured by the scallops, which suppress the measured signal at frequency intervals of $\Delta f = 1/t_d$.

3.4.2 Servo bump

A laser can be stabilized by locking it to a narrow-linewidth reference cavity. This feedback system is called a servo loop [33], and the finite bandwidth of the feedback loop induces peaks in $S_{\delta\nu}(f)$ called servo bumps, which are typically shifted above and below the central peak by frequencies on the order of 1 MHz. We find that experimental servo bumps have approximately gaussian shapes. In fact, we find that the full noise model is well described by a gaussian servo bump combined with white noise, as defined by

$$\begin{aligned} S_{\delta\nu}(f) &= h_0 + h_g \exp \left[-\frac{(f - f_g)^2}{2\sigma_g^2} \right] + h_g \exp \left[-\frac{(f + f_g)^2}{2\sigma_g^2} \right] \\ &= h_0 + \frac{s_g f_g^2}{\sqrt{8\pi}\sigma_g} \exp \left[-\frac{(f - f_g)^2}{2\sigma_g^2} \right] + \frac{s_g f_g^2}{\sqrt{8\pi}\sigma_g} \exp \left[-\frac{(f + f_g)^2}{2\sigma_g^2} \right]. \end{aligned} \quad (3.75)$$

Here, h_g is the bump's height and σ_g is its width, with a FWHM given by $\sqrt{\ln 4}\sigma_g$.

In the second line of Eq. (3.75), we use an alternative expression for the bump height, in terms of its total, dimensionless phase-noise power, $s_g = \int_{-\infty}^{\infty} S_{\phi,g}(f)df$, where the subscript g refers to the gaussian noise components. We use this expression in the simulations described below, to explore the effects of different bump shapes. To perform the s_g conversion here, we note that $S_{\phi,g}(f)$ is actually singular at $f = 0$, causing its integral to diverge. We can regularize this divergence by assuming that the servo bump is narrow (which appears to be true in many experiments), and by making the substitution

$$S_{\phi}(f) = S_{\delta\nu}(f)/f^2 \approx S_{\delta\nu}(f)/f_g^2, \quad (3.76)$$

yielding $s_g \approx \sqrt{8\pi}\sigma_g h_g/f_g^2$, which is the form used in Eq. (3.75). We can think of this expression as describing the noise power in just the servo bump, and not the low-frequency portion of the spectrum. We emphasize that the latter is not ignored – but it is subsumed into the white noise, which we treat separately.

We first consider just the gaussian term in Eq. (3.75), setting $h_0 = 0$. Fourier trans-

forming Eq. (3.76), we obtain

$$R_\phi(\tau) \approx s_g \cos(2\pi f_g \tau) e^{-2\pi^2 \sigma_g^2 \tau^2}. \quad (3.77)$$

Thus for $s_g \ll 1$, Eq. (3.52) gives

$$2S_E(f)/E_0^2 \approx \delta(f) + \frac{h_g}{f_g^2} \exp\left[-\frac{(f-f_g)^2}{2\sigma_g^2}\right] + \frac{h_g}{f_g^2} \exp\left[-\frac{(f+f_g)^2}{2\sigma_g^2}\right], \quad (3.78)$$

and Eq. (3.64) gives

$$S_i(f) \approx \delta(f) + \frac{4h_g}{f_g^2} \sin^2(\pi f t_d) \exp\left[-\frac{(f-f_g)^2}{2\sigma_g^2}\right] + \frac{4h_g}{f_g^2} \sin^2(\pi f t_d) \exp\left[-\frac{(f+f_g)^2}{2\sigma_g^2}\right]. \quad (3.79)$$

The white noise component of $S_{\delta\nu}(f)$ can now be included, obtaining Eqs. (3.51) and (3.67), yielding

$$S_E(f) = 2E_0^{-2} \int_{-\infty}^{\infty} S_{E,w}(f-f') S_{E,g}(f') df', \quad (3.80)$$

$$S_i(f) = \int_{-\infty}^{\infty} S_{i,w}(f-f') S_{i,g}(f') df', \quad (3.81)$$

where the subscripts w and g refer to white and gaussian power spectra, which have already been computed. We solve these integrals, approximately, by noting that a convolution between two peaks, with very different widths, is dominated by the wider peak. We further note that, for the lasers of interest here, the servo bump is much wider than the white-noise Lorentzian peak, which is in turn much wider than a delta function. Hence, we find that

$$2S_E(f)/E_0^2 \approx \frac{h_0}{f^2 + (\pi h_0)^2} + \frac{h_g}{f_g^2} \exp\left[-\frac{(f-f_g)^2}{2\sigma_g^2}\right] + \frac{h_g}{f_g^2} \exp\left[-\frac{(f+f_g)^2}{2\sigma_g^2}\right], \quad (3.82)$$

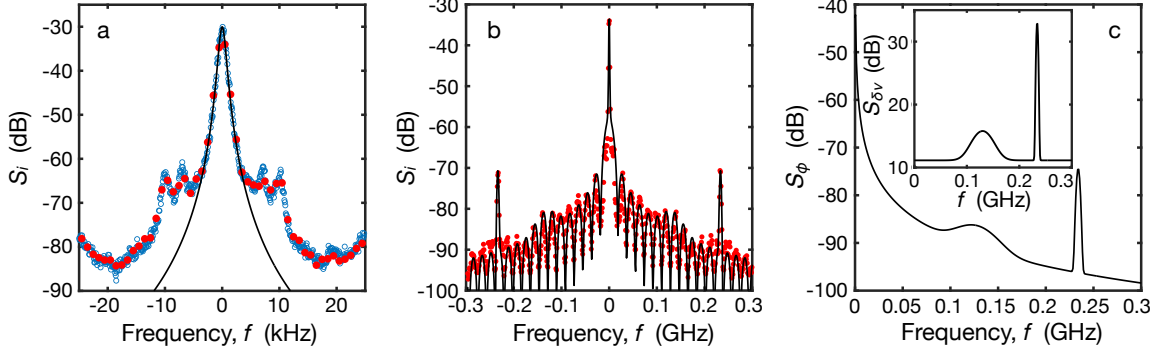


Figure 3.3: 1040 nm solid-state Ti:Sa laser: self-heterodyne data and fits. (a) Self-heterodyne power spectral density, obtained in a 50 kHz frequency window with RBW = 100 Hz (open blue circles), or in a 600 kHz window with RBW = 300 Hz (closed red markers). The data are shifted horizontally so their peaks are centered at zero frequency, and shifted vertically so that they overlap. An optical delay fiber of 11 km is used for both data sets, corresponding to a delay time of $t_d = 5.445 \times 10^{-5}$ s. The data are then fit to Eq. (3.84) (black line), obtaining $\alpha = 5/2$ and $\sigma = 240$ Hz. Finally, all data are renormalized to ensure the correct total power. (b) Same red data set as (a), plotted over a wider frequency window. The data are then fit to Eq. (3.83), including two gaussian servo bumps, obtaining $h_0 = 13$ Hz, $h_{g1} = 2.0$ kHz, $\sigma_{g1} = 1.5$ kHz, $f_{g1} = 234$ kHz, $h_{g2} = 25$ Hz, $\sigma_{g2} = 18$ kHz, and $f_{g2} = 130$ kHz. (c) Phase and frequency power spectral densities, $S_\phi(f)$ and $S_{\delta\nu}(f)$ (inset), resulting from the fitting.

and

$$\begin{aligned} S_i(f) \approx & \frac{2h_0}{f^2 + (2\pi h_0)^2} + e^{-4\pi^2 h_0 t_d} \left\{ \delta(f) - \frac{2h_0}{f^2 + (2\pi h_0)^2} \left[\cos(2\pi f t_d) + \frac{2\pi h_0}{f} \sin(2\pi f t_d) \right] \right\} \\ & + \frac{4h_g}{f_g^2} \sin^2(\pi f t_d) \exp \left[-\frac{(f - f_g)^2}{2\sigma_g^2} \right] + \frac{4h_g}{f_g^2} \sin^2(\pi f t_d) \exp \left[-\frac{(f + f_g)^2}{2\sigma_g^2} \right]. \end{aligned} \quad (3.83)$$

In the following section, we apply these equations as fitting forms for experimental self-heterodyne data.

3.4.3 Laser characterization

To help visualize these results, we now characterize a strongly filtered solid-state Ti:Sa laser used in qubit applications. In Fig. 3.3(a), we plot two experimental data sets from the same laser (red and blue markers). We find that the central peak is broadened more significantly than the RBW settings of the measurement apparatus. The corresponding

linewidths are approximately equal, despite their different RBW, suggesting that RBW is not the only source of broadening.

Although the central peak does not exhibit a clear characteristic form, we find that that it is well described by

$$S_{i,\text{peak}}(f) = \frac{s_p \sigma^{2\alpha-1}}{(f^2 + \pi^2 \sigma^2)^\alpha}. \quad (3.84)$$

Fitting the data to this form yields $\alpha = 5/2$ and $\sigma = 240$ Hz. The corresponding FWHM is 850 Hz, which is indeed several times larger than the RBW of the measurements. Integrating Eq. (3.84) over frequency yields $4s_p/3\pi^4$. The data are therefore shifted vertically in Fig. 3.3(a) to give the correct normalization, $\int_{-\infty}^{\infty} S_i(f) df = 1$.

After this normalization step, the self-heterodyne data away from the peak are fit to Eq. (3.83), where we introduce two distinct servo bumps, obtaining the result shown in Fig. 3.3(b) (black line). The fitting parameters are given by $h_0 = 13$ Hz for the white noise, and $h_{g1} = 2.0$ kHz, $\sigma_{g1} = 1.5$ kHz, $f_{g1} = 234$ kHz, $h_{g2} = 0.025$ kHz, $\sigma_{g2} = 18$ kHz, and $f_{g2} = 130$ kHz for the servo bumps. The corresponding power spectral densities for the noise are plotted in Fig. 3.3(c). We can use these results to determine the fractional noise power in different components of the S_ϕ spectrum. For the first servo bump, we find the fractional power $s_{g1} = 0.00027$, while for the second servo bump, the fractional power is $s_{g2} = 0.00013$. Together, these form a small but non-negligible contribution to the total power.

3.5 Density Matrix Solutions for Rabi Oscillations

3.5.1 Time-Series Expansion of the Laser Noise

In Sec. 3.5.2, below, we solve the density matrix for a qubit undergoing Rabi oscillations, for a given realization $\delta\nu(t)$ of laser frequency noise. We perform an average over all possible noise realizations. These calculations employ a Fourier expansion of the frequency noise, which we now describe.

A real, fluctuating Gaussian process $X(t)$, with zero mean and variance σ_X^2 , can gen-

erally be expressed as a Fourier time series:

$$X(t) = \sum_{j=1}^{\infty} x_j \cos(2\pi f_j t + \varphi_j), \quad (3.85)$$

where $f_j = j\Delta f$. Here, we have defined $X(0) = 0$ for convenience. The random variables x_j can be selected as Rayleigh-distributed random values [38], while the random variables φ_j are uniformly distributed over $[0, 2\pi]$.

We can compute the variance of $X(t)$ as

$$\sigma_X^2 = \left\langle \sum_{j,k} x_j x_k \cos(2\pi f_j t + \varphi_j) \cos(2\pi f_k t + \varphi_k) \right\rangle, \quad (3.86)$$

where an average is taken over the various random variables. Since these variables are assumed to be statistically independent, the double sum vanishes, except for the case $j = k$. Hence,

$$\sigma_X^2 = \sum_{j=1}^{\infty} \langle x_j^2 \rangle / 2. \quad (3.87)$$

The variance is also related to the same-time autocorrelation function, defined in Eq. (3.7), such that

$$\sigma_X^2 = R_X(0) = \int_0^{\infty} S_X^{1\text{-sided}}(f) df = \sum_{j=0}^{\infty} S_{X,j}^{1\text{-sided}} \Delta f, \quad (3.88)$$

where we have used the one-sided version of the noise spectral density function $S_X(f)$. We have also converted the integral to a series representation, with $S_{X,j} = S_X(f_j)$.

Comparing Eqs. (3.87) and (3.88), we see that

$$\langle x_j^2 \rangle = 2S_{X,j}^{1\text{-sided}} \Delta f. \quad (3.89)$$

To generate time traces of $X(t)$, it is then standard practice to make the following replacement for the random variable x_j in Eq. (3.85):

$$x_j \rightarrow \sqrt{2S_{X,j}^{1\text{-sided}} \Delta f} = 2\sqrt{S_{X,j}^{2\text{-sided}} \Delta f}. \quad (3.90)$$

Defined in this way, x_j is deterministic rather than random. The resulting time trace $X(t)$ inherits the correct statistical properties of x_j . Although this procedure cannot account for all random behavior of $X(t)$ [39], it successfully describes most behavior.

The method described above is used to generate random time traces in our numerical simulations, as described in Sec. 3.8. These simulations incorporate time traces of the laser phase fluctuations, defined as

$$\phi(t) = \sum_{j=1}^N 2\sqrt{S_\phi^{2\text{-sided}}(f_j)\Delta f} \cos(2\pi f_j t + \varphi_j). \quad (3.91)$$

Here, we note that, while time-series amplitude coefficients have been replaced by their deterministic averages, the random phases φ_j must still be chosen from the uniform distribution $[0, 2\pi]$. In the following section, we incorporate time traces of the laser frequency fluctuations, defined as

$$\delta\nu(t) = \frac{1}{2\pi} \frac{d\phi}{dt} = \sum_{j=1}^{\infty} \delta\nu_j \sin(2\pi f_j t + \varphi_j), \quad (3.92)$$

where

$$\delta\nu_j = -2\sqrt{S_{\delta\nu}^{2\text{-sided}}(f_j)\Delta f}, \quad (3.93)$$

and we make use of the relation $S_{\delta\nu}^{2\text{-sided}}(f) = f^2 S_\phi^{2\text{-sided}}(f)$. For brevity, we henceforth drop the superscript “2-sided.”

3.5.2 Time-Series Master Equation

We consider a two-level system of frequency ν_e driven resonantly by a monochromatic laser, with Rabi angular frequency Ω_R . We allow for phase fluctuation $\phi(t)$ of the laser, as described by the Hamiltonian

$$H = \frac{\hbar\nu_e}{2}\sigma_z + \hbar\Omega_R \cos(2\pi\nu_e t)[\cos\phi(t)\sigma_x + \sin\phi(t)\sigma_y], \quad (3.94)$$

where $\boldsymbol{\sigma} = (\sigma_x, \sigma_y, \sigma_z)$ are Pauli matrices operating on the two-level system. Moving to a rotating frame defined by $U(t) = \exp(-i\pi\nu_e t \sigma_z)$ and applying a rotating wave approximation (RWA), we obtain the transformed Hamiltonian

$$H' \approx \frac{\hbar\Omega_R}{2} [\cos\phi(t) \sigma_x + \sin\phi(t) \sigma_y]. \quad (3.95)$$

In Eqs. (3.94) and (3.95), the axis of Rabi rotations varies with $\phi(t)$, which captures the physics of the problem, but is inconvenient for our calculations. We therefore consider a frame that follows the fluctuating phase, in which the rotation axis is fixed [40]. This fluctuating frame is defined by the transformation $U_\varphi(t) = \text{diag}[e^{-i\varphi/2}, e^{i\varphi/2}]$, yielding the Hamiltonian

$$\begin{aligned} H'' &\approx \frac{\hbar\Omega_R}{2} \sigma_x - \frac{\hbar(d\phi/dt)}{2} \sigma_z \\ &= \frac{\hbar\Omega_R}{2} \sigma_x - \frac{\hbar\delta\nu(t)}{2} \sigma_z \\ &= \frac{\hbar\Omega_R}{2} \sigma_x - \sum_{j=1}^{\infty} \frac{\hbar\delta\nu_j}{2} \sin(2\pi f_j t + \varphi_j) \sigma_z, \end{aligned} \quad (3.96)$$

where we make use of Eq. (3.92), and the only approximation employed is the standard RWA in Eq. (3.95).

In Eq. (3.96), we have moved to a frame where Ω_R now represents the quantizing field, and where $\delta\nu_j$ represents a Rabi driving term, applied simultaneously at multiple frequencies. To formalize this correspondence, we move to the frame where Ω_R points towards the north pole of the Bloch sphere, as defined by the transformation $U = \exp[-i(\pi/4)\sigma_y]$, obtaining

$$H''' \approx \frac{\hbar\Omega_R}{2} \sigma_z + \sum_{j=1}^{\infty} \frac{\hbar\delta\nu_j}{2} \sin(2\pi f_j t + \varphi_j) \sigma_x. \quad (3.97)$$

For simplicity, we drop the primed notation on H''' in the following derivations.

We now solve for the time evolution of the density operator, for a two-level system governed by Eq. (3.97):

$$\hbar \frac{d\rho}{dt} = i[\rho, H]. \quad (3.98)$$

Although Eq. (3.97) has the standard form of a Rabi rotation, we note that conventional Rabi techniques are not applicable here, because in the frame of Eq. (3.97), the initial state of the system is along the driving axis of the Bloch sphere (\hat{x}), as discussed below. As such, the time evolution arises entirely from counterrotating terms in Eq. (3.97), rather than co-rotating terms. (Note that counterrotating and co-rotating refer, here, to the $\delta\nu_j$ fluctuations, not the original Rabi drive.) Moreover, as will become apparent below, it is desirable to consider perturbative corrections to $\rho(t)$, which are of order $\mathcal{O}[\delta\nu_j^2]$ in the frequency fluctuations.

To construct a perturbation theory, we first note that $2\pi\delta\nu_j$ is typically smaller than Ω_R , allowing us to define the dimensionless small parameter, $\delta_j = 2\pi\delta\nu_j/\Omega_R \lesssim 1$. Defining $\omega_j = 2\pi f_j$, the Hamiltonian becomes

$$\frac{H}{\hbar\Omega_R} = \frac{\sigma_z}{2} + \sum_{j=1}^{\infty} \delta_j \frac{\sigma_x}{2} \sin(\omega_j t + \varphi_j). \quad (3.99)$$

We can then solve the density matrix by expanding in terms of our small parameter,

$$\begin{aligned} \rho &= \rho_0 + \rho_1 + \rho_2 + \dots \\ &= \rho_0 + \sum_{j=1}^{\infty} \delta_j \rho_1^{(j)} + \sum_{j,k=1}^{\infty} \delta_j \delta_k \rho_2^{(j,k)} + \dots, \end{aligned} \quad (3.100)$$

where $\rho_m^{(j,\dots)}$ are assumed to be independent of δ_j . Inserting Eqs. (3.99) and (3.100) into (3.98), collecting terms of equal order in δ_j , and solving up to $\mathcal{O}[\delta_j^2]$ gives

$$\frac{1}{\Omega_R} \frac{d\rho_0}{dt} = i \left[\rho_0, \frac{\sigma_z}{2} \right] \quad (3.101)$$

$$\sum_{j=1}^{\infty} \frac{\delta_j}{\Omega_R} \frac{d\rho_1^{(j)}}{dt} = i \sum_{j=1}^{\infty} \delta_j \left\{ \left[\rho_1^{(j)}, \frac{\sigma_z}{2} \right] + \left[\rho_0, \frac{\sigma_x}{2} \sin(\omega_j t + \varphi_j) \right] \right\}, \quad (3.102)$$

$$\sum_{j,k=1}^{\infty} \frac{\delta_j \delta_k}{\Omega_R} \frac{d\rho_2^{(j,k)}}{dt} = i \sum_{j,k=1}^{\infty} \delta_j \delta_k \left\{ \left[\rho_2^{(j,k)}, \frac{\sigma_z}{2} \right] + \left[\rho_1^{(j)}, \frac{\sigma_x}{2} \sin(\omega_k t + \varphi_k) \right] \right\}. \quad (3.103)$$

For a Rabi driving experiment, in the frame of Eq. (3.94), we consider a qubit initialized to the north pole of the Bloch sphere. In the frame of Eq. (3.99), the corresponding initial

state on the Bloch sphere is \hat{x} , or $\rho(0) = \frac{1}{2}(1+\sigma_x)$. Since ρ_0 , $\rho_1^{(j)}$, and $\rho_2^{(j,k)}$ are independent of δ_j , the initial conditions for the different terms in the density operator expansion are given by $\rho_0(0) = \frac{1}{2}(1 + \sigma_x)$, with $\rho_1(0) = \rho_2(0) = 0$.

Accounting for these initial conditions, it is possible to solve Eq. (3.102), independently, for each $\rho_1^{(j)}$ (results are given below). Making use of uniqueness theorems for Fourier transforms and differential equations, the resulting solution for ρ_1 is unique. Equation (3.102) can therefore be replaced by the decoupled equation

$$\frac{1}{\Omega_R} \frac{d\rho_1^{(j)}}{dt} = i \left[\rho_1^{(j)}, \frac{\sigma_z}{2} \right] + i \left[\rho_0, \frac{\sigma_x}{2} \sin(\omega_j t + \varphi_j) \right]. \quad (3.104)$$

In Eq. (3.103), we note the presence of mixed terms, involving parameters j and k . This is inconvenient; however, in the following derivations, we perform an average over the independent, fluctuating variables $\{\varphi_j, \varphi_k\} \in [0, 2\pi]$, which leads to a helpful simplification. Let us define the averaging procedure as

$$\langle f(\varphi) \rangle_\varphi = \frac{1}{2\pi} \int_0^{2\pi} f(\varphi) d\varphi. \quad (3.105)$$

In the derivations described below, it can be shown that

$$\left\langle \left[\rho_1^{(j)}, \frac{\sigma_x}{2} \sin(\omega_k t + \varphi_k) \right] \right\rangle_{\varphi_j, \varphi_k} = \delta_{jk} \left\langle \left[\rho_1^{(j)}, \frac{\sigma_x}{2} \sin(\omega_j t + \varphi_j) \right] \right\rangle_{\varphi_j}, \quad (3.106)$$

where δ_{jk} is the Kronecker δ -function. As a result, we find that $\langle \rho_2^{(j,k)} \rangle_{\varphi_j, \varphi_k} = \delta_{jk} \langle \rho_2^{(j,j)} \rangle_{\varphi_j} \equiv \delta_{jk} \langle \rho_2^{(j)} \rangle_{\varphi_j}$. Anticipating this step, we can preemptively eliminate the mixed terms in Eq. (3.103), so that the sum runs only over the variable j . As was the case for $\rho_1^{(j)}$, we can then independently solve for each $\rho_2^{(j)}$, obtaining a unique solution for ρ_2 . Equation (3.103) can therefore be replaced by the decoupled equation

$$\frac{1}{\Omega_R} \frac{d\rho_2^{(j)}}{dt} = i \left[\rho_2^{(j)}, \frac{\sigma_z}{2} \right] + i \left[\rho_1^{(j)}, \frac{\sigma_x}{2} \sin(\omega_j t + \varphi_j) \right]. \quad (3.107)$$

Thus, we may solve for the density matrix terms $\rho_1^{(j)}$ and $\rho_2^{(j)}$ independently, and combine

the results for different j values afterwards.

Following the procedure described above, we perturbatively solve for ρ , apply initial conditions, and perform an average over the fluctuating variable φ_j , obtaining

$$\begin{aligned} \langle \rho(t) \rangle &\approx \frac{1}{2} + \left[\frac{1}{2} \cos(\Omega_R t) - \sum_{j=1}^{\infty} \delta_j^2 \frac{2 \cos(\Omega_R t) - 2 \cos(\omega_j t) + (\Omega_R^2 - \omega_j^2)(t/\Omega_R) \sin(\Omega_R t)}{8(\Omega_R^2 - \omega_j^2)^2 / \Omega_R^4} \right] \sigma_x \\ &+ \left[\frac{1}{2} \sin(\Omega_R t) - \sum_{j=1}^{\infty} \delta_j^2 \frac{2 \sin(\Omega_R t) - 2(\omega_j/\Omega_R) \sin(\omega_j t) + (\Omega_R^2 - \omega_j^2)(t/\Omega_R) \cos(\Omega_R t)}{8(\Omega_R^2 - \omega_j^2)^2 / \Omega_R^4} \right] \sigma_y. \end{aligned} \quad (3.108)$$

The perturbative expansion leading up to this result is formally related to a cumulant expansion [41], with an explicit, generalized averaging procedure.

In Eq. (3.108), we note that $\langle \rho \rangle$ diverges for noise occurring near the Rabi frequency, $\omega_j \approx \Omega_R$. Such unphysical behavior is also observed in the Rabi probability formula, $P_{0 \rightarrow 1}(t) = |V_{\text{ac}}/\hbar\Omega|^2 \sin^2(\Omega t)$, when it is Taylor expanded with respect to the small parameter $V_{\text{ac}}/\Delta \lesssim 1$. (Here, $\Omega = \sqrt{\Delta^2 + (V_{\text{ac}}/\hbar)^2}$ is the Rabi frequency and Δ is the detuning.) In the derivation leading to Eq. (3.108), we have employed a similar Taylor expansion with respect to the small parameter $\delta_j = 2\pi\delta\nu_j/\Omega_R \lesssim 1$, obtaining a similar divergence. Further away from $\omega_j = \Omega_R$, we expect Eq. (3.108) to be quite accurate. It is important to be aware of the singular behavior in Eq. (3.108), as it could affect some applications of this theory. However, in the remainder of this work, we focus our attention on quantum gate errors caused by laser noise. Since the singularity in Eq. (3.108) does not appear in such calculations, we simply ignore it from here on.

We now employ Eq. (3.108) to compute quantum gate errors. Specifically, we consider gates defined by the gate times $t = 2\pi N/\Omega_R$ with $N = 1/2, 1, 3/2, \dots$, where $N = 1/2$ corresponds to a π rotation, $N = 1$ corresponds to a 2π rotation, and so on. In the absence of fluctuations ($\delta_j = 0$), the ideal solution for such gates is given by

$$\rho_{\text{ideal}}(N) = \frac{1}{2} + \frac{1}{2}(-1)^{2N} \sigma_x. \quad (3.109)$$

Defining the gate errors as $1 - F$, where $F = \text{tr}[\langle \rho \rangle \rho_{\text{ideal}}]$ is the gate fidelity, and making the substitutions $\omega_j \rightarrow 2\pi f$, $\Delta f \rightarrow df$, and

$$\sum_{j=1}^{\infty} \delta_j^2 \rightarrow \int_0^{\infty} \left(\frac{4\pi}{\Omega_R} \right)^2 S_{\delta\nu}(f) df, \quad (3.110)$$

we obtain

$$\text{error} = (2\pi\Omega_R)^2 \times \int_0^{\infty} S_{\delta\nu}(f) \frac{1 - (-1)^{2N} \cos(4\pi^2 N f / \Omega_R)}{(\Omega_R^2 - 4\pi^2 f^2)^2} df. \quad (3.111)$$

As noted above, this expression remains finite for all f , including $2\pi f = \Omega_R$.

Equation (3.111) is our main result, which may now be applied to cases of interest, including white noise and servo bumps. For the $t = 2\pi N / \Omega_R$ gates, defined above, with white noise defined in Eq. (3.68), we obtain the simple result

$$\text{error} = \frac{\pi^3 h_0 N}{\Omega_R} \quad (\text{white noise}). \quad (3.112)$$

For servo bumps, the frequency noise is defined in Eq. (3.75). To simplify the error calculation, we make use of the fact that the peak in $S_{\delta\nu}(f)$ is typically sharper and narrower than other frequency-dependent terms in Eq. (3.111). This sharp peak can be observed, for example, in Fig. 3.3(c). We therefore make the following substitution in Eq (3.111):

$$S_{\delta\nu}(f) \rightarrow \frac{s_g f_g^2}{2} \delta(f - f_g), \quad (3.113)$$

which yields the following expression for the gate error:

$$\text{error} \approx 2s_g (\pi f_g \Omega_R)^2 \frac{1 - (-1)^{2N} \cos(4\pi^2 N f_g / \Omega_R)}{(\Omega_R^2 - 4\pi^2 f_g^2)^2} \quad (\text{servo bump}). \quad (3.114)$$

As shown in later sections, the largest errors due to servo bumps occur when $\omega_g \approx 2\pi f_g =$

Ω_R . Evaluating Eq. (3.111) in this worst-case scenario gives

$$\text{error} \approx \frac{s_g(\pi N)^2}{4}. \quad (3.115)$$

3.5.3 Two-Photon Gate Fidelity

We can extend the time-series master equation approach to describe two-photon Rabi oscillations, for the excitation scheme shown in Fig. 3.4. We consider a three-level system $\{|g\rangle, |e\rangle, |r\rangle\}$ with level energies given by E_g , E_e , and E_r . We also consider two monochromatic lasers with angular frequencies ω_1 and ω_2 and Rabi angular frequencies Ω_1 and Ω_2 . As before, we allow for phase fluctuations in both lasers, characterized by their individual noise spectral densities, $S_{1,\delta\nu}(f)$ and $S_{2,\delta\nu}(f)$:

$$\phi_i(t) = - \sum_{j=1}^N \delta\nu_{i,j} \cos(2\pi f_j t + \varphi_{i,j}), \quad (3.116)$$

where

$$\delta\nu_{i,j} = -2\sqrt{S_{i,\delta\nu}(f_j)\Delta f}. \quad (3.117)$$

Here, the random phases $\{\varphi_{i,j}\}$ are assumed to be independent for all i and j .

In analogy with Eq. (3.94), the full system Hamiltonian in the laboratory frame is now given by

$$\begin{aligned} H = E_g |g\rangle \langle g| + E_e |e\rangle \langle e| + E_r |r\rangle \langle r| + \hbar\Omega_1 \cos(\omega_1 t) & \left(e^{-i\phi_1} |e\rangle \langle g| + e^{i\phi_1} |g\rangle \langle e| \right) \\ & + \hbar\Omega_2 \cos(\omega_2 t) \left(e^{-i\phi_2} |r\rangle \langle e| + e^{i\phi_2} |e\rangle \langle r| \right) \end{aligned} \quad (3.118)$$

Moving to the rotating frame defined by

$$U(t) = \exp \left[i \left(\frac{2\omega_1 t}{3} + \frac{\omega_2 t}{3} \right) (|e\rangle \langle e| - |g\rangle \langle g|) + i \left(\frac{\omega_1 t}{3} + \frac{2\omega_2 t}{3} \right) (|r\rangle \langle r| - |e\rangle \langle e|) \right] \quad (3.119)$$

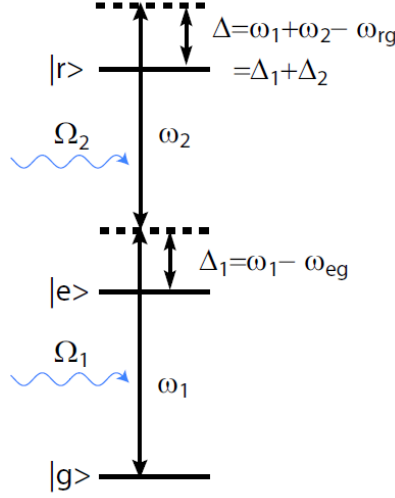


Figure 3.4: Coupling scheme for two-photon Rabi oscillations in a ladder configuration label

and applying an RWA, we obtain

$$H' \approx \frac{\hbar\Delta}{2} |g\rangle\langle g| - \frac{\hbar\delta}{2} |e\rangle\langle e| - \frac{\hbar\Delta}{2} |r\rangle\langle r| + \frac{\hbar\Omega_1}{2} \left(e^{-i\phi_1} |e\rangle\langle g| + e^{i\phi_1} |g\rangle\langle e| \right) + \frac{\hbar\Omega_2}{2} \left(e^{-i\phi_2} |r\rangle\langle e| + e^{i\phi_2} |e\rangle\langle r| \right), \quad (3.120)$$

where we have removed a constant energy term and defined $\hbar\Delta_1 = \hbar\omega_1 + E_g - E_e$, $\hbar\Delta_2 = \hbar\omega_2 + E_e - E_r$, $\Delta = \Delta_1 + \Delta_2$, and $\delta = \Delta_1 - \Delta_2$, as illustrated in Fig. 3.4

As in the previous section, we next move to a fluctuation frame, defined by the transformation

$$U_\phi(t) = e^{-i\phi_1/2-i\phi_2/2} |g\rangle\langle g| + e^{i\phi_1/2-i\phi_2/2} |e\rangle\langle e| + e^{i\phi_1/2+i\phi_2/2} |r\rangle\langle r|, \quad (3.121)$$

yielding the Hamiltonian

$$H'' \approx \frac{\hbar}{2} \left(\Delta + \dot{\phi}_1 + \dot{\phi}_2 \right) |g\rangle\langle g| + \frac{\hbar}{2} \left(-\delta - \dot{\phi}_1 + \dot{\phi}_2 \right) |e\rangle\langle e| + \frac{\hbar}{2} \left(-\Delta - \dot{\phi}_1 - \dot{\phi}_2 \right) |r\rangle\langle r| + \frac{\hbar\Omega_1}{2} (|e\rangle\langle g| + |g\rangle\langle e|) + \frac{\hbar\Omega_2}{2} (|r\rangle\langle e| + |e\rangle\langle r|). \quad (3.122)$$

Now if we assume that $|\delta| \gg \Omega_1, \Omega_2, |\dot{\phi}_1|, |\dot{\phi}_2|$, and that the system wavefunction $|\psi\rangle$ is not initialized into state $|e\rangle$, then at later times we still have $|\langle\psi|e\rangle|^2 \ll 1$. Hence, it is a good approximation to slave $|e\rangle$ to states $|g\rangle$ and $|r\rangle$, such that

$$|e\rangle \approx \frac{\Omega_1}{\delta} |g\rangle + \frac{\Omega_2}{\delta} |r\rangle. \quad (3.123)$$

Eliminating $|e\rangle$ from H'' , we arrive at an effective 2D Hamiltonian describing the dynamical evolution of $|g\rangle$ and $|r\rangle$:

$$H_{2D} \approx \frac{\hbar\tilde{\Omega}_R}{2} \sigma_x - \frac{\hbar}{2} (\Delta_+ + \dot{\phi}_1 + \dot{\phi}_2) \sigma_z, \quad (3.124)$$

where we define $\Delta_+ = \Delta + (\Omega_1^2 - \Omega_2^2)/2\delta$, $\tilde{\Omega}_R = \Omega_1\Omega_2/\delta$, $\sigma_z = |r\rangle\langle r| - |g\rangle\langle g|$, and $\sigma_x = |r\rangle\langle g| + |g\rangle\langle r|$, and we have again removed a constant energy term.

In the absence of noise ($\dot{\phi}_1, \dot{\phi}_2 = 0$), H_{2D} describes rotations tilted slightly away from the x axis, which is undesirable from a gating perspective. This situation can be avoided by adopting the special detuning value defined by the relation $\Delta_+ = 0$, or equivalently,

$$\Delta = \Delta_1 \left(1 - \sqrt{1 + \frac{\Omega_1^2 - \Omega_2^2}{2\Delta_1^2}} \right). \quad (3.125)$$

For this case, we obtain

$$H_{2D} \approx \frac{\hbar\tilde{\Omega}_R}{2} \sigma_x - \frac{\hbar}{2} (\dot{\phi}_1 + \dot{\phi}_2) \sigma_z, \quad (3.126)$$

which maps immediately onto Eq. (3.96) of our previous one-photon analysis.

In the one-photon calculation, we were able to make progress by noting that the random phases φ_j , corresponding to frequency variables ω_j , were independent, yielding additive contributions to the total error in the quantum gates. Now in the two-photon case, the random variables φ_{j1} and φ_{j2} , corresponding to lasers 1 and 2, are also independent; therefore, their contributions to the total error should also be additive. Accounting for the separate power spectral densities in the two lasers, we obtain the following two-photon

results, for gates defined by $t = 2\pi N/\tilde{\Omega}_R$, with $N = 1/2, 1, 3/2, \dots$. For the white noise defined by the parameters h_1 and h_2 in the two lasers, we obtain

$$\text{error} = \frac{\pi^3(h_1 + h_2)N}{\tilde{\Omega}_R} \quad (\text{white noise}). \quad (3.127)$$

For the servo-bump model of laser phase noise, the differences in the lasers are characterized by the total power in the separate servo bumps (s_{g1} and s_{g2}) and their corresponding peak frequencies (f_{g1} and f_{g2}). The resulting error for two-photon gates is given by

$$\begin{aligned} \text{error} \approx & 2s_{g1}(\pi f_{g1}\tilde{\Omega}_R)^2 \frac{1 - (-1)^{2N} \cos(4\pi^2 N f_{g1}/\tilde{\Omega}_R)}{(\tilde{\Omega}_R^2 - 4\pi^2 f_{g1}^2)^2} \\ & + 2s_{g2}(\pi f_{g2}\tilde{\Omega}_R)^2 \frac{1 - (-1)^{2N} \cos(4\pi^2 N f_{g2}/\tilde{\Omega}_R)}{(\tilde{\Omega}_R^2 - 4\pi^2 f_{g2}^2)^2} \quad (\text{servo bump}). \end{aligned} \quad (3.128)$$

3.6 Bandwidth-Limited Phase Noise and the Quasi-static Limit

Narrow bandwidth noise may provide a good approximation for certain highly filtered lasers. In this section, we extend the previous theoretical approach to the case of quasi-static phase noise, where the spectral content of the noise is restricted to very low frequencies. To begin, we consider the more general situation of bandwidth-limited white noise, defined as

$$S_{\delta\nu}(f) = \begin{cases} h_0 & \text{when } |f| \leq f_c, \\ 0 & \text{when } |f| > f_c. \end{cases} \quad (3.129)$$

A noise spectrum of this type could describe a strongly filtered laser with no noise except a broadened carrier signal.

Di Domenico et al. [32] have studied how band-limited white noise is manifested in laser field noise, $S_E(f)$. They observe two distinct behaviors, with an abrupt transition between them occurring at $f_c = \pi^2 h_0 / 8 \ln(2) \approx 1.78 h_0$. When $f_c \gtrsim 1.78 h_0$, $S_E(f)$ takes

the form appropriate for white noise, which we previously characterized in Sec. 3.4.1. When $f_c \lesssim 1.78h_0$, Eqs. (3.49) and (3.63) are readily solved, yielding

$$S_E(f) \approx \frac{|E_0|^2}{\sqrt{16\pi h_0 f_c}} e^{-f^2/4h_0 f_c}, \quad (3.130)$$

$$S_i(f) \approx \sqrt{\frac{3}{16\pi^3 h_0 t_d^2 f_c^3}} e^{-3f^2/16\pi^2 h_0 t_d^2 f_c^3}. \quad (3.131)$$

In the context of Rabi gate operations, when we also have $f_c \ll \Omega_0/2\pi$, we refer to this compressed-noise regime as quasistatic.

The singular nature of quasistatic noise causes the interrelations between $S_\phi(f)$, $S_E(f)$, and $S_i(f)$, embodied in Eqs. ((3.64) and (3.65), to collapse. This is particularly evident in Eq. (3.131) which does not exhibit the scallop features, typical of self-heterodyne measurements. We also note that the FWHM of the broadened carrier signals in Eqs. (3.130) and (3.131) are no longer related and exhibit distinct scaling properties. Hence, $S_i(f)$ may no longer be taken as a proxy for $S_E(f)$.

3.6.1 Master Equation Approach

While $S_{\delta\nu}(f)$, $S_E(f)$, and $S_i(f)$ depend only on h_0 and f_c , Rabi gate errors also depend on Ω_0 . Single-photon gate errors caused by finite-bandwidth white noise can be computed from Eq. (3.111), without approximation, obtaining

$$\begin{aligned} \text{error} = & \frac{\pi h_0}{2\Omega_0} \left\{ \frac{2y[1 - (-1)^{2N} \cos(2\pi Ny)]}{1 - y^2} \right. \\ & + 2\text{Arctanh}(y) + \text{Ci}[2\pi N(1 - y)] - \text{Ci}[2\pi N(1 + y)] \\ & \left. - 2\pi N \text{Si}[2\pi N(1 - y)] + 2\pi N \text{Si}[2\pi N(1 + y)] \right\}, \end{aligned} \quad (3.132)$$

where $\text{Ci}(x)$ and $\text{Si}(x)$ are cosine and sine integral functions ¹, and $y \equiv 2\pi f_c/\Omega_0$.

In the limit $f_c \gg \Omega_0$, we can use Eq. (3.132) to recover the gate-error results obtained in Eqs. (3.112) and (3.127) for ordinary white noise. In the opposite regime, $f_c \lesssim \Omega_0$,

¹Sine and cosine integral functions are defined as $\text{Si}(z) = \int_0^z (\sin t)/t dt$ and $\text{Ci}(z) = -\int_z^\infty (\cos t)/t dt$.

we note that the weak-noise approximation used to derive Eq. (3.132) also requires that $\sqrt{h_0 f_c} \lesssim \Omega_0$, and therefore $h_0, f_c \lesssim \Omega_0$. Hence, for $2\pi N$ Rabi gates, in the quasistatic limit, $h_0, f_c \ll \Omega_0$, we obtain

$$\text{error} \approx \begin{cases} \frac{8\pi^2 h_0 f_c}{\Omega_0^2} & (N = 1/2, 3/2, 5/2, \dots), \\ \frac{32\pi^6 h_0 f_c^3 N^2}{3\Omega_0^4} & (N = 1, 2, 3, \dots). \end{cases} \quad (3.133)$$

These results do not depend on f_c being larger or smaller than h_0 . As in Sec. 3.5.3, the two-photon gate errors are additive, yielding

$$\text{error} = \begin{cases} \frac{8\pi^2(h_1 f_{c1} + h_2 f_{c2})}{\tilde{\Omega}_0^2} & (N = 1/2, 3/2, 5/2, \dots), \\ \frac{32\pi^6(h_1 f_{c1}^3 + h_2 f_{c2}^3)N^2}{3\tilde{\Omega}_0^4} & (N = 1, 2, 3, \dots). \end{cases} \quad (3.134)$$

Qualitatively different types of behavior are observed in Eqs. (3.133) and (3.134) for half vs. full rotations, which can be understood as follows. In the quasistatic limit, frequency noise causes the Rabi rotation axis to shift away from the equator of the Bloch sphere, naturally inducing gate errors. However for the special case of full rotations, the Bloch state returns to its initial value (to leading order in a noise expansion). A secondary effect of the frequency noise is to increase the rotation speed, yielding an over-rotation or under-rotation. However this latter effect is higher-order, resulting in smaller errors for full rotations. In other words, for the special case of full rotations, in the extreme limit of quasistatic noise, the leading order contribution to gate error vanishes; for all other cases, lower-order contributions are present.

We plot Eq. (3.132) in Fig. 3.5, along with results of numerical simulations, for bandwidth-limited white noise. It is evident that our theory captures the majority of the errors arising from such noise spectra. However, the theory breaks down in the limit of large h_0 . Specifically, we find that Eq. (3.132) fails for $h_0 \gtrsim f_c/1.43$. (Failure also requires that $f_c \lesssim \Omega_0/2\pi$.) We attribute the failure of Eq. (3.132) in this regime to the fact that the Master equation derivation in Sec. 3.5 employs an expansion in powers of the

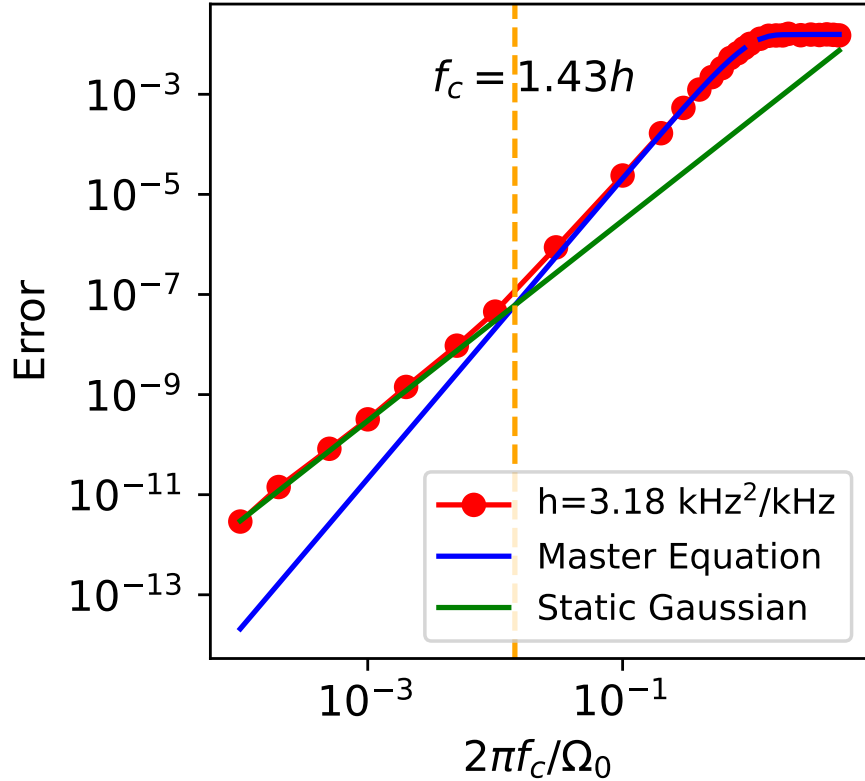


Figure 3.5: Rabi errors for one-photon Rabi oscillations due to band-limited white frequency noise with fixed amplitude $h = 3.18 \text{ kHz}^2/\text{kHz}$, while sweeping the noise bandwidth.

noise strength, retaining only the leading-order term. Hence, for the special case of full rotations, in the quasistatic limit, where the leading-order contribution to the gate error vanishes, our theory does not capture the central physics.

3.6.2 Static Gaussian-Distributed Noise

For phase noise, we can try to use the quasi-static model to get an estimate of the population error.

In this section we only focus on noise spectrum with constant amplitude h and cut-off frequency f_c . The other quantities that are important here are the Rabi frequency Ω_0 , and the laser's full width at half maximum linewidth l which is usually measured in self-heterodyne measurements in labs.

The assumption we make here is that when the bandwidth of the noise spectrum is much less than the Rabi frequency, we can consider the noise to be quasi-static. We can treat the noise as a simple random variable instead of a random process.

Now we assume the laser's frequency drift is also Gaussian distributed. The frequency noise is defined as:

$$\Delta\nu = \nu - \nu_0 \quad (3.135)$$

where ν_0 is the unperturbed optical frequency. Define $x = 2\pi\Delta\nu/\Omega_0$, where Ω_0 is the Rabi frequency for the two level system. Then the Gaussian distribution of x can be the following:

$$f(x) = \frac{1}{\sqrt{2\pi}\sigma} e^{-\frac{x^2}{2\sigma^2}} \quad (3.136)$$

Here $\Delta\nu_{rms} = x\sigma$ is the RMS value for frequency deviation.

For a two-level system resonant with laser frequency ν_0 , the frequency noise will act as detunings. $\Delta = 2\pi\Delta\nu = x\Omega_0$

The population for the excited state $|e\rangle$ in Rabi oscillations is:

$$P_e = \frac{\Omega_0^2}{\Omega_0^2 + \Delta^2} \sin^2\left(\frac{\sqrt{\Omega_0^2 + \Delta^2}t}{2}\right) \quad (3.137)$$

By plugging in $\Delta = x\Omega_0$ and $t = N\frac{2\pi}{\Omega_0}$ we get:

$$P_e = \frac{1}{1+x^2} \sin^2(N\pi\sqrt{1+x^2}) \quad (3.138)$$

The expected value of P_e will be the average over the distribution of x:

$$\mathbb{E}[P_e] = \frac{1}{\sqrt{2\pi}\sigma} \int_{-\infty}^{\infty} \frac{1}{1+x^2} \sin^2(N\pi\sqrt{1+x^2}) e^{-\frac{x^2}{2\sigma^2}} dx \quad (3.139)$$

Then we can get expected value of P_g from the expression above:

$$\mathbb{E}[P_g] = \frac{1}{\sqrt{2\pi}\sigma} \int_{-\infty}^{\infty} [1 - \frac{1}{1+x^2} \sin^2(N\pi\sqrt{1+x^2})] e^{-\frac{x^2}{2\sigma^2}} dx \quad (3.140)$$

We are going to discuss two special cases of N, where N are integers and half integers. In those cases we can simplify the expression for P_e and get an analytical expression for the error.

1. When N is integer, by doing Taylor expansion on the $\frac{1}{1+x^2} \sin^2(N\pi\sqrt{1+x^2})$ term to the fourth order, we can get the following approximation:

$$\frac{1}{1+x^2} \sin^2(N\pi\sqrt{1+x^2}) \approx \frac{N^2\pi^2x^4}{4} \quad (3.141)$$

The integral then becomes:

$$\mathbb{E}[P_e] = \frac{3N^2\pi^2\sigma^4}{4} \quad (3.142)$$

2. When N is half-integer, by doing Taylor expansion on the $\frac{1}{1+x^2} \sin^2(N\pi\sqrt{1+x^2})$ term to the second order, we can get the following:

$$1 - \frac{1}{1+x^2} \sin^2(N\pi\sqrt{1+x^2}) \approx x^2 \quad (3.143)$$

The integral then becomes:

$$\mathbb{E}[P_g] = \sigma^2 \quad (3.144)$$

As a summary, if we start the Rabi oscillation at $P_g = 1$ when $t = 0$, the we have the following expression for errors:

$$\begin{cases} \mathbb{E}[P_g] = \sigma^2, & N=0.5, 1.5, 2.5, 3.5, \dots \\ \mathbb{E}[P_e] = \frac{3N^2\pi^2\sigma^4}{4}, & N=1, 2, 3, 4, \dots \end{cases}$$

Where $N = \frac{\Omega t}{2\pi}$, σ is defined as frequency deviation in terms of Rabi frequency $\sigma = 2\pi\Delta\nu_{rms}/\Omega_0$

In the case of band-limited white noise in the frequency noise spectrum, with band-

width f_c and amplitude h_0 , we have:

$$\sigma^2 = \frac{4\pi^2\nu_{rms}^2}{\Omega_0^2} = \frac{8\pi^2h_0f_c}{\Omega_0^2} \quad (3.145)$$

Then combining it with the expression for Rabi errors, we have:

$$\begin{cases} \text{error} = \frac{8\pi^2h_0f_c}{\Omega_0^2}, & N=0.5, 1.5, 2.5, 3.5, \dots \\ \text{error} = \frac{48\pi^6h_0^2f_c^2N^2}{\Omega_0^4}, & N=1, 2, 3, 4, \dots \end{cases} \quad (3.146)$$

For two photon Rabi oscillations, When there's frequency noise, then the term Δ_+ becomes a random variable which could be nonzero, and we need to find out its distribution. Assume that the frequency drift of each laser can be written as ξ_1 and ξ_2 , where $\xi_1 = \Delta'_1 - \Delta_1$, and $\xi_2 = \Delta'_2 - \Delta_2$.

We can now set up a model where ξ_i is measured by Ω_0 :

$$\xi_i = x_i\Omega_0, i = 1, 2 \quad (3.147)$$

Then similarly, we can assume that x_i has normal distribution with 0 mean and variance σ_i^2 :

$$f(x_i) = \frac{1}{\sqrt{2\pi}\sigma_i} e^{\frac{x_i^2}{2\sigma_i^2}}, i = 1, 2 \quad (3.148)$$

When the system doesn't have frequency noise, the term Δ_+ can be written as:

$$\Delta_+ = \Delta_1 + \Delta_2 + \frac{|\Omega_1|^2 - |\Omega_2|^2}{2(\Delta_1 - \Delta_2)} \quad (3.149)$$

Then with frequency noise, it becomes:

$$\Delta'_+ = \Delta_1 + \Delta_2 + \tilde{\Omega}_0(x_1 + x_2) + \frac{|\Omega_1|^2 - |\Omega_2|^2}{2(\Delta_1 - \Delta_2) + 2\tilde{\Omega}_0(x_1 - x_2)} \quad (3.150)$$

Our purpose here is to study the distribution of the variable x_+ , where it is defined as:

$$x_+ = \frac{\Delta'_+ - \Delta_+}{\tilde{\Omega}_0} \quad (3.151)$$

Then we can use the results in our single photon quasi-static frequency noise model, by replacing the term x in the single photon model by the term x_+ . Here x_+ seems to represent the "equivalent" frequency drift for the two-photon system.

Combining the results, we get:

$$\begin{aligned} x_+ = & x_1 + x_2 + \frac{1}{\tilde{\Omega}_0} \left[\frac{|\Omega_1|^2 - |\Omega_2|^2}{2(\Delta_1 - \Delta_2) + 2\tilde{\Omega}_0(x_1 - x_2)} - \right. \\ & \left. \frac{|\Omega_1|^2 - |\Omega_2|^2}{2(\Delta_1 - \Delta_2)} \right] \end{aligned} \quad (3.152)$$

The third term in the equation above has an general inverse-Gaussian distribution, which is also called Wald distribution, due to the $x_1 - x_2$ term on the denominator. Which is complicated and needs to be studied later.

Nonetheless, we can make an assumption that ξ_1 and ξ_2 are both much less than δ . Then equation above can be approximated to:

$$\begin{aligned} 3rdterm = & \frac{1}{\tilde{\Omega}_0} \left[\frac{|\Omega_1|^2 - |\Omega_2|^2}{2(\Delta_1 - \Delta_2) + 2\tilde{\Omega}_0(x_1 - x_2)} - \right. \\ & \left. \frac{|\Omega_1|^2 - |\Omega_2|^2}{2(\Delta_1 - \Delta_2)} \right] \\ = & \frac{1}{\tilde{\Omega}_0} \left[\frac{|\Omega_1|^2 - |\Omega_2|^2}{2(\Delta_1 - \Delta_2)} \left(1 - \frac{\tilde{\Omega}_0}{\delta}(x_1 - x_2) \right) - \right. \\ & \left. \frac{|\Omega_1|^2 - |\Omega_2|^2}{2(\Delta_1 - \Delta_2)} \right] \\ = & \frac{|\Omega_1|^2 - |\Omega_2|^2}{2\delta^2} (x_1 - x_2) \end{aligned} \quad (3.153)$$

This gives:

$$\begin{aligned} x_+ = & x_1 + x_2 + \frac{|\Omega_1|^2 - |\Omega_2|^2}{2\delta^2} (x_1 - x_2) \\ = & x_1 + x_2 + \alpha(x_1 - x_2) \end{aligned} \quad (3.154)$$

where $\alpha = \frac{|\Omega_1|^2 - |\Omega_2|^2}{2\delta^2}$.

We already know that x_1 and x_2 satisfies normal distribution, then using the properties of normal distributions, we get that x_+ also has normal distribution with zero mean, and a variance of:

$$\sigma_+^2 = (1 + \alpha)^2 \sigma_1^2 + (1 - \alpha)^2 \sigma_2^2 \quad (3.155)$$

Then we can transplant x_+ and σ_+ into the model that we developed for single photon.

$$\mathbb{E}[P] = \frac{1}{\sqrt{2\pi}\sigma_+} \int_{-\infty}^{\infty} \frac{1}{1+x_+^2} \sin^2(N\pi\sqrt{1+x_+^2}) e^{-\frac{x_+^2}{2\sigma_+^2}} dx \quad (3.156)$$

By Taylor expanding the \sin^2 term, we can get an approximation for the integral

$$\begin{cases} \mathbb{E}[P_g] = \sigma_+^2 + \frac{3N^2\pi^2\sigma_+^4}{4}, & N=0.5, 1.5, 2.5, 3.5, \dots \\ \mathbb{E}[P_e] = \frac{3N^2\pi^2\sigma_+^4}{4}, & N=1, 2, 3, 4, \dots \end{cases} \quad (3.157)$$

where $\sigma_+^2 = (1 + \alpha)^2 \sigma_1^2 + (1 - \alpha)^2 \sigma_2^2$, α is a constant, $\alpha = \frac{|\Omega_1|^2 - |\Omega_2|^2}{2\delta^2}$.

3.7 Intensity Noise

Time dependent intensity fluctuations are written as

$$I(t) = I_0 + \delta I(t) = I_0[1 + \alpha_I(t)] \quad (3.158)$$

where I_0 is the intensity of the noise-free laser and $\alpha_I(t)$ is the time-varying relative intensity fluctuation. The time varying Rabi frequency due to intensity noise for a one-photon process is

$$\Omega(t) = \Omega_0 \sqrt{1 + \alpha_I(t)} \quad (3.159)$$

where Ω_0 is the constant Rabi frequency.

The relative intensity noise (RIN) is the root-mean-square(RMS) value of the relative intensity fluctuations. In the following we will assume that $\alpha_I(t)$ is wide-sense stationary,

so that the RIN level is independent of time. The RIN level can be written in terms of the power spectrum of relative intensity noise as

$$\text{RIN} = \sqrt{\int_{-\infty}^{\infty} d\nu S_I(\nu)} \quad (3.160)$$

where

$$S_I(\nu) = \int_{-\infty}^{\infty} d\tau R_I(\tau) e^{-i2\pi\nu\tau} \quad (3.161)$$

and $R_I(\tau)$ is the intensity auto-correlation function as defined in Eq. ()�.

In principle the effect of intensity noise on gate fidelity can be calculated using methods similar to those used in previous sections for laser phase noise. In certain types of lasers, including semiconductor diode lasers, relaxation oscillations may lead to intensity noise at frequencies of several GHz]. In optically pumped solid-state lasers relaxation oscillations tend to be limited to much lower, sub MHz frequencies. The analysis here is limited to the case of intensity noise spectra that are substantially less than the Rabi frequency, which enables us to use a simplified quasi-static description of the noise.

We could also use the quasi-static theory to evaluate the effect of near-DC intensity noise components. We will compare these two methods of studying intensity noise in Sec. 3.8.3 and Sec. 3.8.3.

Assume that x follows normal distribution with zero mean and variance σ^2 :

$$f(x) = \frac{1}{\sqrt{2\pi}\sigma} e^{-\frac{x^2}{2\sigma^2}} \quad (3.162)$$

Here σ is the root-mean-square(RMS) intensity noise, which is the RIN level that we measure in labs.

Under this situation, the Rabi frequency for a two level system is then:

$$\Omega = \Omega_0 \sqrt{1+x} \quad (3.163)$$

where Ω_0 is the Rabi frequency when the intensity noise does not exist. Here to make the

expression valid we need $-1 \leq x \leq 1$, which means the intensity noise is not greater than the signal.

Under the setting that $-1 \leq x \leq 1$, we need to modify the distribution of x to be a truncated-Gaussian:

$$f(x) = \begin{cases} \frac{1}{\sqrt{2\pi}\sigma \text{Erf}(\frac{1}{\sqrt{2}\sigma})} e^{-\frac{x^2}{2\sigma^2}}, & \text{if } -1 \leq x \leq 1 \\ 0, & \text{otherwise} \end{cases}$$

In resonant Rabi oscillation the population probability for the ground state $|g\rangle$ is:

$$P_g = \cos^2\left(\frac{\Omega t}{2}\right) \quad (3.164)$$

Suppose we are interested on the expectation value of P_e after N cycles driven by a laser with intensity noise, $t_N = N \frac{2\pi}{\Omega_0}$. Then the expected value of P_e can be calculated by the following integral:

$$\mathbb{E}[P_g] = \frac{1}{\sqrt{2\pi}\sigma \text{Erf}(\frac{1}{\sqrt{2}\sigma})} \int_{-1}^1 \cos^2\left(\frac{\Omega t_N}{2}\right) e^{-\frac{x^2}{2\sigma^2}} dx \quad (3.165)$$

$$= \frac{1}{\sqrt{2\pi}\sigma \text{Erf}(\frac{1}{\sqrt{2}\sigma})} \int_{-1}^1 \cos^2(N\pi\sqrt{1+x}) e^{-\frac{x^2}{2\sigma^2}} dx \quad (3.166)$$

By assuming that x is very small, and doing Taylor expansion on the cosine part of the integral, we get the following approximation to second order:

$$\cos^2(N\pi\sqrt{1+x}) \approx 1 - \frac{N^2\pi^2x^2}{4} \quad (3.167)$$

By plugging the approximation back and doing Gaussian integral on x between -1 and 1, we get:

$$\mathbb{E}[P_g] = 1 - \frac{N^2\pi^2\sigma^2}{4} + \frac{N^2\pi^{\frac{3}{2}}}{2\sqrt{2}} \frac{\sigma e^{-\frac{1}{2\sigma^2}}}{\text{Erf}(\frac{1}{\sqrt{2}\sigma})} \quad (3.168)$$

The last term, with a $e^{-\frac{1}{2\sigma^2}}$ term, is zero in many orders of expansion. A good

approximation will then be:

$$\mathbb{E}[P_g] = 1 - \frac{N^2\pi^2\sigma^2}{4} \quad (3.169)$$

To conclude, we can write the error predicted by quasi-static model to be:

$$Error = \frac{N^2\pi^2\sigma^2}{4} \quad (3.170)$$

For a certain RIN level σ , to make the oscillation amplitude decay by a factor of $1/e$, we need the time $N_{1/e}$ (in oscillation cycles) to be;

$$N_{1/e} = \frac{1.59}{\pi\sigma} \quad (3.171)$$

For two-photon Rabi oscillations ,When $\delta = \Delta_1 - \Delta_2 \gg |\Omega_1|, |\Omega_2|$, solving the Schrodinger equations gives the following approximate expression for the population on the Rydberg state $|r\rangle$, assuming initially $|c_g(0)|^2 = 1, |c_e(0)|^2 = |c_r(0)|^2 = 0$:

$$|c_r(t)|^2 = \sin^2\left(\frac{\Omega_0 t}{2}\right) \quad (3.172)$$

Here $v = \Omega_1\Omega_2/\delta$. This expression is also only true when $\Delta_+ = \Delta_1 + \Delta_2 + \frac{|\Omega_1|^2 - |\Omega_2|^2}{2\delta} = 0$ is satisfied. This condition guarantees a full population transfer between the ground state $|g\rangle$ and the Rydberg state $|r\rangle$.

When $\Delta_+ \neq 0$, expression (3.172) becomes:

$$|c_r(t)|^2 = \frac{\Omega_0^2}{\Omega'^2} \sin^2\left(\frac{\Omega' t}{2}\right) \quad (3.173)$$

where $\Omega'^2 = \tilde{\Omega}_0^2 + |\Delta_+|^2$.

In our following discussions, we always assume that our noiseless system has $\Delta_+ = 0$.

If the two lasers driving the two-photon Rabi oscillations both have intensity noise:

$$\begin{aligned} I_1(t) &= I_{10} + \delta I_1(t) = I_{10}(1 + x_1(t)) \\ I_2(t) &= I_{20} + \delta I_2(t) = I_{20}(1 + x_2(t)) \end{aligned} \quad (3.174)$$

Assume that x_1 and x_2 both has normal distribution with 0 mean and variance σ_1^2 and σ_2^2 :

$$f(x_i) = \frac{1}{\sqrt{2\pi}\sigma_i} e^{\frac{x_i^2}{2\sigma_i^2}} \quad (3.175)$$

where $i = 1, 2$.

Under this model, the modified Rabi rate Ω'_i will be:

$$\Omega'_i = \Omega_i \sqrt{1 + x_i}, i = 1, 2 \quad (3.176)$$

Set $t_N = N \frac{2\pi}{\Omega_0}$, then the expected value of Rydberg state population can be calculated with the following integral, under the condition that $\Delta_+ = 0$:

$$\begin{aligned} \mathbb{E}[P_r] &= \frac{1}{2\pi\sigma_1\sigma_2} \int_{-\infty}^{\infty} dx_1 \\ &\quad \int_{-\infty}^{\infty} \sin^2(N\pi\sqrt{(1+x_1)(1+x_2)}) e^{\frac{x_1^2}{2\sigma_1^2}} e^{\frac{x_2^2}{2\sigma_2^2}} dx_2 \end{aligned} \quad (3.177)$$

Expanding the sin term in the integral to second order and evaluating the integral gives

an estimate for the expectation of the state occupancnt occupancy, which is also the expected population error in Rabi oscillations

$$\mathbb{E}[P_r] = \frac{N^2\pi^2\sigma_1^2}{4} + \frac{N^2\pi^2\sigma_2^2}{4}. \quad (3.178)$$

3.8 Numerical Simulations of the Laser Noise

3.8.1 Dynamical Equations

Two start with, we study a two-level system interacting with a monochromatic field. By writing the state of the system to be $|\psi\rangle = c_g(t)e^{-i\omega_g t}|g\rangle + c_e(t)e^{-i\omega_e t}|e\rangle$, and the electric field to be $E = (\varepsilon/2)e^{-i\omega t} + c.c.$, we can solve the Schrödinger equations directly and get

the following dynamical equations:

$$\frac{d}{dt}c_g(t) = i\frac{\Omega_0}{2}e^{-i\Delta t}c_e(t) \quad (3.179)$$

$$\frac{d}{dt}c_e(t) = i\frac{\Omega_0^*}{2}e^{i\Delta t}c_g(t) \quad (3.180)$$

where Δ is the detuning $\Delta = \omega - \omega_{eg} = \omega - (\omega_e - \omega_g)$, and Ω_0 is the complex Rabi frequency $\Omega_0 = d_{eg}\epsilon/\hbar$, where d_{eg} is the atomic dipole moment.

For simplicity, we first assume that there are no detunings so that $\Delta = 0$. Then we can study how phase and intensity noise can affect the above dynamical equations. A time varying phase noise $\phi(t)$ gives an extra phase term $e^{i\phi(t)}$ to the right side of equation 3.179 and 3.180. For intensity noise, we use the following form:

$$I(t) = I_0 + \delta I(t) == I_0(1 + \alpha_I(t)) \quad (3.181)$$

where I_0 is the intensity of the noise-free laser. We use $\alpha_I(t)$ to represent the time-varying relative intensity fluctuation. With these two types of time-varying noise, the dynamical equations become:

$$\frac{d}{dt}c_g(t) = i\frac{\Omega_0\sqrt{1 + \alpha_I(t)}}{2}e^{i\phi(t)}c_e(t) \quad (3.182)$$

$$\frac{d}{dt}c_e(t) = i\frac{\Omega_0^*\sqrt{1 + \alpha_I(t)}}{2}e^{-i\phi(t)}c_g(t) \quad (3.183)$$

For a two-photon Rabi oscillation between 3 atomic levels, the dynamical equations can be written as the following:

$$\frac{d}{dt}c_g(t) = i\frac{\Omega_1^*}{2}e^{i\Delta_1 t}c_e(t) \quad (3.184)$$

$$\frac{d}{dt}c_e(t) = i\frac{\Omega_1}{2}e^{-i\Delta_1 t}c_g(t) + i\frac{\Omega_2^*}{2}e^{i\Delta_2 t}c_r(t) \quad (3.185)$$

$$\frac{d}{dt}c_r(t) = i\frac{\Omega_2}{2}e^{-i\Delta_2 t}c_e(t) \quad (3.186)$$

Here Ω_1 , Ω_2 , Δ_1 , Δ_2 are the Rabi frequencies and detunings of the two transitions, respectively. If we add phase noise $\phi_1(t)$ and $\phi_2(t)$ to both lasers, the dynamical equations become:

$$\frac{d}{dt}c_g(t) = i\frac{\Omega_1^*}{2}e^{i(\Delta_1 t + \phi_1(t))}c_e(t) \quad (3.187)$$

$$\frac{d}{dt}c_e(t) = i\frac{\Omega_1}{2}e^{-i(\Delta_1 t + \phi_1(t))}c_g(t) + i\frac{\Omega_2^*}{2}e^{i(\Delta_2 t + \phi_2(t))}c_r(t) \quad (3.188)$$

$$\frac{d}{dt}c_r(t) = i\frac{\Omega_2}{2}e^{-i(\Delta_2 t + \phi_2(t))}c_e(t) \quad (3.189)$$

For the two-photon transitions, we are mostly interested in the case where $\delta = \Delta_1 - \Delta_2 \gg |\Omega_1|, |\Omega_2|$. In this case the intermediate state $|e\rangle$ is mostly not populated, and the response of the system is an effective 1-photon Rabi transition between $|g\rangle$ and $|r\rangle$, with effective 2-level Rabi frequency $\Omega_R = \frac{\Omega_1\Omega_2}{\delta}$.

3.8.2 Testing Density Matrix Solutions

In this section, we present numerical results that simulates the response of a system with frequency noise with a 3-step recipe: First, we define the noise spectrum of a laser. This can be done by either directly giving the expression the noise spectrum; or calculate the noise spectrum from lab self-heterodyne measurements, as we have already introduced in Sec. 3.4.1 and 3.4.2; Second, create samples of the time-varying phase noise and $\phi(t)$ from the noise spectrum; And last, we can plug $\phi(t)$ into the dynamical equations in Sec. 3.8.1 and simulate the result with computer programs. As $\phi(t)$ we generate is only one random sample of the the result, we will repeat this last step for many times and examine the statistical properties of the simulation outcomes.

To generate a frequency noise spectrum, we start with the self-heterodyne measurement on one of the lasers in our laser. The original measurement result is shown as follow:

From this measurement we are able to generate a noise spectrum with servo bumps, which will give us exactly the same self-heterodyne result. The expression we generated is:

$$S_{\delta\nu}(f) = h_g \exp\left(-\frac{(f - f_g)^2}{2\sigma_g^2}\right) \quad (3.190)$$

where $h_g = 1100 \text{ Hz}^2/\text{Hz}$, $f_g = 234 \text{ kHz}$, $\sigma_g = 1.4 \text{ kHz}$. Here h_g , f_g and σ_g are the amplitude, center frequency and width of the servo bump. The fractional power inside the servo bump (relative to the main peak in the self-heterodyne spectrum) is given by $\Delta P = \frac{\sqrt{2\pi}h_g\sigma_g}{f_g^2}$. The self-heterodyne measurement and the self-heterodyne spectrum derived from the noise spectrum above are shown in Fig. 3.3.

One-photon transitions

First, we study the effect of frequency noise on one-photon Rabi transitions, where its dynamical equations are given in equation (3.179) and (3.180).

For a laser with white noise, we start with $h_0 = 200 \text{ Hz}$ and bandwidth $bw = 10\Omega_0$, $\Omega_0 = 1\pi \text{ MHz}$, and then change h_0 to simulate the response of the system. We also compare the numerical results with equation (3.112). The results are shown in Fig. 3.6. For a laser with servo bumps, we are first interested in the effect of the fractional power

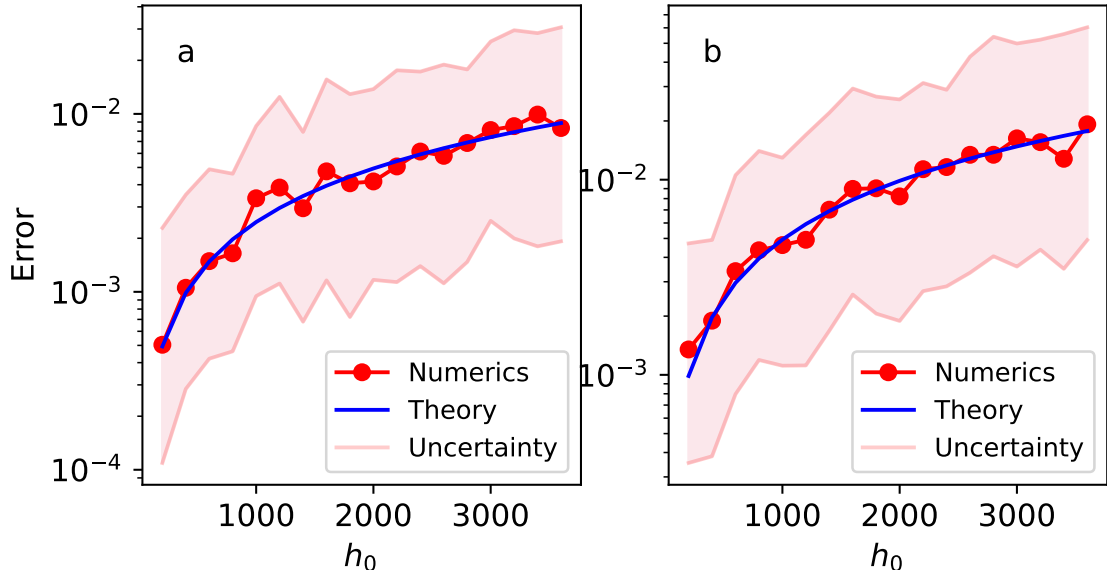


Figure 3.6: (a: π pulse; b: 2π pulse) Relation between rabi population errors and the amplitude h_0 of the white noise spectrum. Bandwidth of the spectrum in the simulation is $bw = 10\Omega_0$, $\Omega_0 = 1\pi \text{ MHz}$.

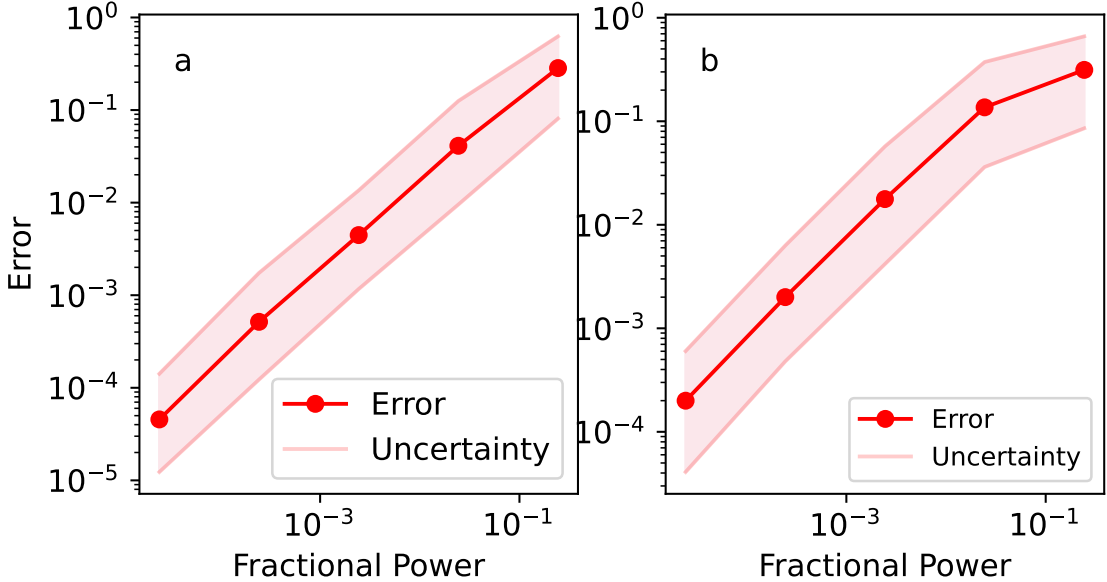


Figure 3.7: (a: π pulse; b: 2π pulse) Relation between rabi population errors and the fractional power of the servo bump. $h_g = 1100 \text{ Hz}^2/\text{Hz}$, $\sigma_g = 1.4 \text{ kHz}$, f_g is the bump center frequency where maximum error is generated.

inside the bump, which is given by $\Delta P = \frac{\sqrt{2\pi}h_g\sigma_g}{f_g^2}$. We start with the noise spectrum and parameters defined in equation(3.190), and then change h_g to simulate the effect of different ΔP s, while keeping bump center frequency f_g unchanged. The results are shown in Fig.3.7. Besides bump power, it would also be important to study how different servo bump center frequencies would affect the Rabi errors. To do this we still start with the noise spectrum and parameters defined in equation(3.190), then gradually increase the bump center frequency f_g and simulate the response of the system. Parameter h_g is changed accordingly to keep fractional power ΔP unchanged. We also compare the numerical results with equation(3.114). The results are shown in Fig.3.8.

From Fig.3.8 we can find that the servo bump would have the largest effect on Rabi population errors when $f_g \approx 1.5\Omega_0$ for π pulse, and $f_g \approx 1.0\Omega_0$ for 2π pulse.

Two-photon transitions

For two-photon transitions, we start with a simple assumption that $\Omega_1 = \Omega_2$, and that the two lasers have the identical noise spectrum. Two samples of the phase noise $\phi_1(t)$

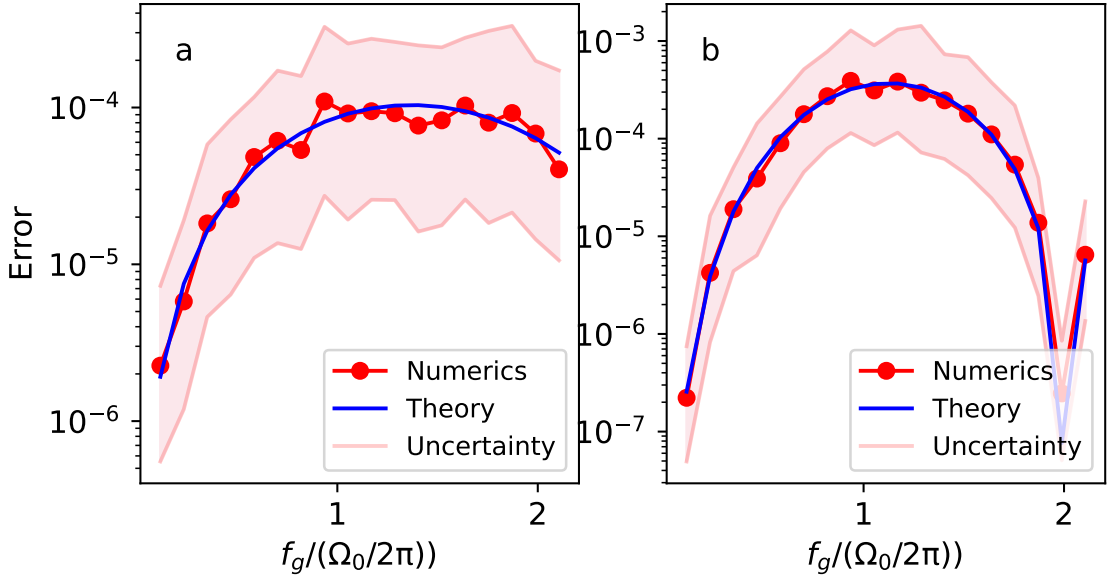


Figure 3.8: (a: π pulse; b: 2π pulse) Relation between Rabi population errors and the center frequency of the servo bump f_g . Here we assume that the two lasers have the same frequency noise power spectrum. $h_g = 1100 \text{ Hz}^2/\text{Hz}$, $\sigma_g = 1.4 \text{ kHz}$. Ω_0 is the Rabi frequency.

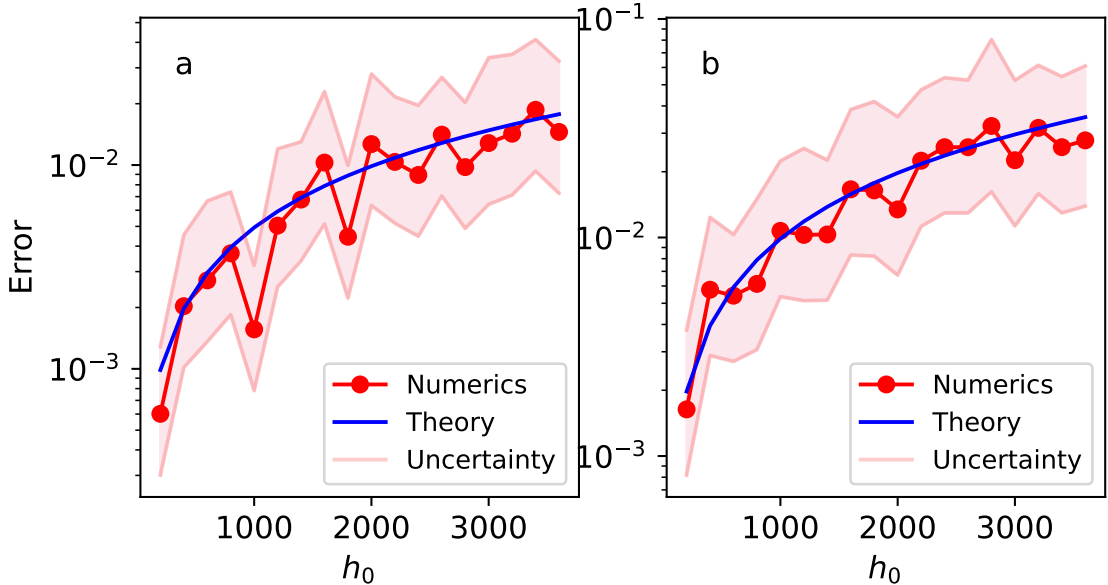


Figure 3.9: (a: π pulse; b: 2π pulse) Relation between rabi population errors and the amplitude h_0 of the white noise spectrum. Bandwidth of the spectrum in the simulation is $bw = 10\Omega_0$, $\Omega_0 = 1\pi \text{ MHz}$.

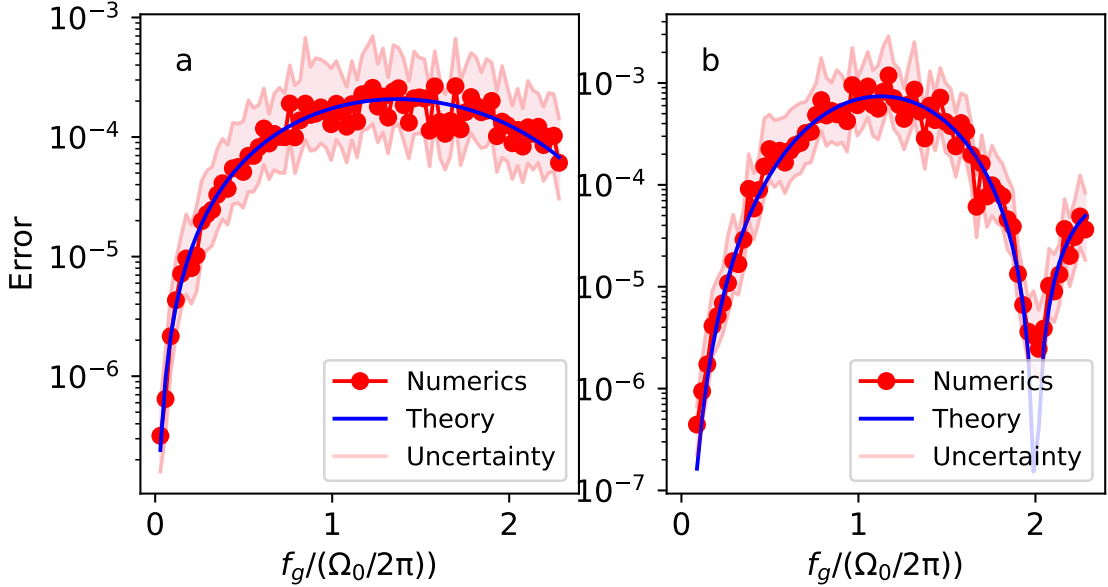


Figure 3.10: (a: π pulse; b: 2π pulse) Relation between rabi population errors and the center frequency of the servo bump f_g . $h_g = 1100 \text{ Hz}^2/\text{Hz}$, $\sigma_g = 1.4 \text{ kHz}$. Ω_0 is the Rabi frequency.

and $\phi_2(t)$ are generated from the spectrum and inserted into the dynamical equations.

We first study the effect of white noise in two-photon transitions. We use the same parameter settings in section 3.8.2 for the simulation. We also compare the numerical results with equation(3.127). The results are shown in Fig.3.9.

We start with the same spectrum and parameters defined in equation (3.190), and then study the effect of fractional power in the bump as well the effect of the center frequency of the bump, with approaches that we used in the section above. We also compare the numerical results with equation(3.128).

The results are shown Fig.3.10.

3.8.3 Testing Quasi-Static Model

In this section we are going to compare the results from the quasi-static model to the numerical results from the time-series simulations.

The noise we are simulating is a band-limit white frequency noise with a cut-off frequency F_c in its frequency domain. Before knowing the result, we assumed that the two

results should match, especially when the cut-off frequency F_c is low compared to the Rabi frequency Ω .

One-Photon Frequency Noise

Here we still use dynamical equations given in equation (3.182) and (3.183) for the numerical simulations. The initial noise spectrum being used here is a white-noise spectrum with height $h_0 = 0.01F_c$, and cut-off frequency $F_c = 0.01\Omega_0$, where Ω_0 is the Rabi frequency. We then increase the linewidth l of the corresponding lineshape by increasing h_0 , as $l = \pi h_0$. The results are shown in Fig.3.11.

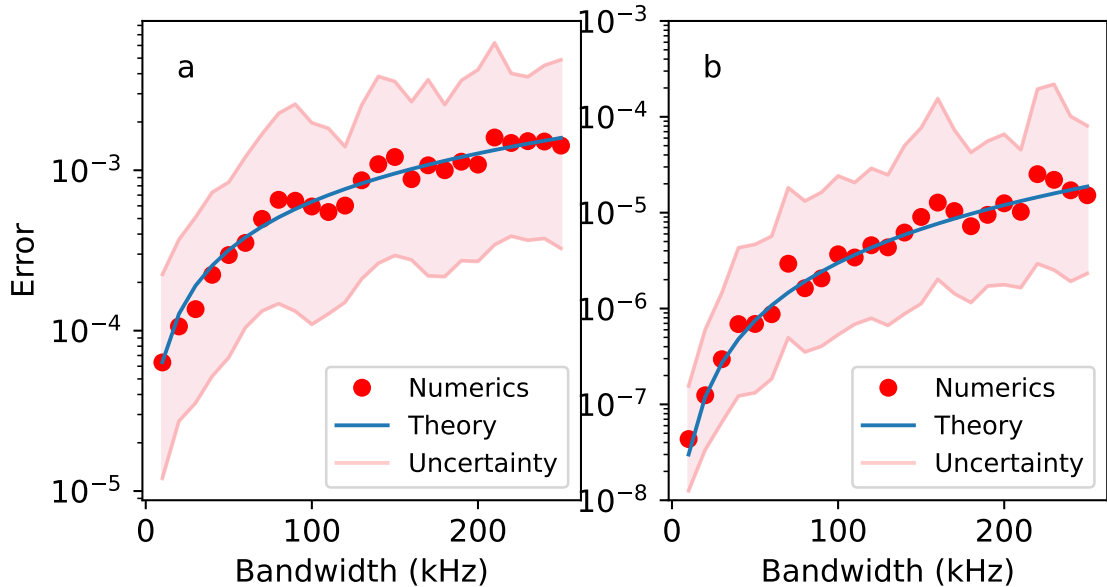


Figure 3.11: (a: π pulse; b: 2π pulse) Errors predicted by Equation (3.146) in the quasi-static model and errors calculated by numerical simulations. $\Omega_0 = 1 \times 2\pi$ MHz.

By setting the linewidth to $lw = 0.05\Omega_0$ and sweeping F_c , the results are shown in Fig.3.12. Showing the quasi-static theory start to diverge from the numerics when the bandwidth gets larger.

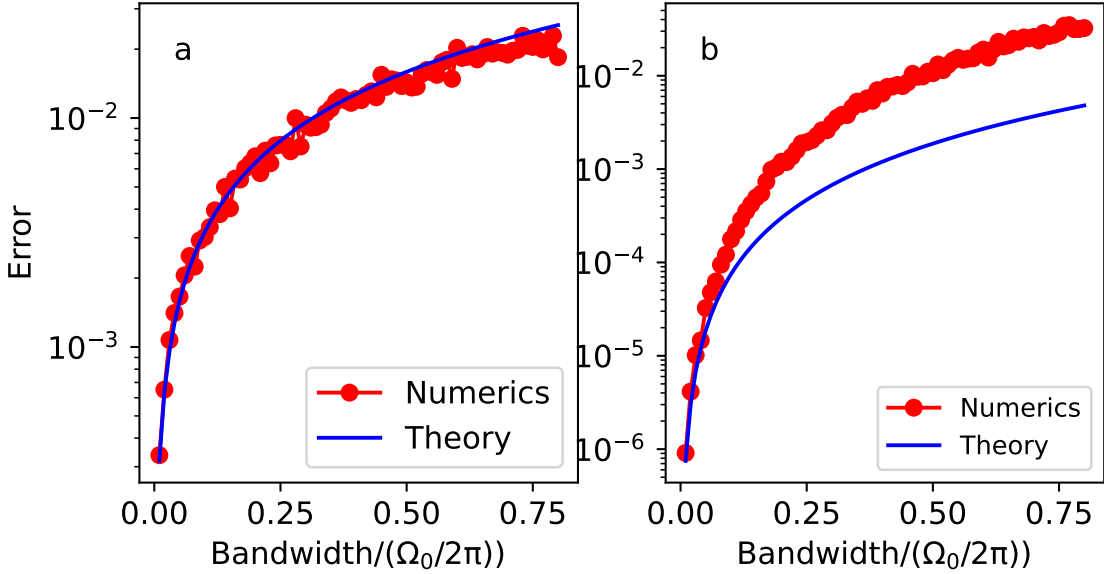


Figure 3.12: (a: π pulse; b: 2π pulse) Relation between errors and the bandwidth of the frequency noise spectrum. $\Omega_0 = 1 \times 2\pi$ MHz.

One-Photon Intensity noise

Here we numerically simulate dynamical equations given in (3.182) and (3.183). We assume that the time-varying intensity noise has a constant-amplitude power spectral density and a certain bandwidth. Each amplitude correspond to a different RIN level. We sweep the RIN level of the intensity noise in our numerical simulations. We also compare the numerical results with equation(3.170). The results are shown in Fig.3.13.

Two-Photon Frequency noise

For two-photon transitions we assume the two lasers have exactly the same noise spectrum, and two samples of phase noise $\phi_1(t)$ and $\phi_2(t)$ are generated and used in evaluating the 2-photon dynamical equations. In this case we assume that the two lasers have the same spectrum as it was in the one-photon transition, which is a white-noise spectrum with height $h_0 = 0.01F_c$, and cut-off frequency $F_c = 0.01\tilde{\Omega}_0$. Given this, the quasi-static

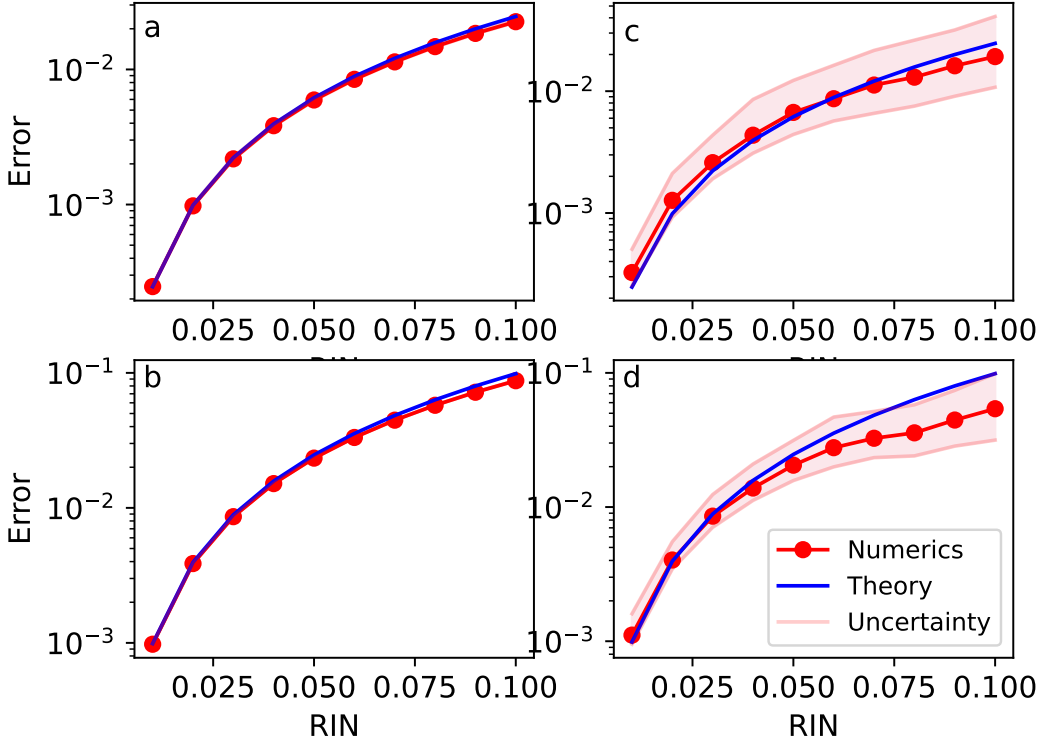


Figure 3.13: (a,c: π pulse; b,d: 2π pulse; a,b: $F_c = 0.1\Omega_0$; c,d: $F_c = 10\Omega_0$) Relation between errors and the RIN level of the intensity noise. F_c is the bandwidth of the intensity noise spectrum. $\Omega_0 = 1 \times 2\pi$ MHz.

estimate for errors (Equation (3.157)) now becomes:

$$\begin{cases} \mathbb{E}[P_g] = \sigma^2 + 12N^2\pi^2\sigma^4, & N=0.5, 1.5, 2.5, 3.5, \dots \\ \mathbb{E}[P_e] = 12N^2\pi^2\sigma^4, & N=1, 2, 3, 4, \dots \end{cases} \quad (3.191)$$

where $\sigma = \sigma_1 = \sigma_2$.

Here we increase the linewidth l of the corresponding lineshape by increasing h_0 . The results are shown in Fig.3.14.

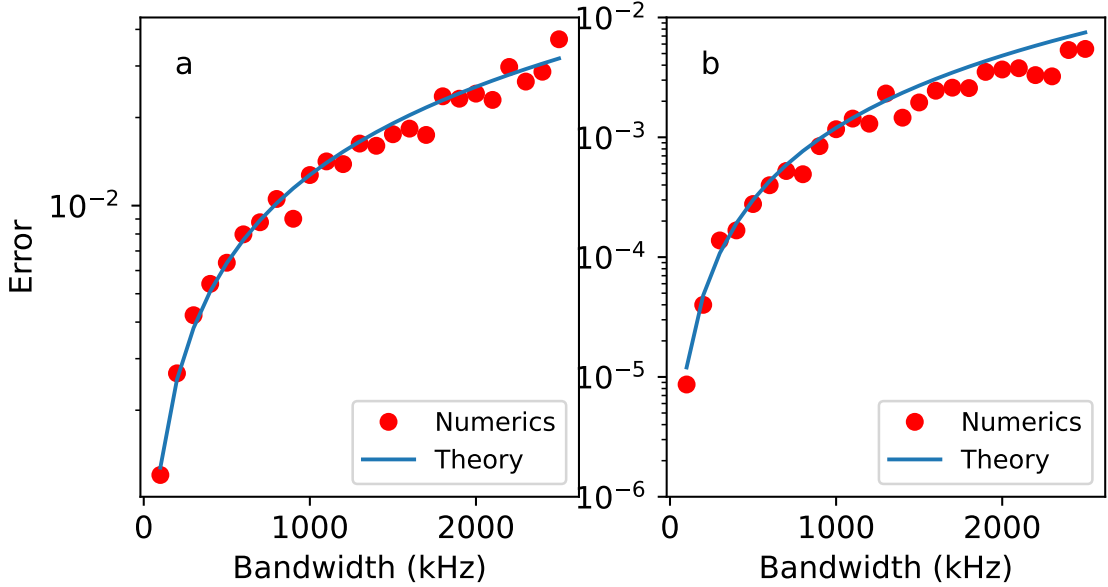


Figure 3.14: (a: π pulse; b: 2π pulse) Relation between errors and the linewidth of the laser. Here we assume that the two lasers have the same linewidth in their Lorentzian lineshape. $\tilde{\Omega}_0 = 1 \times 2\pi$ MHz.

Two-Photon Intensity Noise

Similar to section 3.8.3, we assume the two lasers have the same RIN level, and we compare the numerical results with Equation (3.178): Fig.3.15.

3.8.4 Effect of Laser noise on Ramsey Measurements

Assume that we perform a standard Ramsey measurement(a $\frac{\pi}{2}$ -gap- $\frac{\pi}{2}$ operation) on a two-level system $|g\rangle$ and $|e\rangle$.Here we assume that the laser field is very close to resonant with the system($\omega_q \approx \omega$), but carries some frequency/phase noise. For simplicity we only consider the effect of the laser noise during the gap time.

After the $\frac{\pi}{2}$ -gap- $\frac{\pi}{2}$ operation, the probability of finding the qubit in state $|g\rangle$ is:

$$P_g = \frac{1 - \cos(\Delta T + \phi_{\omega n}(T))}{2} \quad (3.192)$$

, where T is the length of the gap, Δ is the detuning of the laser, and $\phi_{\omega n}(T)$ is the phase accumulated on the laser during the gap time T. If we vary the term ΔT and measure P_g ,

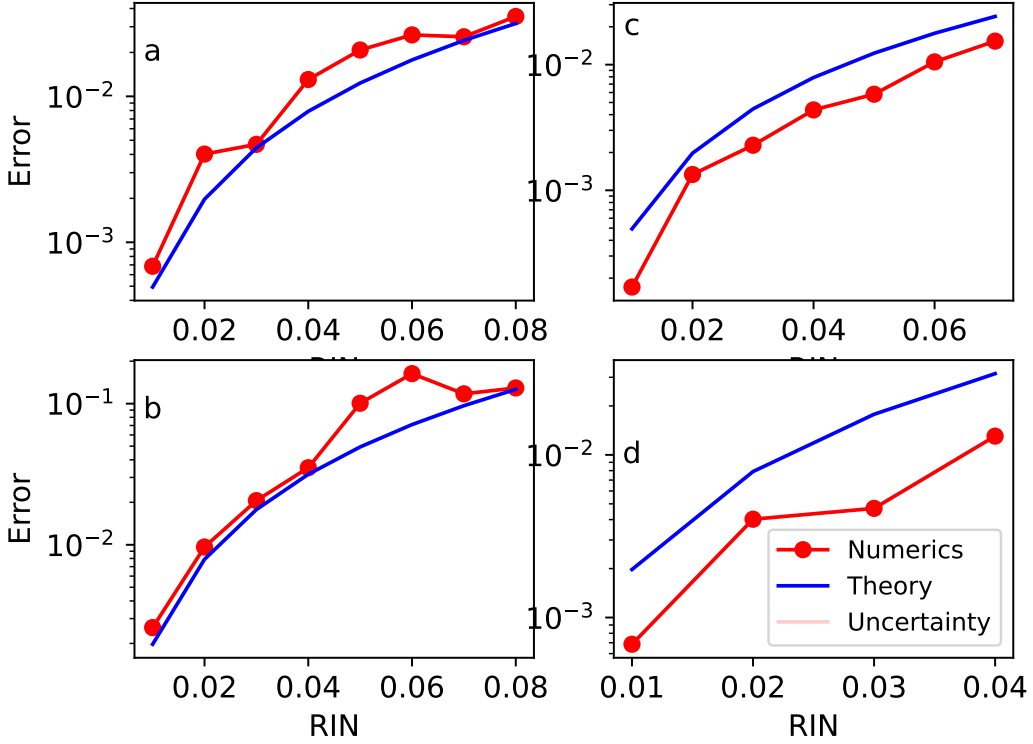


Figure 3.15: (a,c: π pulse; b,d: 2π pulse; a,b: $F_c = 0.1\tilde{\Omega}_0$; c,d: $F_c = 10\Omega_0$) Relation between errors and the RIN level of the intensity noise. F_c is the bandwidth of the intensity noise spectrum. $\tilde{\Omega}_0 = 1 \times 2\pi$ MHz.

we would get a fringe. The peak-to-peak amplitude of the fringe(by setting $\Delta T = 2n\pi$ is:

$$a = \cos(\phi_{\omega n}(T)) \quad (3.193)$$

One-photon transition

A laser's phase noise can be identified as a Wiener process when its corresponding frequency noise has a white power spectrum, since the phase drift is the accumulation of instantaneous frequency noise:

$$\frac{\phi(t)}{2\pi} = \int_0^t \Delta\nu(t)dt \quad (3.194)$$

The Wiener process is a process that $W_0 = \frac{dW(t)}{dt}$ is a process with flat power spectral

density:

$$S_0 = h_0 \quad (3.195)$$

From the property of the Wiener process we can infer that the noise term $\phi_{\omega n}(T)$ in Ramsey experiments has the following property:

$$\phi_{\omega n}(T) \sim \mathcal{N}(0, 4h_0\pi^2 T) \quad (3.196)$$

The expected value of the peak-to-peak amplitude of the fringe is:

$$\begin{aligned} \mathbb{E}[a] &= \int_{-\infty}^{\infty} \cos(x) \frac{1}{\sqrt{8h_0\pi^3 T}} e^{-\frac{x^2}{8h_0\pi^2 T}} dx \\ &= e^{-2h_0\pi^2 T} \end{aligned} \quad (3.197)$$

The T_2 time is therefore:

$$T_2 = \frac{1}{2h_0\pi^2} \quad (3.198)$$

Fig.3.16 shows the comparison between T_2 time predicted by equation (3.198) and T_2 time from simulations.

Two-photon transition

In two-photon Ramsey experiments, with the limit of $\delta \gg |\Omega_1|, |\Omega_2|$, the equivalent Rabi frequency equals to $\tilde{\Omega}_0 = \Omega_1\Omega_2/2\Delta_1$.

The phase noise from Ω_0 is from the noise in Ω_1 and Ω_2 . So $\phi_R(t) = \phi_1(t) + \phi_2(t)$.

For the noise term $\phi_{\omega n}(T)$, it should equal to the sum of the random phases accumulated on each laser:

$$\phi_{\omega n}(T) = \phi_1(T) + \phi_2(T) \quad (3.199)$$

, where $\phi_1(T) \sim \mathcal{N}(0, h_1\pi^2 T)$, and $\phi_2(T) \sim \mathcal{N}(0, h_2\pi^2 T)$. h_1 and h_2 are the amplitudes of the white noise of each laser in their power spectral density.

Combining the above equations we have:

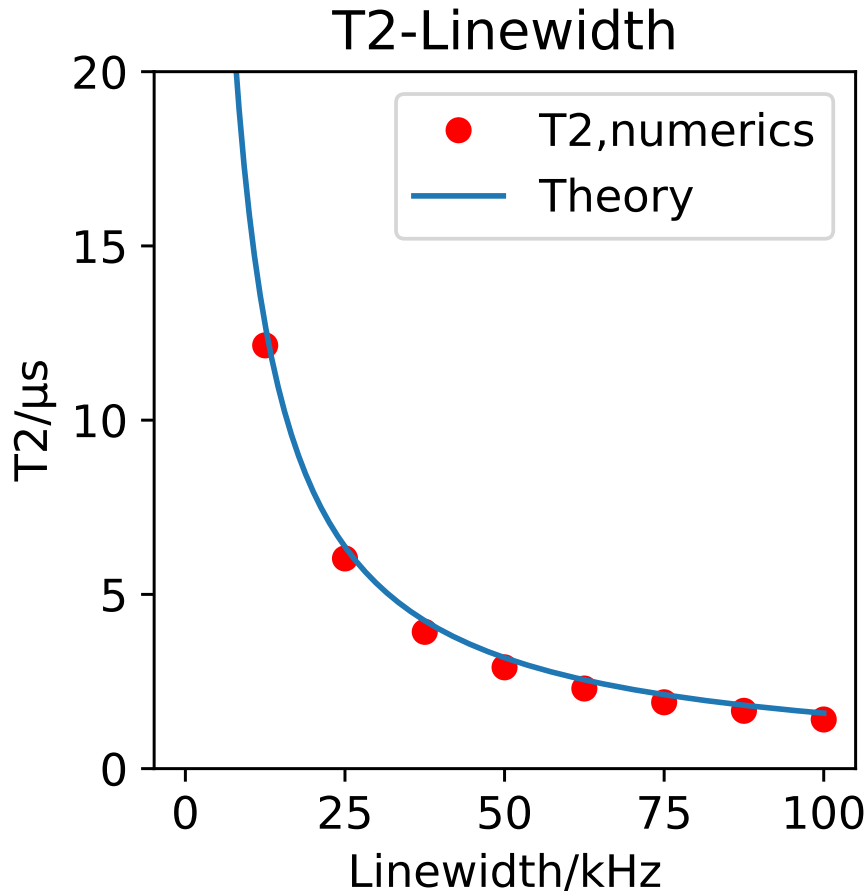


Figure 3.16: (One photon)Blue: T2 time predicted by theory; Red: T2 time simulated from dynamical equations.

$$\phi_{\omega n}(T) \sim \mathcal{N}(0, 4(h_1 + h_2)\pi^2 T) \quad (3.200)$$

Assuming that the carrier-domain lineshape of each laser is $FWHM_1$ and $FWHM_2$, then the expression for T_2 is then:

$$T_2 = \frac{1}{2(h_1 + h_2)\pi^2} \quad (3.201)$$

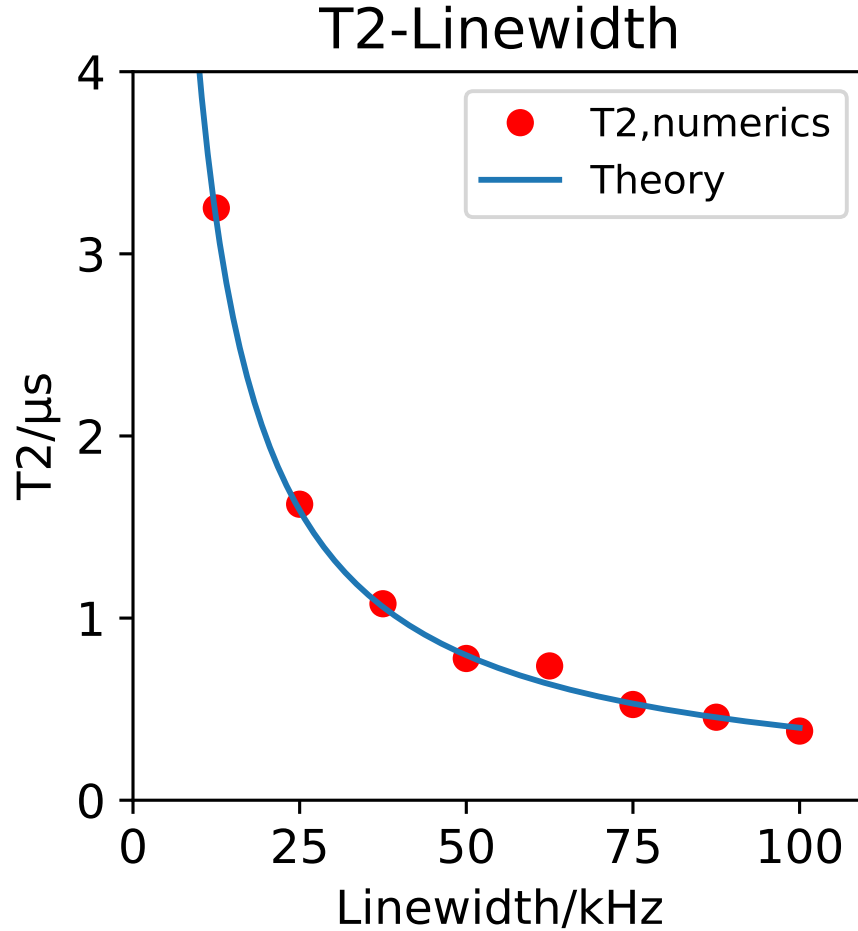


Figure 3.17: (Two photon)Blue: T2 time predicted by theory; Red: T2 time simulated from dynamical equations.

3.9 Outlooks for Future Research

In the above sections we presented a detailed analysis for the effect of laser noise in Rabi oscillations. To begin with, we studied how to translate the self-heterodyne spectrum $S_i(f)$ to the frequency noise power spectral density $S_{\delta\nu}(f)$. We mainly focused on relating white noise and servo bump noises in $S_{\delta\nu}(f)$ to measurements. In reality, however, a laser's noise spectrum could be more complicated, which could include pink($1/f$) noise or Brownian($1/f^2$) noise. We did not analyze these types of noises, but one can use some general expressions we presented, such as Eqs. (3.61) and (3.64), to analyze other types

of noises.

For a given noise, we mainly focused on evaluating the population errors for 1- and 2-photon Rabi oscillations. For phase errors, for simplicity we only analyzed white noise in section 3.8.4. A more complete study of phase errors for complicated noise spectrum, such as the servo bump noise, would be the next step for our theoretical study for laser noise.

Finally, since what we are presenting are all pure theoretical studies, our results will be more convincing if the expressions for Rabi errors can be verified through experiments. The experiment could be difficult to implement with optically driven Rabi oscillations, since the laser noise spectrum is affected by many error sources, thus making it difficult to sweep parameters and do tests against our theories such as Eqs. (3.114). However, since our analysis is determined solely by the power spectral densities of the frequency noise as a random process, and not involving any photonic nature of lasers, our theory could also be applied to microwave Rabi processes. In this case, we can sweep the parameters of the noise and "add" the noise to the microwave sources. For example, in our Cesium atom array experiment we use the $F = 3$ and $F = 4$ hyperfine levels as our qubit state $|0\rangle$ and $|1\rangle$. In experiments we use a microwave source that is resonance with the energy splitting of 9.192631770 GHz to drive the rotations between the two levels. Here we can inject noise with spectrum of certain parameters to the microwave source with devices such as the arbitrary waveform generator(AWG), and measure the Rabi errors in single-qubit oscillations. This experiment is listed on the plan for future experiments of our lab.

Chapter 4

Multi-Qubit Gate

Neutral atoms provide an ideal platform for implementing multi-qubit gates, thanks to the long-range nature of Rydberg interactions and the effect of Rydberg blockades. In this section we propose and analyze a high fidelity approach for implementing C_kZ gates and CZ_k gates. A C_kZ gate performs a Z rotation on the target qubit when all k controls are in state $|1\rangle$, and otherwise does not change the state of the target. The CZ_k gate imparts a π phase shift on the composite state when all $k+1$ qubits are in state $|1\rangle$ and otherwise has no effect. As the two-qubit case for both gates is the basic CZ gate, the C_kZ gate is symmetric with respect to permutation of any of the $(k+1)$ qubits, and the CZ_k gate is symmetric within all the k data qubits.

4.1 C_kZ gate protocol

A C_kZ gate involves $k+1$ qubits with a controlled Z operation performed on the target provided all $k+1$ qubits are in state $|1\rangle$. This can be expressed as

$$C_kZ = I - 2P_{|1\rangle^{\otimes(k+1)}} \quad (4.1)$$

where I is the identity operator and $P_{|1\rangle^{\otimes(k+1)}}$ is the projector onto the state $|1\rangle^{\otimes(k+1)}$.

The C_kZ gate can be realized in a system with symmetric interactions, where all the

$k+1$ atoms are within a blockade radius of each other. To implement the gate, 2π Rydberg pulses are applied to each atom, and the system is coupled to a collective, singly excited Rydberg state. After the pulse the collective state gains a π phase shift, except when the initial state of the system is $|00\dots0\rangle$, assuming that the Rydberg pulse couples state $|0\rangle$ to Rydberg state $|r\rangle$. Therefore the logical transformation matrix of the system is $\text{diag}[-1, -1, -1, \dots, 1]$, which is equivalent to a $C_k Z$ gate, up to an irrelevant global phase. Although the Rydberg blockade mechanism is an essential ingredient that enables this multi-qubit gate it also leads to a Rabi frequency and pulse area that scales as \sqrt{n} where n is the number of Rydberg coupled atoms. Since n is unknown the pulse area is not well defined, which leads to large gate errors if constant amplitude pulses are used. This problem can be circumvented by using adiabatic pulses which have a constant pulse area despite the underlying variation in Rabi frequency. This idea was introduced in[42] in the context of gate design for multi-atom ensemble qubits.

We consider two types of adiabatic pulses shown in Fig. 4.1: the double ARP pulse analyzed in [43] with Bell-state fidelity $\mathcal{F} > 0.997$ and the single Gaussian pulses analyzed in [44] with fidelity $\mathcal{F} > 0.996$. The ARP pulses consist of two identical π pulses with time-dependent Rabi drive $\Omega(t)$ and detuning $\Delta(t)$

$$\Omega(t) = \Omega_0 \frac{e^{-(t-t_0)^4/\tau^4} - a}{1 - a} \quad (4.2a)$$

$$\Delta(t) = -\Delta_0 \cos\left(\frac{2\pi}{T}t\right), \quad (4.2b)$$

with t_0 the center of each pulse and $T/2$ the length of each pulse so the gate duration is T . The parameter a is chosen so that $\Omega = 0$ at the beginning and end of each pulse. The pulse slope parameter was set to be $\tau = 0.175T$.

The single Gaussian pulse has a constant detuning $\Delta(t) = \Delta$ and a time-dependent Rabi Drive

$$\Omega(t) = \Omega_0 e^{-t^2/\delta t^2}. \quad (4.3)$$

The parameter δt was varied to optimize the gate fidelity as discussed below.

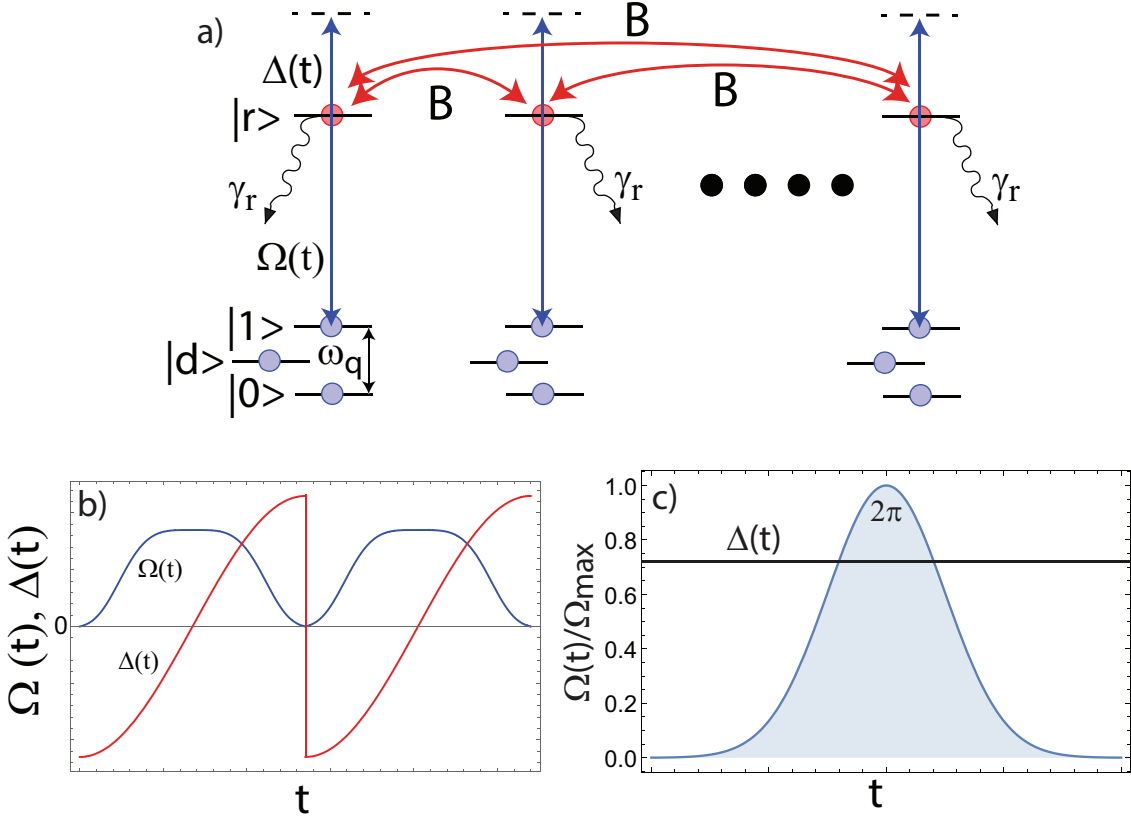


Figure 4.1: Multi-qubit gate protocols. a) Each atom is described with a 4-level structure: computational basis $|0\rangle$, $|1\rangle$, Rydberg state $|r\rangle$, and leakage state $|d\rangle$. In the fully symmetric case each pair of atoms has equal Rydberg coupling B . b) ARP pulses applied to each atom for the $C_k Z$ gate. c) Single Gaussian pulse at fixed detuning applied to each atom for the CZ_k gate.

Multi-qubit $C_k Z$ and CZ_k gates act in a Hilbert space of dimension $d = 2^{k+1}$. The process fidelity can be evaluated by random sampling of the gate action on input states in a d dimensional space. It is sufficient to sample a subset of $2d$ states in mutually unbiased bases[45]. We will instead use the method introduced in [46], which shows that the average fidelity based on a set of $d + 1$ input states provides a good estimate of gate fidelity. This set of states consists of $d = 2^{k+1}$ basis states $|\phi_j\rangle$, $j = 1, \dots, 2^k$ as well as a superposition state $|\phi_{\text{ave}}\rangle = (1/\sqrt{d}) \sum_{j=1}^d |\phi_j\rangle$. This estimate is also sufficient to quantify the nonunitarity of the gate.

The Rydberg pulses used to implement $C_k Z$ and CZ_k gates as described below result in unitary transformations that differ from the desired outcome up to phases that can be

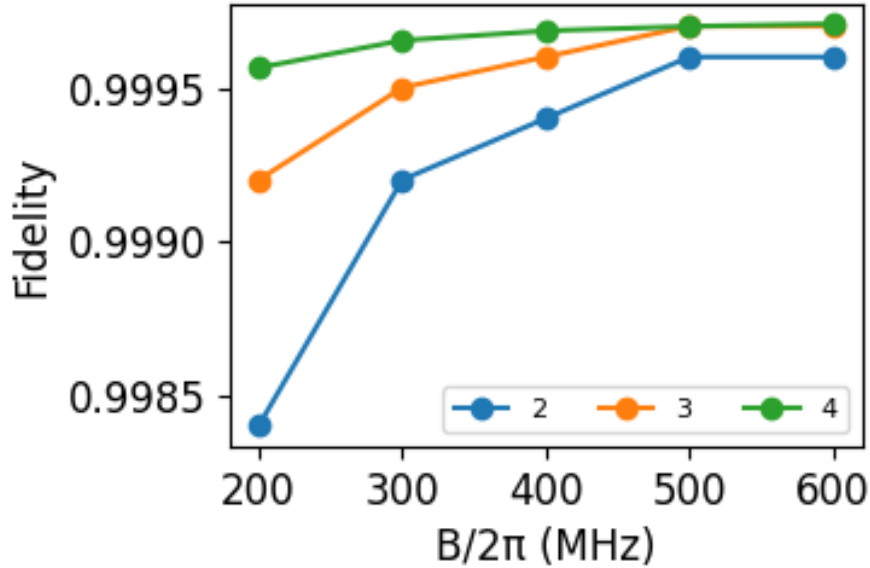


Figure 4.2: Numerical results for $C_k Z$ gate fidelities with different control qubit number k and coupling strength B . The gate is implemented with ARP pulses. $\Omega_0/2\pi = 17$ MHz, Rydberg lifetime $\tau = 540\mu s$, $T_{initial} = 0.54\mu s$, $\Delta_{initial}/2\pi = 23$ MHz.

corrected with single qubit R_Z rotations. These rotations are parameterized in terms of phases $[\chi_1, \chi_2, \dots, \chi_N]$. Gate optimization is performed by varying pulse parameters and for each set of parameters also varying the χ phases to optimize the fidelity.

In the following we will show that with the ARP pulses $C_k Z$ fidelity $\mathcal{F} > 0.991$ can be achieved for $k = 2, 3$ and 4 with equal Rydberg coupling strengths for each pair of qubits. We will also show the protocol's robustness against unequal coupling strengths. .

4.1.1 Numerical results for symmetric interactions

In this section we start with the simplest case of equal Rydberg coupling strength between all pairs of atoms. The fidelities of the $N = k + 1$ qubit gate $C_k Z$ for $k = 1, 2, 3, 4$ are presented in Table 4.1 for an interaction strength of $B/2\pi = 200$ MHz and in Fig. 4.2 for $B/2\pi$ from 200-600 MHz. Optimized values of the gate parameters that maximize the fidelity were found using the procedure described in Appendix A.2. The numerical results demonstrate that the protocol for implementing a multi-qubit $C_k Z$ gate with symmetric ARP pulses gives fidelities $\mathcal{F} > 0.998$. Interestingly \mathcal{F} increases as k gets larger.

Table 4.1: Fidelity of $C_k Z$ gates with ARP pulses for $k = 2, 3, 4$ with $B/2\pi = 200$ MHz, $\Omega_0/2\pi = 17$ MHz, Rydberg lifetime $\tau = 540\mu s$. $T_{\text{initial}} = 0.54 \mu s$, $\Delta_{\text{initial}}/2\pi = 23$ MHz.

k	Fidelity	$\Delta_0/(2\pi)$ (MHz)	$T (\mu s)$
2	0.9984	25.36	0.399
3	0.9992	27.12	0.431
4	0.9995	28.66	0.427

4.1.2 Numerical results for asymmetric interactions

In a real implementation the interaction strengths between atom pairs may not be all equal due to geometrical constraints as well as Rydberg state dependent anisotropy of the interaction[47]. Plaquette geometries and choices of Rydberg states that give close to equal couplings are presented in Sec. 4.4. Here we simulate the gate performance in the presence of unequal couplings to clarify the robustness of the protocol.

We start with a 3-atom case ($k = 2$) where there are 3 inter-atomic couplings and assume the coupling strengths are $B_0 - \Delta B$, B_0 , $B_0 + \Delta B$. For the 4-atom case ($k = 3$), there are six inter-atomic couplings, which we assume to be $B_0 - \Delta B$, $B_0 - 0.6\Delta B$, $B_0 - 0.2\Delta B$, $B_0 + 0.2\Delta B$, $B_0 + 0.6\Delta B$, $B_0 + \Delta B$. Similarly for the 5-atom case ($k = 4$), there are 10 inter-atomic couplings that are taken to be equally spaced between $B_0 - \Delta B$ and $B_0 + \Delta B$.

Results for a range of ΔB values are shown in Fig. 4.3. Allowing for $\Delta B/B_0$ up to 0.25 the reduction in fidelity is less than 0.001 for $k = 2, 3, 4$. We infer that the gate is very robust with respect to variation in the pair wise coupling strengths. We note that it is important that the coupling strengths are static, since the compensation phases needed for optimal fidelity are dependent on the values of the couplings.

4.2 CZ_k gate protocol

The CZ_k gate can be expressed as

$$\text{CZ}_k = P_{|0\rangle_1} \prod_{j=2}^{k+1} I_j + P_{|1\rangle_1} \prod_{j=2}^{k+1} Z_j. \quad (4.4)$$

If the control qubit is in state $|0\rangle$ there is no operation, and if the control qubit is in

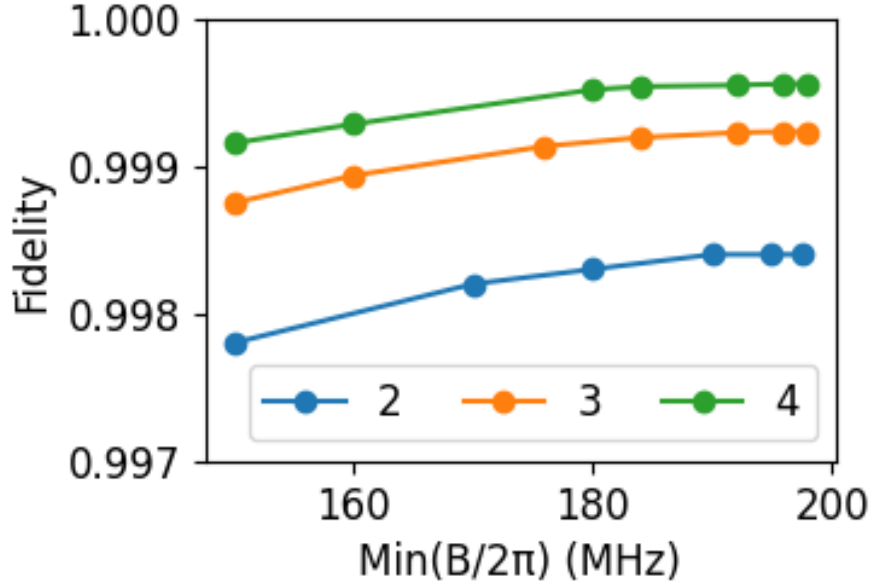


Figure 4.3: C_kZ fidelity for different values of $B_{\min} = B_0 - \Delta B$ values. Parameters are the same as in Fig. 4.2 with $B_0/2\pi = 200$ MHz.

state $|1\rangle$ and an odd number of the target qubits in state $|1\rangle$, then a sign flip is applied to the state.

To achieve a CZ_k gate, a special asymmetric configuration of the inter-atomic couplings is desirable. The coupling between the control qubit and target qubits needs to be symmetric or close to symmetric, and there should be zero coupling between target qubits. If the control-target coupling is strong and the target-target coupling is zero, or sufficiently weaker, then a pulse sequence can be designed that implements a CZ_k gate. Implementations that provide asymmetric interactions can be realized in Rydberg systems where there is a great deal of flexibility in choice of atomic levels and interaction geometry[48, 49, 50, 51].

The CZ_k operation can be implemented efficiently in Rydberg blockaded qubit arrays. To implement the CZ_k gate, we generalize the 2-qubit CZ gate with symmetric pulses[]. Our simulation results show a high fidelity CZ_k gate could be achieved with the symmetric single Gaussian pulse with $\mathcal{F} > 0.99$.

Table 4.2: Fidelity of CZ_k gate with single Gaussian pulse for $k = 2, 3, 4$ with $B/2\pi = 10.75 \text{ MHz}$, $\Omega_0/2\pi = 17 \text{ MHz}$, Rydberg lifetime $\tau = 540 \mu\text{s}$, $\delta t_{initial} = 0.2 \mu\text{s}$, $\Delta_{initial}/2\pi = 23 \text{ MHz}$

k	Fidelity	$\Delta_0/(2\pi) \text{ (MHz)}$	$T \text{ (\mu s)}$
2	0.9988	25.36	0.399
3	0.9928	27.12	0.431
4	0.9974	28.66	0.427

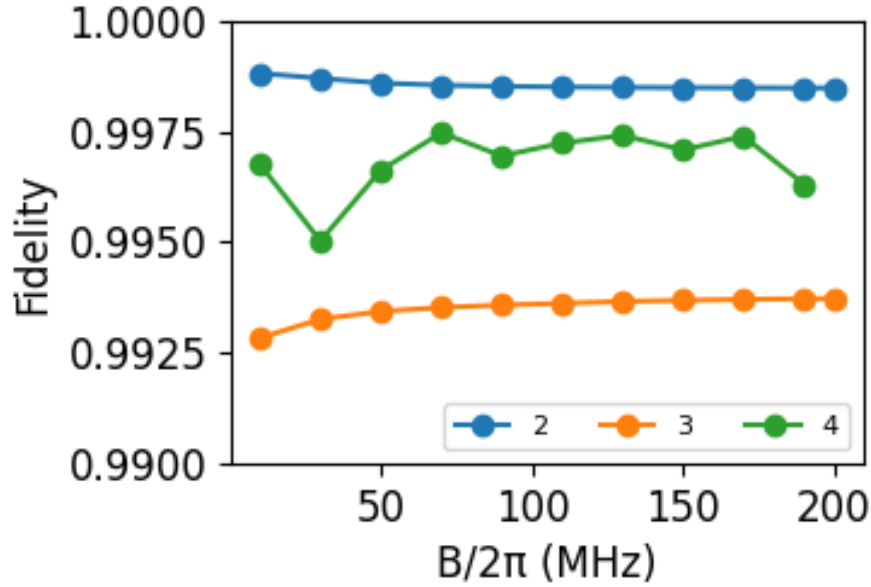


Figure 4.4: Numerical results for CZ_k gate with different target qubit number k and coupling strength B . $\Omega_0/2\pi = 17 \text{ MHz}$, Rydberg lifetime $\tau = 540 \mu\text{s}$, $\delta t_{initial} = 0.2 \mu\text{s}$, $\Delta_{initial}/2\pi = 23 \text{ MHz}$.

4.2.1 Numerical results with zero target-target couplings

In this section we start with the simplest case where the Rydberg coupling strength is exactly zero between all pairs of target qubits. The results are shown in Fig.4.4 and Table 4.2.

4.2.2 Numerical results with finite target-target couplings

In this section we study the nonideal case where the coupling between two target qubits is not negligible. For simplicity we assume that all target-target coupling strengths are the same, and equal to a fraction ϵ of the control-target interaction strength. We then vary ϵ

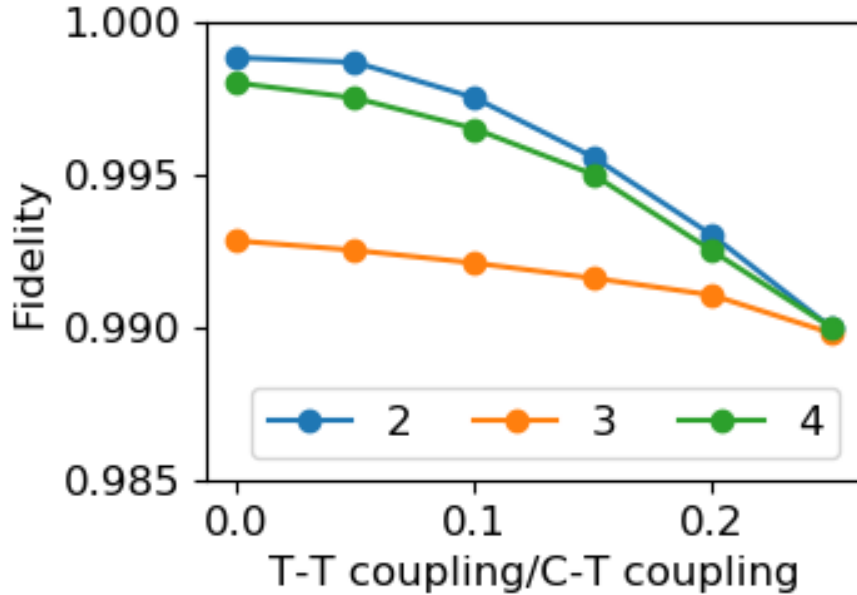


Figure 4.5: Fidelities at different target-target(T-T) coupling values as a percentage of control-target(C-T) coupling for $k=2,3$ and 4 with the single Gaussian pulse. $B_0/2\pi = 10.5$ MHz.

and repeat the optimization in the above section for each value. From the results in Fig. 4.5 we see that the CZ_k fidelity remains above 0.99 for $k = 2, 3, 4$ and $\epsilon < 0.25$.

4.3 Qubit pumping

Rydberg gate errors arise primarily from two effects. The first is coherent rotation errors due to variations in the amplitude or frequency of the laser pulses or due to variations in the atom separation which changes the Rydberg interaction strength. The second type of error arises from spontaneous emission that scales as the ratio t_r/τ where t_r is the effective time that population is in the Rydberg state during the gate, and τ is the Rydberg lifetime. Spontaneous emission also occurs due to scattering from intermediate states that facilitate two-photon Rydberg excitation. The intermediate state scattering can be suppressed far below the scattering from the Rydberg state by using a large one-photon detuning from the intermediate state[52]. Therefore only the Rydberg scattering is included in this analysis.

Spontaneous emission events can be divided into two types. There is redistribution of

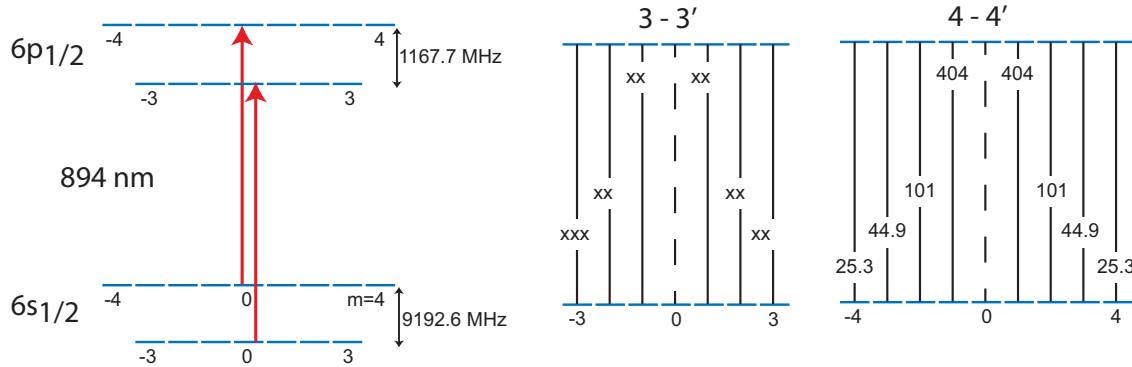


Figure 4.6: Atomic structure for qubit pumping with Cs atoms. The transitions are labeled with the saturation intensity in W/m^2 . The saturation intensity of the transition $|fm\rangle \rightarrow |f'm\rangle$ is $I_{fm,f'm} = \epsilon_0 c \hbar^2 \gamma^2 / 4 d_{fm,f'm}^2$ with $d_{fm,f'm}$ the dipole matrix element, and γ the natural linewidth of the $6p_{1/2}$ level.

population between the qubit states leading to depolarization errors as well as population of Zeeman substates that are outside the computational basis leading to leakage errors. As has been emphasized recently[53], detectable leakage errors lead to higher code thresholds than depolarization errors, provided the leakage sites are subsequently reinitialized in the computational basis. Leakage due to physical loss of an atom requires atom replacement. Leakage into a Zeeman state outside the computational basis, can be repaired using the pumping procedure shown in Fig. 4.6. In the ideal limit this procedure does not change a valid qubit state, but repumps states outside the computational basis into a superposition of qubit states thereby converting leakage errors into depolarization errors.

The basic idea is illustrated in Fig. 4.6. A pair of π polarized optical fields couple $6s_{1/2}, f = 3$ to $6p_{1/2}, f' = 3$ and $6s_{1/2}, f = 4$ to $6p_{1/2}, f' = 4$. Due to selection rules the matrix element is zero for π transitions between states with $f = f'$ and $m = 0$. Therefore any population in a valid qubit state will be largely unaffected while population in states with $m \neq 0$ will be excited to the $6p_{1/2}$ level and decay back to the ground level. The Zeeman state can change by $-1, 0, 1$ in the decay so population accumulates in a qubit state. The dynamics can be analyzed by solving the Lindblad equation or, to a good approximation, using rate equations.

Leakage events during a Rydberg gate can result in population transferring to any

$m \neq 0$ state since the decay process may involve multiple transitions. For highly excited Rydberg states in a room temperature environment roughly half of the decay is to the ground state or first optically excited states and half is driven by blackbody radiation to nearby Rydberg levels, that then decay, or transfer further to other levels. We therefore expect that the distribution among Zeeman states will be peaked close to $m = 0$ and substantially smaller for larger $|m|$. For simplicity we will use a conservative model that assumes equal distribution among Zeeman states. This implies that with probability $1/16$ a spontaneous emission leads to a Z error, probability $1/16$ a depolarization error, and probability $7/8$ a leakage error. The pumping procedure converts leakage errors into depolarization errors so the error model becomes Z errors with probability $1/16$ and depolarization errors with probability $15/16$.

4.4 Plaquette geometries for uniform Rydberg interactions

The multi-qubit protocols described in the following sections operate with the highest fidelity when all atom pairs have an equal strength Rydberg coupling. The interaction strength between atomic Rydberg states depends on the principal quantum number, the interatomic separation, and the geometrical orientation[47]. For alkali atom s orbitals the interaction is very close to isotropic and depends monotonically on the separation R as $1/R^3$ at short range and $1/R^6$ at long range.

Figure 4.7 shows qubit layouts in 2D that can be used to achieve close to equal coupling strengths, and can be used to tile the plane, thereby supporting a scalable qubit register.

For implementation of multi-qubit gates the simplest situation is equal coupling between all atoms. This is automatically the case for $N = 2$ atoms and trivially possible for $N = 3$ using a planar triangular arrangement. For $N > 3$ it is not possible to find a planar geometry that gives equal distances between all atom pairs.

Symmetric interactions can be achieved by coupling to several different Rydberg states as shown in Fig. 4.7. For $N = 4$ atoms we excite states n_1s and n_2s where n_1, n_2 are the principal quantum numbers. The interaction strengths are $V_1 = V_{n_1,n_1}(\sqrt{2}d)$, $V_2 =$

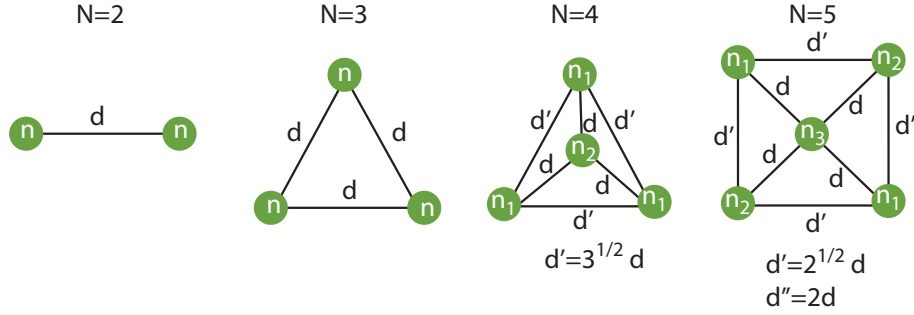


Figure 4.7: Geometrical arrangements and choice of Rydberg states for $N = 2, 3, 4, 5$. Using Rydberg ns states with isotropic interactions equal couplings can be achieved for $N = 2, 3, 4$. For $N = 5$ close to equal couplings are possible as discussed in the text.

$V_{n_2,n_2}(\sqrt{2}d)$, and $V_3 = V_{n_1,n_2}(d)$. The interaction between two atoms in the same Rydberg state has a strong dependence on n but if $n_2 = n_1 \pm 1$ and n_1 is large the small fractional difference between V_{n_1,n_1} and V_{n_2,n_2} scales as $1/n_1$. On the other hand the interaction between different Rydberg states decreases rapidly with $|n_2 - n_1|$. The interaction strength also depends on the angle θ between the inter-atomic axis the quantization axis. We will assume the $m_a = m_b = 1/2$ Rydberg Zeeman states (a, b denote the atoms) are excited with the quantization axis perpendicular to the plane containing the atoms, thus $\theta = \pi/2$. As shown in [54] the interaction at $\theta = \pi/2$ can be either enhanced or suppressed relative to $\theta = 0$ depending on the values of the energy defects and C_3 coefficients for the Förster eigenstates. This additional freedom will allow us to pick states that provide better matching of the interaction strengths.

Here is a first attempt at finding parameters for the 4-qubit case.

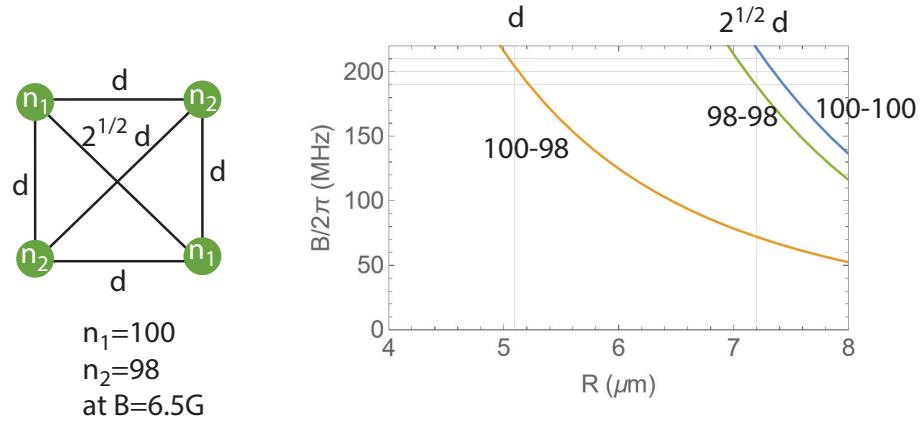


Figure 4.8: Choice of Rydberg states for the 4-qubit case. Using Cs 98s and 100s in a field of $B_z = 6.5$ G all coupling strengths are equalized to within about 5%.

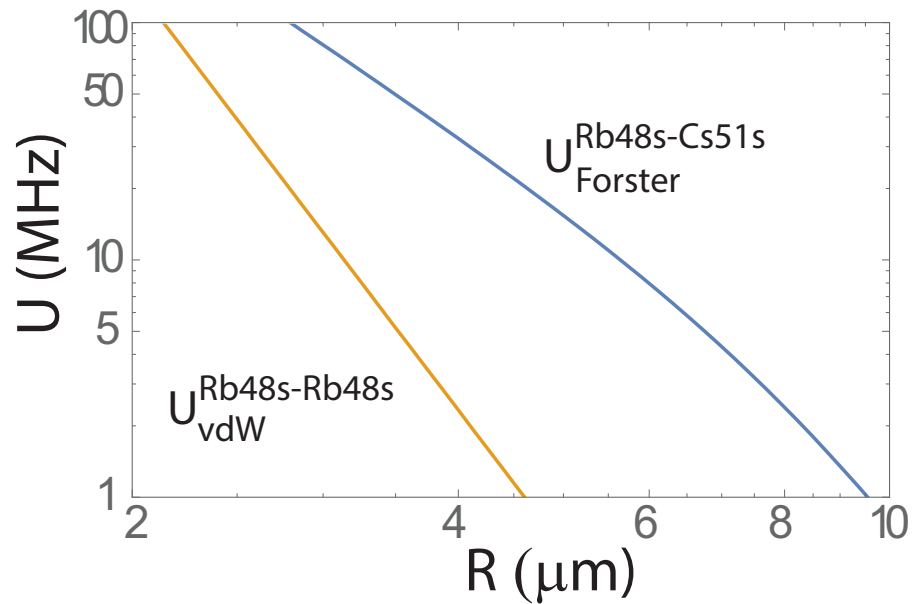


Figure 4.9: Rb-Cs coupling strengths

Chapter 5

Implementation of the Surface Code

The surface code is one of the most promising approaches for fault tolerant quantum computation[55]. Large codes have code distance that scales as the square root of the qubit number, and smaller codes have also been analyzed for near term demonstrations[1]. Neutral atom qubits typically have highly asymmetric noise properties with $T_2 \ll T_1$. Modified surface codes that are optimized for biased noise have been shown to have high error thresholds[56], which suggests study of a neutral atom implementation of the surface code. This was first considered in Ref. [57].

We analyze an improved implementation that uses two atomic species. A two-species approach has several advantages. First, using one-species for data qubits, and one for ancillas, the challenge of eliminating crosstalk onto the data qubits during ancilla measurements can be effectively suppressed[54]. While it is true that the surface code can be implemented in a measurement free modality, doing so requires increased circuit complexity[58]. A second advantage is that asymmetry in the ratio of inter-species to intra-species interaction strength can be used to implement parity checks with a single multi-qubit gate[48, 49], instead of decomposition into a longer series of gate operations.

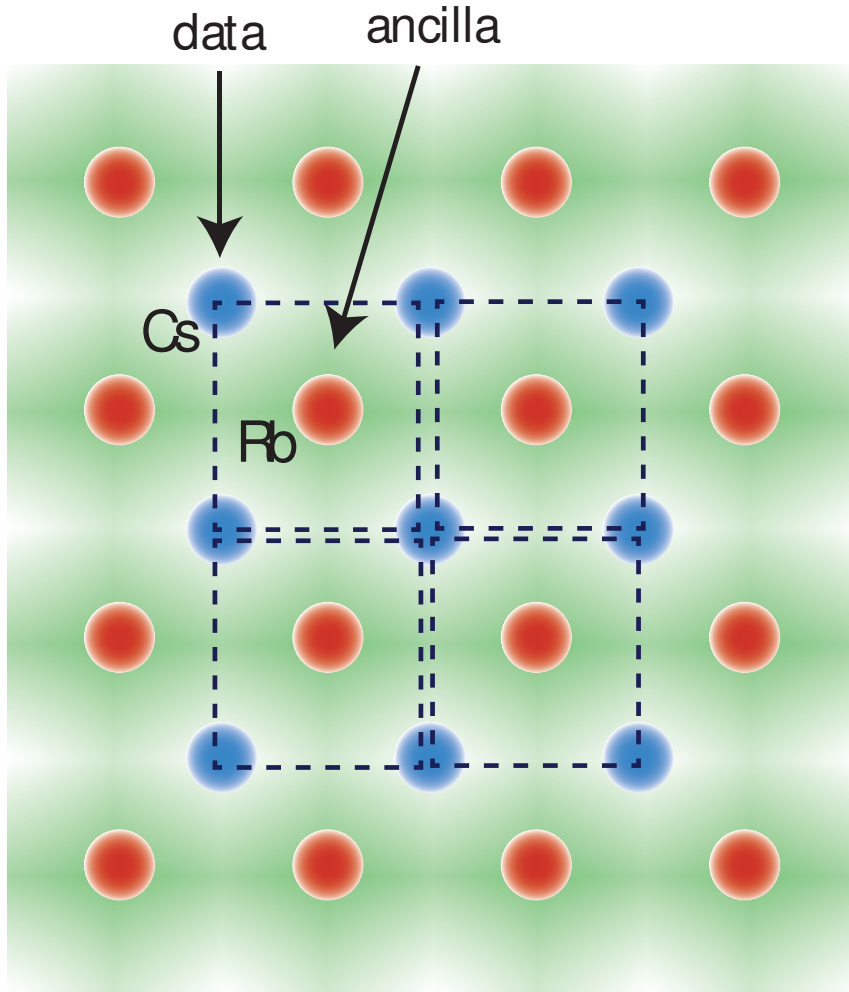


Figure 5.1: (color online) Two species surface code.

5.1 Analysis of the s-13 Code

Circuits for measuring X and Z type stabilizers can be configured in several variants (see for example Fig. 2 in [59]). Using C_Z gates as the two-qubit primitive the stabilizer operation can be implemented in a single step provided the data qubits only couple to the ancilla, but do not interact with each other. A large interaction asymmetry can be achieved as described in [54], using a Rb atom for the ancilla and a Cs atom for the data as described in [54].

The symmetry found here may not be sufficient for high fidelity operation. There are at least two ways in which the asymmetry can be increased. One is to replace the constant

amplitude Rydberg pulses with shaped pulses, possibly using an adiabatic protocol[60], as we discussed in the previous chapter. When designing optimized pulses we may take advantage of the fact that the ancilla qubit always starts in a known state. Therefore the fidelity can be optimized for that case, which relaxes constraints compared to design of a universal gate which must work for an arbitrary input state. A second option is to extend the theory of[54] which considered only ns and np Rydberg levels to higher angular momentum cases which may have larger asymmetries.

A logical qubit can be encoded in a $n \times n$ array of physical qubits[55]. The code distance d scales as the square root of the number of physical qubits whereas the pseudo-threshold has only a weak dependence on the number of physical qubits. While a large code distance is desirable the requirements for qubit number are daunting so it is of interest to explore the performance on small codes.

A minimal instance of the surface code based on a rotated lattice with 17 qubits, 9 for data and 8 ancillas, with code distance $d = 3$ was proposed in[61]. The threshold was analyzed and a version that reuses ancillas to reduce the physical qubit count to 13 was presented in [1]. The performance in a trapped ion implementation was analyzed in [62] where it was found that a two-qubit gate fidelity > 0.999 was required to reach the code threshold.

This code as well as a $d = 5$, 49 qubit version were simulated in [63] using parameters and time scales appropriate for superconducting qubits. It was pointed out that besides the limitations of the quantum hardware very fast classical circuits for error decoding are a requirement due to the relatively short coherence times of superconducting qubits. Since coherence time scales can be several orders of magnitude longer with neutral atom qubits the performance of the classical hardware can be relaxed.

Here we analyze a neutral atom implementation of surface-13 shown in Fig. 5.2. The circuit diagram for one round of X and Z syndrome measurement is shown in Fig. 5.3. Using the multi-qubit CZ gates described in the next section the circuit depth for one round is 12 gate operations: 4 Hadamard gates which are implemented with microwaves

that rotate all data or ancilla qubits in parallel and 4 CZ gates for X and Z parity measurements. The ancilla qubits are measured after the X stabilizer operations and reset for Z stabilizer operations.

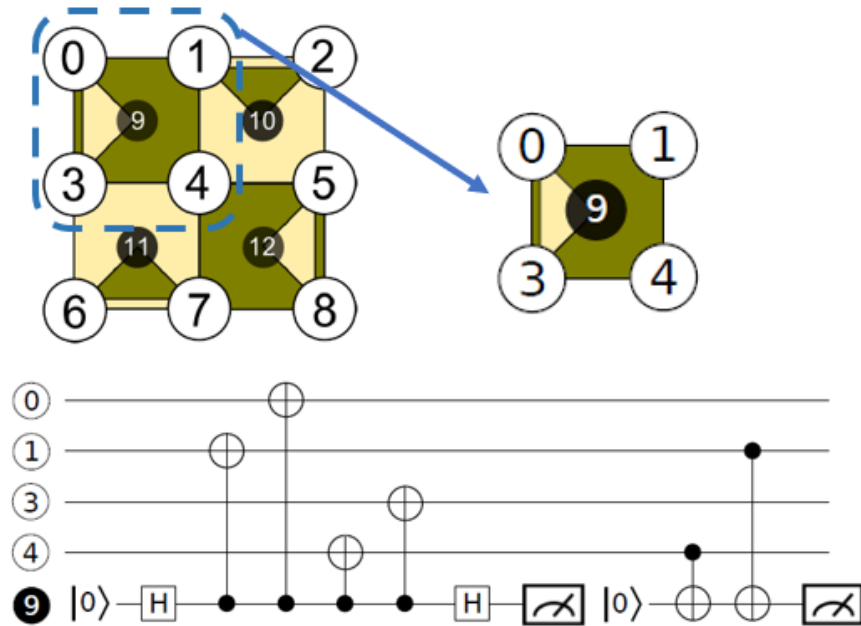


Figure 5.2: Surface-13 layout following[1]. White circles represent data qubits; black circles, syndrome qubits. Dark patches represent X stabilizers; light patches represent Z stabilizers. The circuit of a single plaquette(for example, the plaquette that contains qubit No.0,1,3,4,9) is also shown.

For the s-13 code, after each round of measurement, a decoder is needed to predict where the error occurred and the type of the error, based on the how many ancilla measurements have changed, as shown in Fig. 5.4.

5.2 Single Plaquette Simulation

Preliminary results for stabilizer detection on a single 5-atom plaquette are shown in Fig. 5.5. We see that for very modest Rydberg coupling strengths the stabilizer is extracted onto the ancilla with close to perfect fidelity. The numerics show that for $B/2\pi \geq 16 MHz$ the fidelity of the resulting ancilla state is larger than 0.999 which is well above the surface

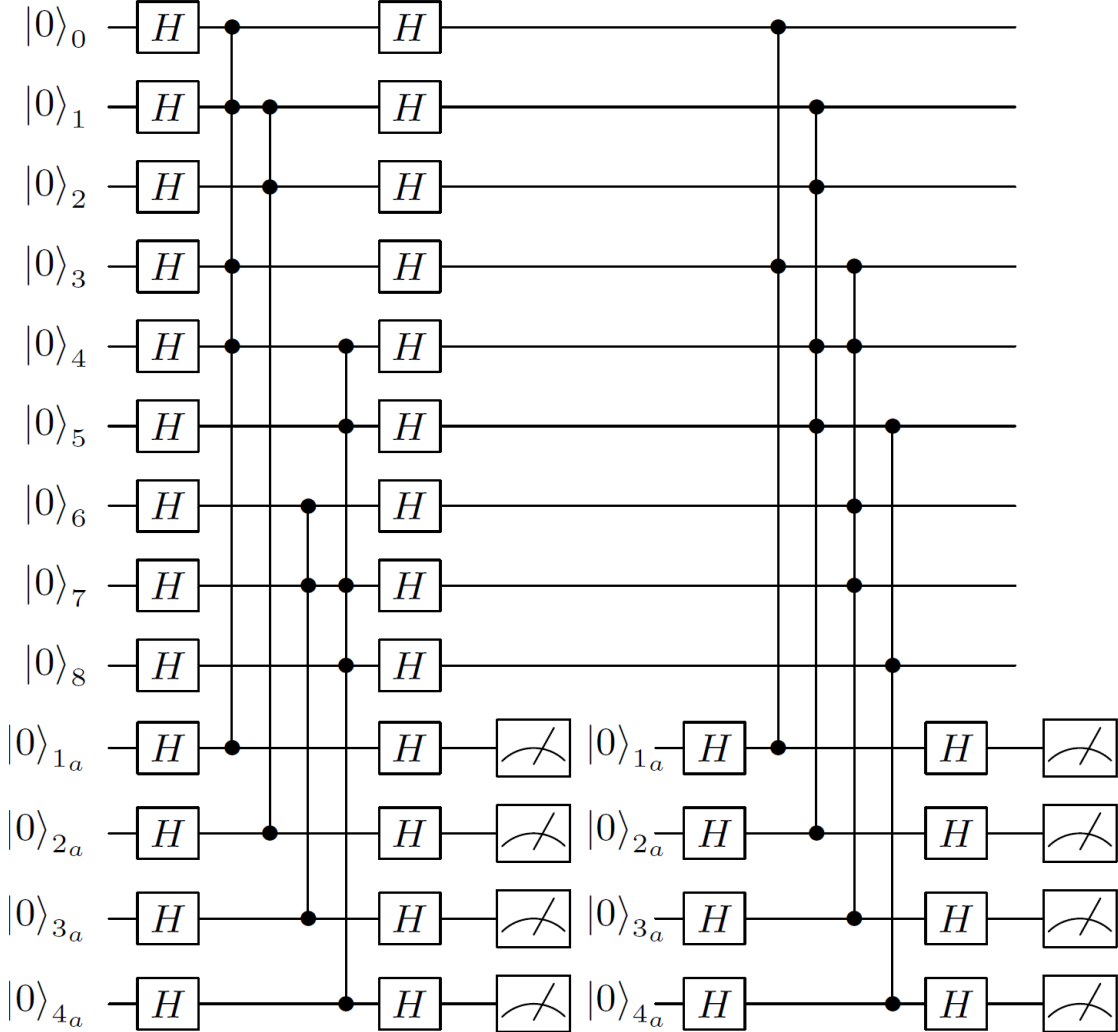


Figure 5.3: Circuit for one round of X and Z stabilizer measurements on surface-13. Qubits $0 - 8$ are data encoded in Cs atoms and qubits $1_a - 4_a$ are ancillas encoded in Rb atoms. Hadamard gates are performed with global microwave pulses at ω_{Cs} and ω_{Rb} .

code threshold. The presented fidelity does not include single qubit errors, measurement errors, or decoherence during the measurement time. The time needed for a single round of error detection is dominated by the ancilla measurement time of several ms. Thus faster measurements would shorten the cycle time and reduce the requirement on gate fidelities. Apart from improvements in optical collection efficiency there are routes to speeding up the measurement. More directly the ancilla qubits may be replaced by multi-atom ensemble qubits. While Rydberg entanglement with fidelity above 0.99 has been demonstrated in

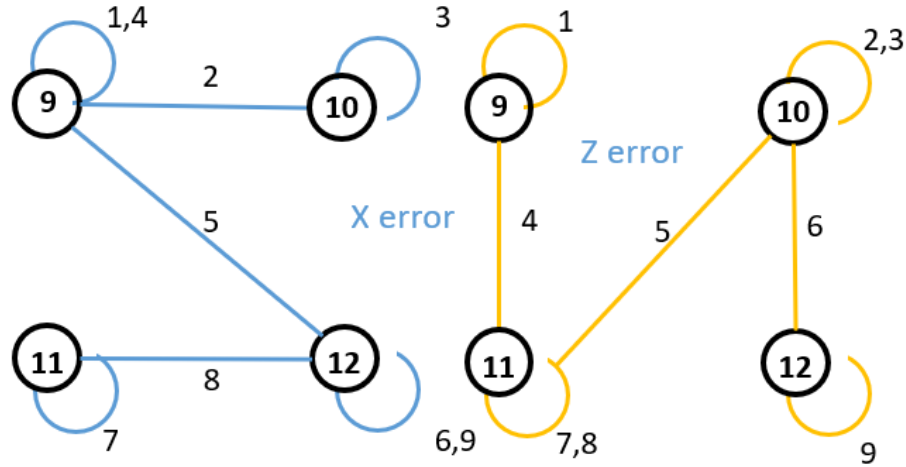


Figure 5.4: Decoder for s-13 code. Black circles show possible ancilla flips. Blue or yellow lines show the possible X or Z errors on the listed qubits that could cause the measured qubit flip. For example, a single ancilla flip during an X measurement on 9 could indicate X error on data qubit 1 or 4; ancilla flips on 9 and 10 during an X measurement indicates X error on data qubit 2.

a one-dimensional geometry, the experimental results in a 2D array have not yet reached that level.

As we have shown in the previous chapter, high-fidelity multi-qubit gates could be achieved for neutral atoms. Assume that for a single plaquette with four data qubits and one ancilla qubit, the Rydberg coupling strengths between the ancilla qubit and all the data qubits are the same, and there are zero coupling between any pairs of data qubits. This configuration is physically achievable by tuning the ancilla-data distance and data-data distance in the plaquette geometry. As Fig.5.6 and Fig.5.7 shows, both standard stabilizer circuits can be converted to a sequence of four CZ gates. The four sequential CZ is equivalent to a CZ₄ gate, which means we can do the stabilizer measurement with a single multi-qubit gate. This gives a faster code cycle time, and avoids error from a certain data qubit to affect other qubits.

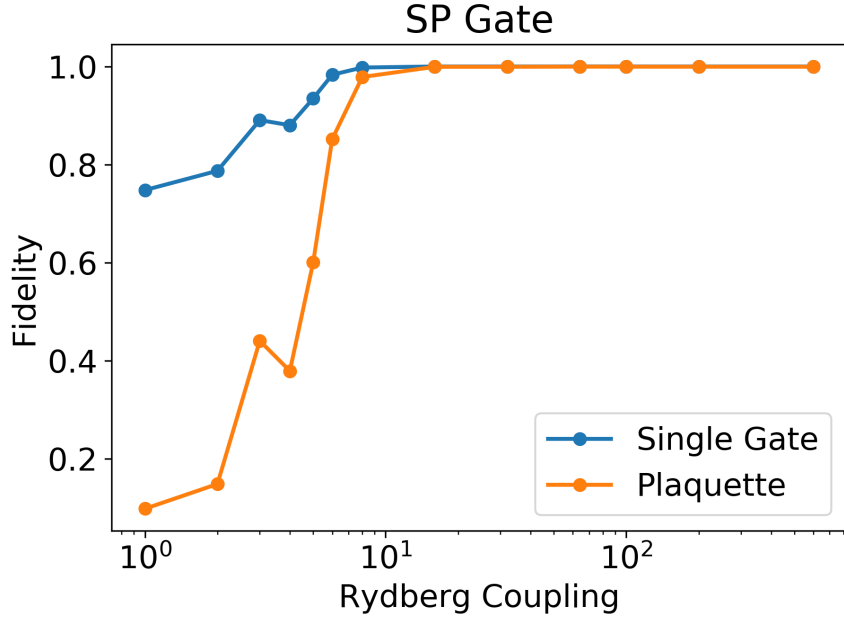


Figure 5.5: Simulation results using QuaC for stabilizer detection on a single 5-atom plaquette. All qubits were initialized in the superposition state $(|0\rangle + |1\rangle)/\sqrt{2}$, and a series of four ancilla-data CZ gates was applied sequentially. Single qubit gates were assumed to have perfect fidelity. The presented fidelity is the overlap between the calculated and ideal final state.

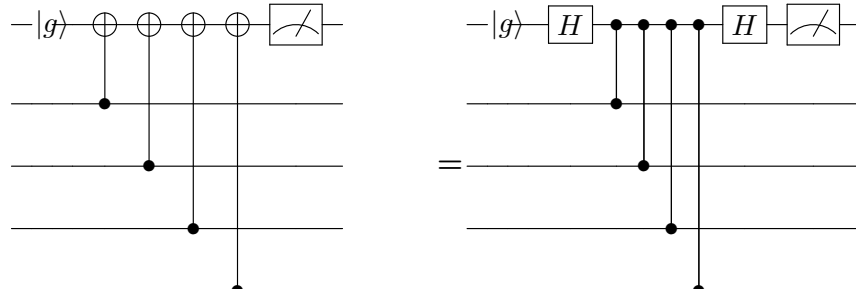


Figure 5.6: Z stabilizer

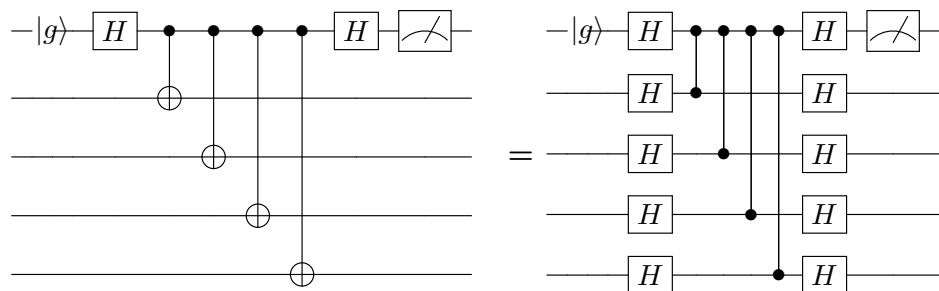


Figure 5.7: X stabilizer

Chapter 6

Conclusion and Outlook

In this thesis we presented theoretical analysis of various aspects for improving the performance of quantum computing with neutral atoms. We theoretically investigated errors in the Rabi oscillation process of neutral atoms. We focused on a noise mechanism that dominates many qubit experiments: phase fluctuations of the driving laser. We considered both one and two-photon Rabi oscillations, and also considered generic noise spectra, such as flat-background (white) noise, and noise peaked at finite frequencies. We have specifically considered the weak-noise regime, which is typical of modern qubit experiments. In this limit, we uncover simple relations between the underlying phase-noise spectra and noise spectra measured in self-heterodyne experiments. We also studied the effect of band-limited white noise. Further studies are needed to elucidate the influence of phase noise on coherence properties of qubit states. We are also planning to set up experiments in the AQuA lab to compare our theory with experimentally measured errors.

We also analyzed protocols for achieving high-fidelity multi-qubit C_kZ and CZ_k gates. We examined two possible adiabatic pulses for achieving the two complimentary gates. We optimized pulse parameters for each gate type, as well as the single qubit phase rotations implemented on each qubit after the gate. Symmetry on Rydberg coupling strengths between qubit pairs is needed. For C_kZ equal coupling strengths between all pairs are needed, while for CZ_k gates we need equal coupling strengths between all control-target

pairs and zero coupling between target-target pairs. We analyzed geometries for the ideal coupling and studied the stability of the multi-qubit gates against finite variations in coupling strengths. We also analyzed the performance of implementing a simple surface code (s13) with neutral atoms, with the optimized multi-qubit gate mentioned above. Future work would involve analyzing the gate and the surface code with measured parameters from the experiment, achieving the desired geometry for the multi-qubit gates, and testing the surface code on our neutral atom qubit array system. For the surface code it would also be beneficial to examine the advantage of using different atomic species for the ancilla and data qubits both theoretically and experimentally.

Appendix A

Parameters for multi-qubit gates

A.1 Parameters for CZ_k gate with single Gaussian pulses

The CZ_k gate parameters for each point on Fig.4.4 and Fig.4.5 are shown in Table.A.1-A.3.

Table A.1: Parameters for CZ_k gate with single Gaussian pulse for $k = 2$, $\Omega_0/2\pi = 17$ MHz, $\delta t_{initial} = 0.2\mu s$, $\Delta_{initial}/\Omega = 0.5$

$B/(2\pi)$	Fidelity	Δ/Ω	δt (μs)	ϕ_1	ϕ_2	ϕ_3
10.75	0.9988	0.2383	0.3139	1.1188	-1.8854	-1.8854
20	0.9988	0.4334	0.4067	1.3494	-1.6466	-1.6466
30	0.9987	0.5032	0.4097	-0.0577	-3.0456	-3.0456
40	0.9986	0.5475	0.4113	-0.8702	2.4288	2.4289
50	0.9986	0.5785	0.4124	-1.4052	1.8966	1.8966
60	0.9986	0.6016	0.4131	-1.7885	1.5151	1.5152
70	0.9985	0.6196	0.4137	-2.0763	1.2283	1.2284
80	0.9985	0.6341	0.4141	-2.3013	1.0041	1.0041
90	0.9985	0.6459	0.4144	-2.4851	0.8207	0.8207
100	0.9985	0.6558	0.4147	3.6503	0.6738	0.6739
110	0.9985	0.6643	0.4149	3.5249	0.5486	0.5485
120	0.9985	0.6716	0.4151	3.4177	0.4415	0.4416
130	0.9985	0.6780	0.4153	3.3266	0.3506	0.3508
140	0.9985	0.6835	0.4155	3.2464	0.2706	0.2706
150	0.9985	0.6884	0.4156	3.1754	0.1996	0.1996
160	0.9985	0.6927	0.4156	3.1130	0.1374	0.1375
170	0.9985	0.6966	0.4158	3.0579	0.0828	0.0829
180	0.9985	0.7002	0.4158	3.0067	0.0312	0.0313
190	0.9985	0.7034	0.4159	2.9629	-0.0121	-0.0123
200	0.9985	0.7064	0.4160	2.9220	-0.0529	-0.0527

Table A.2: Parameters for CZ_k gate with single Gaussian pulse for $k = 3$, $\Omega_0/2\pi = 17 \text{ MHz}$, $\delta t_{initial} = 0.2\mu\text{s}$, $\Delta_{initial}/\Omega = 0.5$

$B/(2\pi)$	Fidelity	Δ/Ω	$\delta t (\mu\text{s})$	ϕ_1	ϕ_2	ϕ_3	ϕ_4
10	0.9928	0.4979	0.1680	0.1090	-1.6459	-1.6459	-1.6458
20	0.9931	0.5098	0.1425	-1.3888	3.3518	3.3518	3.3519
30	0.9932	0.5315	0.1395	-1.8388	3.0485	3.0483	3.0485
40	0.9934	0.5475	0.1370	-2.1406	2.8189	2.8193	2.8191
50	0.9934	0.5594	0.1349	-2.3549	2.6464	2.6466	2.6467
60	0.9935	0.5682	0.1331	-2.5160	2.5125	2.5125	2.5126
70	0.9935	0.5750	0.1316	-2.6408	2.4063	2.4061	2.4064
80	0.9935	0.5802	0.1303	-2.7438	2.3164	2.3163	2.3162
90	0.9936	0.5841	0.1290	-2.8296	2.2401	2.2399	2.2401
100	0.9936	0.5874	0.1278	-2.9054	2.1703	2.1702	2.1701
110	0.9936	0.5897	0.1267	-2.9715	2.1086	2.1087	2.1087
120	0.9936	0.5696	0.1137	2.9517	1.6890	1.6889	1.6889
130	0.9937	0.5709	0.1136	2.9255	1.6744	1.6744	1.6743
140	0.9937	0.5721	0.1135	2.9027	1.6615	1.6619	1.6617
150	0.9937	0.5734	0.1133	2.8815	1.6484	1.6485	1.6483
160	0.9937	0.5744	0.1133	2.8638	1.6382	1.6381	1.6382
170	0.9937	0.5753	0.1132	2.8472	1.6277	1.6280	1.6278
180	0.9937	0.5762	0.1130	2.8318	1.6181	1.6179	1.6181
190	0.9937	0.5770	0.1130	2.8185	1.6099	1.6098	1.6097
200	0.9937	0.5777	0.1129	2.8068	1.6029	1.6028	1.6028

Table A.3: Parameters for CZ_k gate with single Gaussian pulse for $k = 4$, $\Omega_0/2\pi = 17 \text{ MHz}$, $\delta t_{initial} = 0.2\mu\text{s}$, $\Delta_{initial}/\Omega = 0.5$

$B/(2\pi)$	Fidelity	Δ/Ω	$\delta t (\mu\text{s})$	ϕ_1	ϕ_2	ϕ_3	ϕ_4	ϕ_5
10	0.9967	0.5045	0.2222	2.0155	0.5987	0.5987	0.5987	0.5985
30	0.9950	0.5045	0.2222	0.5926	0.3988	0.3984	0.3987	0.3986
50	0.9966	0.5654	0.1654	-1.7351	-2.5526	-2.5523	-2.5522	-2.5521
70	0.9975	0.6000	0.1101	2.8183	1.3092	1.3090	1.3092	1.3088
90	0.9969	0.5358	0.1214	3.0567	2.0636	2.0635	2.0633	2.0631
110	0.9942	0.5899	0.2278	-0.6421	-0.3472	-0.3471	-0.3469	-0.3472
150	0.9971	0.5585	0.1184	2.7948	1.8082	1.8080	1.8079	1.8083

A.2 Parameters for C_kZ gate with ARP pulses

The C_kZ gate parameters for each point on Fig.4.2 and Fig.4.3 are shown in the tables below.

Table A.4: Fidelities for CZ_k gate with single Gaussian pulse for $k = 3, 4, 5$ with different data-data coupling strengths at $B = 10$. B is the coupling strength between control and target qubits. d-d ratio = $B_{\text{data-data}}/B$. Gate parameters are the corresponding Δ , δt and local phase numbers for $B = 10$ for $k = 2, 3, 4$.

d-d ratio	Fidelity($k = 2$)	Fidelity($k = 3$)	Fidelity($k = 4$)
0	0.9988	0.9928	0.9938
0.05	0.9987	0.9925	0.9934
0.1	0.9975	0.9921	0.9926
0.15	0.9956	0.9916	0.9916
0.2	0.9930	0.9910	0.9904
0.25	0.9900	0.9904	0.9890

Table A.5: Parameters for C_kZ gate with ARP pulse for $k = 2$, $\Omega_0/2\pi = 17$ MHz, $T_{\text{initial}} = 0.54\mu\text{s}$, $\Delta_{\text{initial}} = 23$ MHz

$B/(2\pi)$	Fidelity	$\Delta/(2\pi)$	δt (μs)	ϕ_1	ϕ_2	ϕ_3
200	0.9984	23.7883	0.5095	0.4628	0.4625	0.4625
300	0.9992	23.2001	0.5185	0.3127	0.3128	0.3128
400	0.9994	23.1993	0.5212	0.2355	0.2358	0.2356
500	0.9996	23.1606	0.5226	0.1890	0.1887	0.1890
600	0.9996	23.2264	0.5235	0.1578	0.1575	0.1576

Table A.6: Parameters for C_kZ gate with ARP pulse for $k = 3$, $\Omega_0/2\pi = 17$ MHz, $T_{\text{initial}} = 0.54\mu\text{s}$, $\Delta_{\text{initial}} = 23$ MHz

$B/(2\pi)$	Fidelity	$\Delta/(2\pi)$	δt (μs)	ϕ_1	ϕ_2	ϕ_3	ϕ_4
200	0.9992	23.9516	0.5312	0.5634	0.5634	0.5632	0.5634
300	0.9995	23.8794	0.5350	0.3769	0.3767	0.3769	0.3769
400	0.9996	23.9011	0.5365	0.2832	0.2830	0.2828	0.2830
500	0.9997	23.9184	0.5376	0.2266	0.2267	0.2268	0.2268
600	0.9997	23.9621	0.5387	0.1890	0.1892	0.1893	0.1894

Table A.7: Parameters for C_kZ gate with ARP pulse for $k = 4$, $\Omega_0/2\pi = 17$ MHz, $T_{\text{initial}} = 0.54\mu\text{s}$, $\Delta_{\text{initial}} = 23$ MHz

$B/(2\pi)$	Fidelity	$\Delta/(2\pi)$	δt (μs)	ϕ_1	ϕ_2	ϕ_3	ϕ_4	ϕ_5
200	0.9996	24.4616	0.4908	0.6134	0.6132	0.6134	0.6132	0.6131
300	0.9997	24.4448	0.5261	0.4074	0.4075	0.4074	0.4076	0.4073
400	0.9997	24.3935	0.5264	0.3051	0.3052	0.3054	0.3054	0.3053
500	0.9997	24.4084	0.5225	0.2441	0.2438	0.2439	0.2441	0.2439
600	0.9997	24.4088	0.5193	0.2035	0.2031	0.2035	0.2033	0.2032

Table A.8: Fidelities for C_kZ gate with single Gaussian pulse for $k = 3, 4, 5$ with different inter-atomic coupling strengths at $B_0 = 0$. For $k = 2$, there are 3 different coupling strengths, for $k = 3$, there are 6 different coupling strengths, and for $k = 4$, there are 10 different coupling strengths. For each k number, the coupling strengths are equally spaced between $B_0 - \Delta B$ and $B_0 + \Delta B$. The Ω , Δ , T and single qubit rotation phase parameters are from the $B = 200$ cases for $k = 2, 3, 4$.

k=2	Fidelity(k=2)	k=3	Fidelity(k=4)	k=4	Fidelity(k = 4)
197.5	0.9984	198	0.9992	198	0.9996
195	0.9984	196	0.9992	196	0.9996
190	0.9984	192	0.9992	192	0.9995
180	0.9983	184	0.9992	184	0.9995
170	0.9982	176	0.9991	176	0.9995
150	0.9978	160	0.9989	160	0.9993

Appendix B

Sensitivity of CZ_k and C_kZ gates to phase variations

We vary the single-qubit rotation phase of the control qubit and the first target qubit to check the sensitivity of CZ_k and C_kZ gates to single qubit phase variations. The results are shown in Fig.B.1 and Fig.B.2.

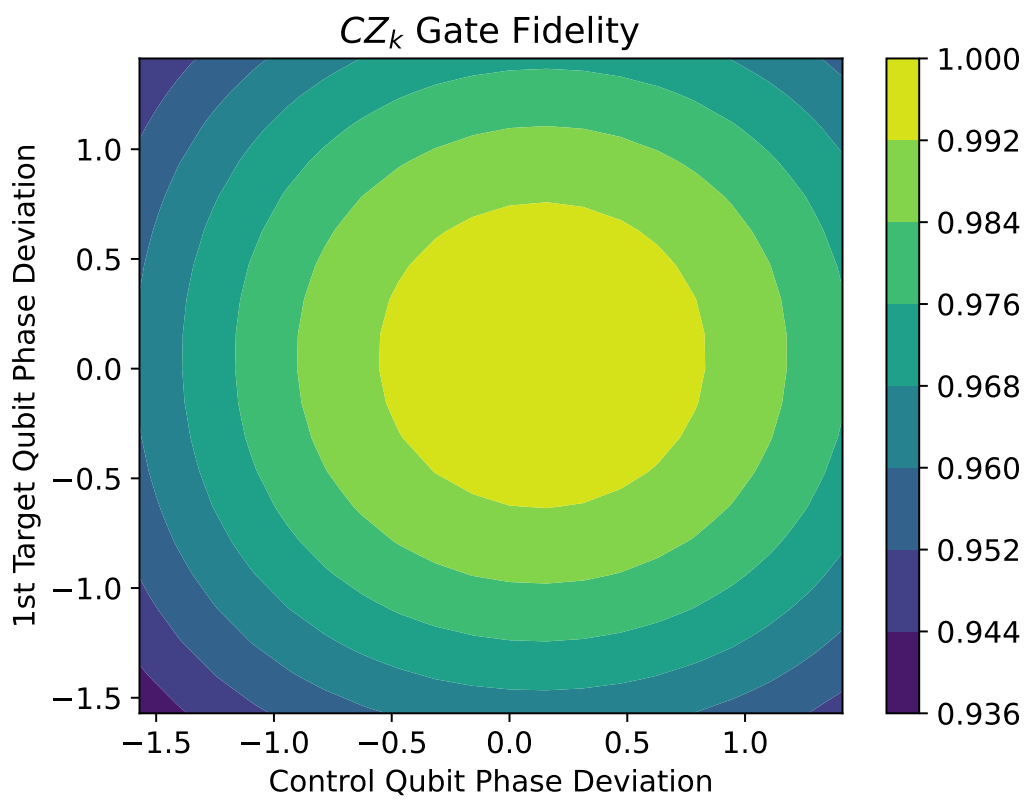


Figure B.1: Fidelity of the CZ_k gate with the single Gaussian pulse with variations of the single-qubit rotation phase on the control and the first target qubit. Variation range is $[-\pi/2, \pi/2]$

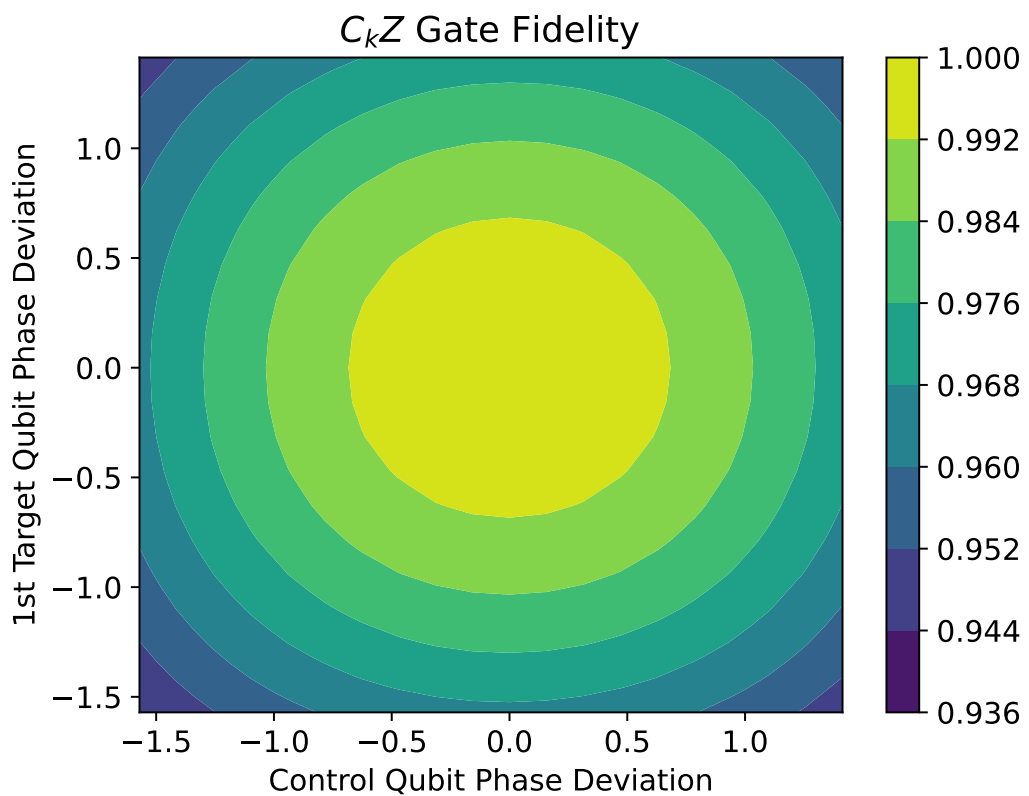


Figure B.2: Fidelity of the C_kZ gate with the ARP pulse with variations of the single-qubit rotation phase on the control and the first target qubit. Variation range is $[-\pi/2, \pi/2]$

Appendix C

QuaC simulator

QuaC (Quantum in C)[64] is a parallel time dependent open quantum systems solver, written by Matthew Otten (otten.matt@gmail.com). QuaC utilizes PETSc (www.mcs.anl.gov/petsc) for parallelization and linear algebra and features are still regularly being added.

The QuaC simulator is capable of modeling open quantum systems, with support for systems of qubits as well as more general systems. It uses the Lindblad master equation formulation and evolves the density matrix. QuaC is able to describe many Markovian, non-unitary evolution processes, as long as the environment is large compared to the system and only weakly coupled. For example, it can model amplitude damping, dephasing, thermal effects, and even some forms of correlated noise. Moreover, QuaC has the flexibility to model quantum architectures at gate or pulse levels.

QuaC has been parallelized to run on supercomputers, and ongoing work of the investigators optimizes the simulator for use on the upcoming exa-scale supercomputer Aurora. The main challenge with QuaC is large memory footprint required to store the density matrix. As a result, the maximum size of systems that can be simulated is approximately 25 qubits.

Bibliography

- [1] Y. Tomita and K. M. Svore. Low-distance surface codes under realistic quantum noise. *Phys. Rev. A*, 90:062320, 2014.
- [2] Peter W Shor. Polynomial-time algorithms for prime factorization and discrete logarithms on a quantum computer. *SIAM review*, 41(2):303–332, 1999.
- [3] X.-Q. Zhou, P. Kalaswan, T. C. Ralph, and J. L. O’Brien. Calculating unknown eigenvalues with a quantum algorithm. *Nat. Phot.*, 7:223–228, 2013.
- [4] E. A. Martinez, C. A. Muschik, P. Schindler, D. Nigg, A. Erhard, M. Heyl, P. Hauke, M. Dalmonte, T. Monz, P. Zoller, and R. Blatt. Real-time dynamics of lattice gauge theories with a few-qubit quantum computer. *Nature*, 534:516–519, 2016.
- [5] C. Figgatt, D. Maslov, K.A. Landsman, N.M. Linke, S. Debnath, and C. Monroe. Complete 3-qubit Grover search on a programmable quantum computer. *Nat. Commun.*, 8:1918, 2017.
- [6] Leonardo DiCarlo, Jerry M Chow, Jay M Gambetta, Lev S Bishop, Blake R Johnson, DI Schuster, J Majer, Alexandre Blais, Luigi Frunzio, SM Girvin, et al. Demonstration of two-qubit algorithms with a superconducting quantum processor. *Nature*, 460(7252):240–244, 2009.
- [7] M.P. Harrigan, K. J. Sung, M. Neeley, K. J. Satzinger, F. Arute, K. Arya, J. Atalaya, J. C. Bardin, R. Barends, S. Boixo, M. Broughton, B. B. Buckley, D. A. Buell, B. Burkett, N. Bushnell, Y. Chen, Z. Chen, B. Chiaro, R. Collins, W. Courtney, S. Demura,

- A. Dunsworth, D. Eppens, A. Fowler, B. Foxen, C. Gidney, M. Giustina, R. Graff, S. Habegger, A. Ho, S. Hong, T. Huang, L. B. Ioffe, S. V. Isakov, E. Jeffrey, Z. Jiang, C. Jones, D. Kafri, K. Kechedzhi, J. Kelly, S. Kim, P. V. Klimov, A. N. Korotkov, F. Kostritsa, D. Landhuis, P. Laptev, M. Lindmark, M. Leib, O. Martin, J. M. Martinis, J. R. McClean, M. McEwen, A. Megrant, X. Mi, M. Mohseni, W. Mruczkiewicz, J. Mutus, O. Naaman, C. Neill, F. Neukart, M. Y. Niu, T. E. O'Brien, B. O'Gorman, E. Ostby, A. Petukhov, H. Putterman, C. Quintana, P. Roushan, N. C. Rubin, D. Sank, A. Skolik, V. Smelyanskiy, D. Strain, M. Streif, M. Szalay, A. Vainsencher, T. White, Z. J. Yao, P. Yeh, A. Zalcman, L. Zhou, H. Neven, D. Bacon, E. Lucero, E. Farhi, and R. Babbush. Quantum approximate optimization of non-planar graph problems on a planar superconducting processor. *Nat. Phys.*, 17:332–336, 2021.
- [8] T. F. Watson, S. G. J. Philips, E. Kawakami, D. R. Ward, P. Scarlino, M. Veldhorst, D. E. Savage, M. G. Lagally, Mark Friesen, S. N. Coppersmith, M. A. Eriksson, and L. M. K. Vandersypen. A programmable two-qubit quantum processor in silicon. *Nature*, 555:633–637, 2018.
- [9] Victor Acosta and Philip Hemmer. Nitrogen-vacancy centers: Physics and applications. *MRS bulletin*, 38(2):127–130, 2013.
- [10] M. Saffman, D. Oblak, J. Appel, and E. S. Polzik. Spin squeezing of atomic ensembles by multi-colour quantum non-demolition measurements. *Phys. Rev. A*, 79:023831, 2009.
- [11] M. Saffman, T. G. Walker, and K. Mølmer. Quantum information with Rydberg atoms. *Rev. Mod. Phys.*, 82:2313–2363, 2010.
- [12] T. Graham, M. Kwon, B. Grinkemeyer, A. Marra, X. Jiang, M. Lichtman, Y. Sun, M. Ebert, and M. Saffman. Rydberg mediated entanglement in a two-dimensional neutral atom qubit array. *Phys. Rev. Lett.*, 123:230501, 2019.

- [13] T. M. Graham, Y. Song, J. Scott, C. Poole, L. Phuttitarn, K. Jooya, P. Eichler, X. Jiang, A. Marra, B. Grinkemeyer, M. Kwon, M. Ebert, J. Cherek, M. T. Lichtman, M. Gillette, J. Gilbert, D. Bowman, T. Ballance, C. Campbell, E. D. Dahl, O. Crawford, N. S. Blunt, B. Rogers, T. Noel, and M. Saffman. Multi-qubit entanglement and algorithms on a neutral-atom quantum computer. *Nature*, 604:457–462, 2022.
- [14] Daniel M Greenberger, Michael A Horne, and Anton Zeilinger. Going beyond bell’s theorem. In *Bell’s theorem, quantum theory and conceptions of the universe*, pages 69–72. Springer, 1989.
- [15] A. Aspuru-Guzik, A. D. Dutoi, P. J. Love, and M. Head-Gordon. Simulated quantum computation of molecular energies. *Science*, 309:1704–1707, 2005.
- [16] Edward Farhi, Jeffrey Goldstone, and Sam Gutmann. A quantum approximate optimization algorithm. *arXiv preprint arXiv:1411.4028*, 2014.
- [17] RWP Drever, John L Hall, FV Kowalski, J. Hough, GM Ford, AJ Munley, and H Ward. Laser phase and frequency stabilization using an optical resonator. *Applied Physics B*, 31(2):97–105, 1983.
- [18] TW Hansch and B Couillaud. Laser frequency stabilization by polarization spectroscopy of a reflecting reference cavity. *Optics communications*, 35(3):441–444, 1980.
- [19] T Ukachi, RJ Lane, WR Bosenberg, and CL Tang. Phase-matched second-harmonic generation and growth of a LiB₃O₅ crystal. *JOSA B*, 9(7):1128–1133, 1992.
- [20] Yong-Ho Cha, Kwang-Hoon Ko, Gwon Lim, Jae-Min Han, Hyun-Min Park, Taek-Soo Kim, and Do-Young Jeong. Generation of continuous-wave single-frequency 1.5 w 378 nm radiation by frequency doubling of a ti: sapphire laser. *Applied optics*, 49(9):1666–1670, 2010.
- [21] Tim Freegarde and Claus Zimmermann. On the design of enhancement cavities for second harmonic generation. *Optics Communications*, 199(5-6):435–446, 2001.

- [22] JS Nielsen. Generation of 90-mw continuous-wave tunable laser light at 280 nm by frequency doubling in a kdp crystal. *Optics letters*, 20(8):840–842, 1995.
- [23] Valentin G Dmitriev, Gagik G Gurzadyan, and David N Nikogosyan. *Handbook of nonlinear optical crystals*, volume 64. Springer, 2013.
- [24] K Kato. Temperature-tuned 90 deg. phase-matching properties of LiB₃O₅. *IEEE journal of quantum electronics*, 30(12):2950–2952, 1994.
- [25] GD Boyd and DA Kleinman. Parametric interaction of focused gaussian light beams. *Journal of Applied Physics*, 39(8):3597–3639, 1968.
- [26] MH Dunn and AI Ferguson. Coma compensation in off-axis laser resonators. *Optics Communications*, 20(2):214–219, 1977.
- [27] John A Gubner. *Probability and random processes for electrical and computer engineers*. Cambridge University Press, 2006.
- [28] James A Barnes, Andrew R Chi, Leonard S Cutler, Daniel J Healey, David B Lee-son, Thomas E McGunigal, James A Mullen, Warren L Smith, Richard L Sydnor, Robert FC Vessot, et al. Characterization of frequency stability. *IEEE transactions on instrumentation and measurement*, (2):105–120, 1971.
- [29] Alexis Mérigaud and John V Ringwood. Free-surface time-series generation for wave energy applications. *IEEE Journal of Oceanic Engineering*, 43(1):19–35, 2017.
- [30] DS Elliott, Rajarshi Roy, and SJ Smith. Extracavity laser band-shape and bandwidth modification. *Physical Review A*, 26(1):12, 1982.
- [31] Miao Zhu and John L Hall. Stabilization of optical phase/frequency of a laser system: application to a commercial dye laser with an external stabilizer. *JOSA B*, 10(5):802–816, 1993.

- [32] Gianni Di Domenico, Stéphane Schilt, and Pierre Thomann. Simple approach to the relation between laser frequency noise and laser line shape. *Applied optics*, 49(25):4801–4807, 2010.
- [33] Fritz Riehle. *Frequency standards: basics and applications*. John Wiley & Sons, 2006.
- [34] P. Gallion and G. Debarge. Quantum phase noise and field correlation in single frequency semiconductor laser systems. *IEEE Journal of Quantum Electronics*, 20(4):343–349, 1984.
- [35] Y. Li, Z. Fu, L. Zhu, H. Zhu, J. Zhong, P. Xu, X. Chen, J. Wang, and M. Zhan. Laser frequency noise measurement using an envelope-ratio method based on a delayed self-heterodyne interferometer. *Optics Communications*, 435:244–250, 2019.
- [36] H. Tsuchida. Laser frequency modulation noise measurement by recirculating delayed self-heterodyne method. *Optics Letters*, 36:681–683, 2011.
- [37] L. Richter, H. Mandelberg, M. Kruger, and P. McGrath. Linewidth determination from self-heterodyne measurements with subcoherence delay times. *IEEE Journal of Quantum Electronics*, 22(11):2070–2074, 1986.
- [38] M. J. Tucker, P. G. Challenor, and D. J. T Carter. Numerical simulation of a random sea. *Applied Ocean Research*, 6:118–122, 1984.
- [39] J.-B. Saulnier, P. Ricci, A. Clément, and A. D. O. Falcão. Mean power output estimation of WECs in simulated sea. *Proc. 8th Eur. Wave Tidal Energy Conf.*, 710:891–900, 2009.
- [40] Th. Haslwanter, H. Ritsch, J. Cooper, and P. Zoller. Laser-noise-induced population fluctuations in two- and three-level systems. *Phys. Rev. A*, 38:5652–5659, Dec 1988.
- [41] R. Kubo. Stochastic liouville equations. *J. Math. Phys.*, 4:174–183, 1963.
- [42] I. I. Beterov, M. Saffman, E. A. Yakshina, V. P. Zhukov, D. B. Tretyakov, V. M. Entin, I. I. Ryabtsev, C. W. Mansell, C. MacCormick, S. Bergamini, and M. P.

- Fedoruk. Quantum gates in mesoscopic atomic ensembles based on adiabatic passage and Rydberg blockade. *Phys. Rev. A*, 88:010303(R), 2013.
- [43] I. I. Beterov, D. B. Tretyakov, V. M. Entin, E. A. Yakshina, I. I. Ryabtsev, M. Saffman, and S. Bergamini. Application of adiabatic passage in Rydberg atomic ensembles for quantum information processing. *J. Phys. B: At. Mol. and Opt. Phys.*, 53:182001, 2020.
- [44] F. Robicheaux, T. Graham, and M. Saffman. Photon recoil and laser focusing limits to Rydberg gate fidelity. *Phys. Rev. A*, 103:022424, 2021.
- [45] H. F. Hofmann. Complementary classical fidelities as an efficient criterion for the evaluation of experimentally realized quantum operations. *Phys. Rev. Lett.*, 94:160504, 2005.
- [46] D. M. Reich, G. Gualdi, and C. P. Koch. Minimum number of input states required for quantum gate characterization. *Phys. Rev. A*, 88:042309, 2013.
- [47] T. G. Walker and M. Saffman. Consequences of Zeeman degeneracy for the van der Waals blockade between Rydberg atoms. *Phys. Rev. A*, 77:032723, 2008.
- [48] M. Saffman and K. Mølmer. Efficient multiparticle entanglement via asymmetric Rydberg blockade. *Phys. Rev. Lett.*, 102:240502, 2009.
- [49] M. Müller, I. Lesanovsky, H. Weimer, H. P. Büchler, and P. Zoller. Mesoscopic Rydberg gate based on electromagnetically induced transparency. *Phys. Rev. Lett.*, 102:170502, 2009.
- [50] M. Khazali and K. Mølmer. Fast multiqubit gates by adiabatic evolution in interacting excited-state manifolds of Rydberg atoms and superconducting circuits. *Phys. Rev. X*, 10:021054, 2020.
- [51] J. T. Young, P. Bienias, R. Belyansky, A. M. Kaufman, and A. V. Gorshkov. Asymmetric blockade and multiqubit gates via dipole-dipole interactions. *Phys. Rev. Lett.*, 127:120501, 2021.

- [52] M. Saffman and T. G. Walker. Analysis of a quantum logic device based on dipole-dipole interactions of optically trapped Rydberg atoms. *Phys. Rev. A*, 72:022347, 2005.
- [53] Y. Wu, W.-S. Bao, S. Cao, F. Chen, M.-C. Chen, X. Chen, T.-H. Chung, H. Deng, Y. Du, D. Fan, M. Gong, C. Guo, C. Guo, S. Guo, L. Han, L. Hong, H.-L. Huang, Yong-Heng Huo, Liping Li, Na Li, Shaowei Li, Yuan Li, Futian Liang, Chun Lin, Jin Lin, Haoran Qian, Dan Qiao, Hao Rong, Hong Su, Lihua Sun, Liangyuan Wang, Shiyu Wang, Dachao Wu, Yu Xu, Kai Yan, Weifeng Yang, Yang Yang, Yangsen Ye, Jianghan Yin, Chong Ying, Jiale Yu, Chen Zha, Cha Zhang, Haibin Zhang, Kaili Zhang, Yiming Zhang, Han Zhao, Y. Zhao, L. Zhou, Q. Zhu, C.-Y. Lu, C.-Z. Peng, X. Zhu, and J.-W. Pan. Strong quantum computational advantage using a superconducting quantum processor. *arXiv:2106.14734*, 2021.
- [54] I. I. Beterov and M. Saffman. Rydberg blockade, Förster resonances, and quantum state measurements with different atomic species. *Phys. Rev. A*, 92:042710, 2015.
- [55] A. G. Fowler, M. Mariantoni, J. M. Martinis, and A. N. Cleland. Surface codes: Towards practical large-scale quantum computation. *Phys. Rev. A*, 86:032324, 2012.
- [56] D. K. Tuckett, S. D. Bartlett, and S. T. Flammia. Ultrahigh error threshold for surface codes with biased noise. *Phys. Rev. Lett.*, 120:050505, 2018.
- [57] J. M. Auger, S. Bergamini, and D. E. Browne. Blueprint for fault-tolerant quantum computation with Rydberg atoms. *Phys. Rev. A*, 96:052320, 2017.
- [58] H. E. Ercan, J. Ghosh, D. Crow, V. N. Premakumar, R. Joynt, M. Friesen, and S. N. Coppersmith. Measurement-free implementations of small-scale surface codes for quantum-dot qubits. *Phys. Rev. A*, 97:012318, 2018.
- [59] R. Versluis, S. Poletto, N. Khammassi, B. Tarasinski, N. Haider, D. J. Michalak, A. Bruno, K. Bertels, and L. DiCarlo. Scalable quantum circuit and control for a superconducting surface code. *Phys. Rev. Appl.*, 8:034021, 2017.

- [60] M. Saffman, I. I. Beterov, A. Dalal, E. J. Paez, and B. C. Sanders. Symmetric Rydberg controlled- Z gates with adiabatic pulses. *Phys. Rev. A*, 101:062309, 2020.
- [61] C. Horsman, A. G. Fowler, S. Devitt, and R. van Meter. Surface code quantum computing by lattice surgery. *New J. Phys.*, 14:123011, 2012.
- [62] C. J. Trout, M. Li, M. Gutiérrez, Y. Wu, S.-T. Wang, L. Duan, and K. R. Brown. Simulating the performance of a distance-3 surface code in a linear ion trap. *New Jour. Phys.*, 20:043038, 2018.
- [63] T. E. O'Brien, B. Tarasinski, and L. DiCarlo. Density-matrix simulation of small surface codes under current and projected experimental noise. *npj Qu. Inf.*, 3:39, 2017.
- [64] Otten Matthew. Quantum in c, <http://https://github.com/0tt3r/quac>.